TESIS DOCTORAL

Convertidor Electrónico embarcado con control bi-modal del almacenamiento de energía con implementación de estrategias V2G (Vehicle To Grid) y del motor del vehículo eléctrico sin sensor

Jaime Pando Acedo

Programa de Modelización y Experimentación en Ciencia y Tecnología

2021

TESIS DOCTORAL

Convertidor Electrónico embarcado con control bi-modal del almacenamiento de energía con implementación de estrategias V2G (Vehicle To Grid) y del motor del vehículo eléctrico sin sensor

Jaime Pando Acedo

Programa de Modelización y Experimentación en Ciencia y Tecnología

Con la conformidad de los directores:

Enrique Romero Cadaval **María Isabel Milanés Montero**

2021

PhD. Dissertation

Embedded Bi-Modal Controlled Electronic Converter For Energy Storage With Vehicle To Grid And Sensorless Strategies

Jaime Pando Acedo

Modelling and Experimentation in Science and Technology Doctoral Program

With the approval of the directors:

Enrique Romero Cadaval **María Isabel Milanés Montero**

2021

A las verdaderas investigadoras de mi familia

Agradecimientos

Sólo ha sido gracias a la ayuda de una serie de personas que he podido realizar este trabajo, que aunque culmina con este documento, ha sido realizado durante largos años. He puesto mi empeño en que el trabajo realizado estuviera a la altura del reto, y aunque siempre hay aspectos que podrían mejorar, lo que es seguro es que sin el apoyo de dichas personas no lo habría conseguido.

En primer lugar quiero mostrar mi más profundo agradecimiento a mis padres, fuente de apoyo absoluto e incondicional, que no dudaron ni por un instante de que sería capaz de hacer lo que me propusiera. Especial mención a mi madre, verdadera investigadora en mi familia, de la que siempre recordaré verla estudiar sin descanso, y sólo ahora comprendo la constancia necesaria para afrontar este trabajo.

Nadie conoce mejor el día a día experimentado que los compañeros de laboratorio, y en mi caso no ha sido una excepción. Tanto los primeros como los últimos, sólo he encontrado ánimos y compañerismo en ellos. Largos días de laboratorio que sólo gente que los comparte contigo son capaces de entender.

Rodearse de amigos es lo mejor que puede hacer uno con su vida, y para mi ha sido fundamental en este periodo. Sin menoscabo del aprecio que les profeso a todos ellos, quiero agradecer a David su consejo y comprensión, siendo alguien que conoce las dificultades de este camino. Y no puedo olvidarme de Claudia, quien ha sabido apoyarme en los últimos momentos, posiblemente los más duros. Su tesón y constancia siempre han causado en mí una gran admiración, es una verdadera investigadora aunque ella aún no lo sepa.

No puedo terminar sin agradecer a mis directores de tesis, Enrique y Maribel, por haber recorrido junto a mí este camino y orientado a lo largo de él. También quiero mencionar a la Junta de Extremadura por su financiación mediante el programa de Ayudas para la Financiación de Contratos Predoctorales (PD16044).

Por último, mi más profundo reconocimiento para miles de personas que de forma desinteresada desarrollan herramientas de código libre como LaTeX. Gracias a ellos se pueden desarrollar documentos como este.

Resumen

Debido a las preocupaciones medioambientales, la investigación relativa al Vehículo Eléctrico (VE) ha experimentado un notable avance en los últimos años. El presente trabajo versa sobre el desarrollo de un convertidor electrónico y su controlador para un Motor Síncrono de Imanes Permanentes (MSIP), como los empleados en los VE. Dicho controlador incluye funciones avanzadas destinadas a reducir el coste del sistema y aumentar su fiabilidad. El convertidor está compuesto por una parte destinada a la propulsión del vehículo y otra a la fase de carga de las baterías del VE.

Las funciones del controlador diseñado para el convertidor son tres. La primera consiste en el control del MSIP sin usar el sensor de posición del motor para ello. Eliminar este elemento crítico se traduciría en un aumento de la fiabilidad y simplificación del sistema. En segundo lugar, las estrategias de carga del VE se han considerado desde el punto de vista de su inclusión en las Comunidades Inteligentes, dotando al cargador del VE con funciones activas de red. Después, se ha discutido la integración de los sistemas de propulsión y carga del VE, para conseguir reducir los componentes del sistema completo y eliminando el par de carga producido. La última función del controlador trata sobre la detección y corrección de vibración en la estructura del VE, utilizando para ello el control de velocidad del MSIP.

Los resultados de simulación y experimentales validan las estrategias del controlador para el convertidor considerado.

Abstract

Due to environmental concerns, the research relative to the Electric Vehicle (EV) has been increasing steadily during the last years. The work presented describes the electronic converter and its controller for a Permanent Magnet Synchronous Motor (PMSM), like the ones used in EVs. Said controller contains advanced functions that allow for a cost reduction in the system and an increase in its reliability. The converter is formed by two parts: one used for driving the PMSM and the other one for charging the storage system of the EV.

The functions of the controller designed for the converter are three. The first one consists on controlling the PMSM without the need of a position sensor. The elimination of this critical component would translate in a simpler system enhancing the reliability. The second function of the controller is to use the EV as a component of the Smart Communities, providing the EV charger with grid active functions. The integration of the charger and the driving system is then discussed for a reduction in the number of components needed, removing the charging torque produced. Finally, the last function is designed to detect and correct vibrations detected in the EV structure, using the PMSM's speed controller.

Simulation and experimental results prove the good operation of the control strategies for the converter proposed.

Contents

List of Figures

List of Tables

Glossary

$\boldsymbol{i_c^{-\omega_c t+\theta_{sl\_e}}}$ High-frequency current vector in a reference frame rotating at $-\omega_c t + \theta_{sl\_e}$, page 34

$\boldsymbol{i_c^{\omega_c t+\theta_{sl\_e}}}$ High-frequency current vector in a reference frame rotating at $\omega_c t + \theta_{sl\_e}$, page 30

$\boldsymbol{i_c^R}$ High-frequency current vector in the real rotor reference frame, page 28

$\boldsymbol{i_c^S}$ High-frequency current vector in the stator reference frame, page 29

$\boldsymbol{u_c^{\hat{R}}}$ High-frequency voltage vector in the estimated rotor reference frame, page 26

$\boldsymbol{u_c^R}$ High-frequency voltage vector in the real rotor reference frame, page 27

$\boldsymbol{u_c^S}$ High-frequency voltage vector in the stator reference frame, page 27

δ_A Perturbation introduced in the correction current's amplitude, page 149

δ_{ph} Perturbation introduced in the correction current's phase, page 149

Γ Vibration amplitude, page 133

λ_m Rotor magnet flux, page 12

μ Charger efficiency, page 113

ω Rotor mechanical speed in radians per second, page 9

ω_c High frequency pulsation, page 26

ω_{ref} Reference speed in radians per second, page 52

ω_{sl} Estimated rotor mechanical speed in radians per second, page 9

ϕ_c Phase of the vibration correction current, page 145

ϕ_{hL} Angle phase of the harmonic of order h of the load current source, page 67

ϕ_{hs} Angle phase of the harmonic of order h of the grid voltage source, page 67

θ Rotor mechanical angle in radians, page 9

θ_e Rotor electrical angle in radians, page 12

θ_{sl_e} Estimated rotor electrical angle in radians, page 27

θ_{sl} Estimated rotor mechanical position in radians, page 9

$BEMF$	Back-Electromotive Force, page 5
BPF	Band Pass Filter, page 31
d_{AC}	Duty cycle for the AC side of the converter, page 77
d_{DC_bat}	DC converter side duty cycle for the battery, page 80
d_{DC_scap}	DC converter side duty cycle for the supercapacitor, page 80
dPF	displacement Power Factor, page 91
$ESMS$	Energy Storage Management System, page 61
ESS	Energy Storage System, page 59
EV	Electric Vehicle, page 1
f_c	Cut-off frequency, page 32
f_g	Power grid frequency, page 104
F_r	Machine's friction coefficient, page 13
$f_{\Gamma c}$	Frequency of the vibration correction current, page 145
f_ω	Electric rotation frequency, page 136
FFT	Fast Fourier Transform, page 149
FOC	Field Oriented Control, page 4
h	Harmonic order, page 67
HPF	High Pass Filter, page 32
i_{ab}	a and b phase currents in stationary frame, page 9
i_{bat}	Battery current, page 65
i_{ch-D_ref}	Charger current reference from DSC control, page 72
i_{ch-H_ref}	Charger current reference from THC control, page 72
i_{ch-Q_ref}	Charger current reference from QSC control, page 72
i_{ch}	Charger current, page 65
I_c	Amplitude of the vibration correction current, page 145
I_{hL}	RMS value of the load harmonic components, page 96
i_L	Load current, page 65
I_{nm}	Motor nominal current, page 109
$i_{q\_ref\_D}$	Derivative part of the reference for the q-axis current controller, page 140
$i_{q\_ref\_I}$	Integral part of the reference for the q-axis current controller, page 140
$i_{q\_ref\_PI}$	Speed PI controller share of the q-axis current reference, page 145
$i_{q\_ref\_P}$	Proportional part of the reference for the q-axis current controller, page 140
$i_{q\_ref\_vib}$	Vibration controller share of the q-axis current reference, page 145

i_{q_ref} Reference for the q-axis current controller, page 140

i_{scap} Supercapacitor current, page 65

IOC Integrated Onboard Charger, page 62

J Machine's moment of inertia, page 13

k_1, k_2 Linear regression coefficients, page 52

L_d Direct-axis inductance, page 12

L_q Quadrature-axis inductance, page 12

L_{AC} AC filter inductance, page 79

L_{dq}, L_{qd} Mutual inductance terms in rotor reference frame, page 28

LPF Low Pass Filter, page 31

n Rotor speed in rpm, page 136

NVH Noise, Vibration and Harshness, page 129

p Pole pairs, page 12

$P\&O$ Perturbation and Observation, page 148

P_J Joule losses in the machine windings, page 113

P_u Useful power developed by the charger, page 113

P_{inv} Inverter losses, page 113

PF Power Factor, page 91

PI Proportional-Integral controller, page 20

PID Proportional Integral Derivative controller, page 139

PLL Phase-Locked Loop, page 69

$PMSM$ Permanent Magnet Synchronous Machine, page 3

PWM Pulse Width Modulation, page 17

R_D Reverse diode resistance, page 16

R_s Rotor resistance per phase, page 12

R_{EB} Electronic breaker resistance, page 16

s Laplace operator, page 12

s_{abc} switching signals for the electronic switches of three branches abc, page 9

$SCEMS$ Smart Community Energy Management System, page 61

$SMPMSM$ Surface Mounted PMSM, page 8

T_c Switching time, page 23

T_e Electromagnetic torque, page 12

T_L Load torque, page 13

T_s Fundamental sampling time in seconds, page 26

T_{sc} Sampling time for the control algorithms in seconds, page 26

THD	Total Harmonic Distortion, page 82
U_c	Injected voltage peak value, page 26
v_0	Unitary signal in phase with grid the voltage, page 69
V_D	Reverse diode voltage drop, page 16
V_{1s}	RMS value of the grid voltage's fundamental component, page 70
v_{90}	Unitary signal in quadrature with the grid voltage, page 69
v_{abc}	*abc* voltages in the stationary frame, page 9
v_{ao}	Middle point to phase A voltage, page 16
v_{bat}	Battery voltage, page 65
V_{DC}	DC bus voltage, page 9
v_{dq}	*dq* voltages in the rotor reference frame, page 10
V_{EB}	Electronic breaker voltage drop, page 16
v_{L_AC}	Voltage drop in the AC filter inductor, page 79
v_{L_bat}	Voltage drop in the battery filter inductor, page 80
v_{R_AC}	Voltage drop in the AC filter resistor, page 79
v_{R_bat}	Voltage drop in the battery filter resistor, page 80
v_{scap}	Supercapacitor voltage, page 65
v_{sw}	Switch voltage drop, page 16
v_s	Grid voltage, page 65
w_f	Band-pass filter window, page 32

1

Introduction

Climate change is a fact. The Intergovernmental Panel on Climate Change (IPCC) estimates that the human activities are responsible of 1.0º C of global warming above pre-industrial levels. Moreover, is likely to reach 1.5º C between 2030 and 2052 if it increases at the current rate [1]. The effects of climate change are diverse and threatens the lifestyle of all species, not only humankind. Some of them are already noticeable nowadays, such as an increase in: the mean temperature on most land and ocean regions, hot extremes in most inhabited regions, heavy precipitation in some regions and the probability of drought in others. Other changes are still to come, but include the rise of the sea level and heavy impact on biodiversity and ecosystems, including species loss and extinction. However, the adverse effects of climate change can be less likely to happen if the global warming is limited to 1.5º C. This is the challenge of our and future generations, and inspires intergovernmental organizations, such as the European Union (EU), to take action. This are the reasons behind the European Green Deal [2].

Among the several key points of the European Green Deal depicted in Figure 1.1, this work directly relates to the building of a more sustainable and

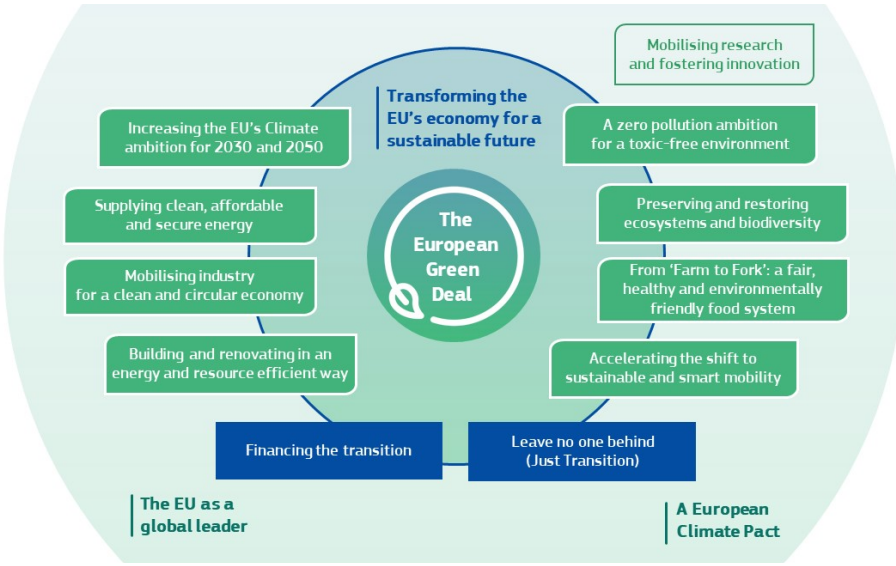

Figure 1.1: The European Green Deal [2]

smarter mobility, as well as to the forming of a zero pollution and toxic-free environment. Transport accounts for a quarter of the greenhouse emissions of the EU, and is still increasing. In order to fulfill the goals established, there is a need of a 90% reduction in transport emissions by 2050. From all the transport emissions in the EU, the road transport accounts for a 71.7%. Therefore, for achieving such reduction in the emissions, the final leap to the Electric Vehicle (EV) has to be done. The EU estimates that by 2025, we will increase the number of public recharging points and alternatively fueled cars from 140k and 975k to 1 million and 13 million, respectively. To support such an increase, the deployment of the public recharging points has to fill the gaps existing, notably for long-distance travel and less densely populated areas.

Each member of the EU has to adapt the road plan specified by the European Commission to local legislation. For the case of Spain, the law approved in May

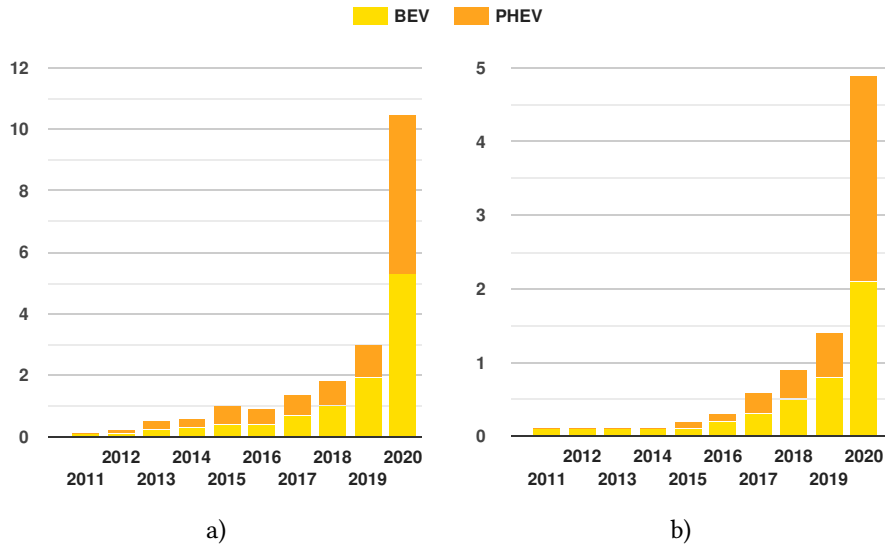

Figure 1.2: Newly registered AF cars relative to total newly registered cars (in %). a) European Union. b) Spain. Data from the European Alternative Fuels Observatory.

2021 sets the legal requirements to fulfill the goals marked by Europe [3]. Related to the smarter mobility and electrification of the vehicle fleet, the objectives are that by 2040, all new registered vehicles for non commercial uses shall be emission-free. Figure 1.2 represent the percentage of the newly registered Battery Electric Vehicles (BEV) and Plug-in Hybrid Vehicles in (PHEV) in the last years. It is clear that although 2020 has been a great year for the EV in Spain, much remains to be done. Although the technology used in EVs is maturing slowly, it is still a high interest topic in research. Advanced control techniques are developed to enhance the benefits of this vehicles and to make them more appealing to a hesitant population.

Regarding the deployment of public recharging points, at least one 50 kW

charger will be installed in most gas stations. This is a starting point, but clearly not enough to supply the EVs that are to come. Moreover, cities with a population higher than 50k must have low emission zones before 2023. Thus, residential low power charging is necessary. This can be exploited to use it as an active element able to provide grid functions and transform regular homes into Smart Homes. These Smart Homes, together with distributed renewable energy generation, are the key elements of the Smart Communities.

Another aspect of the decarbonisation needed in global economy is the maximization of the renewable energy production and energy efficiency. It is expected that the contribution of renewable energy to the energy consumption in Spain will rise from the 16% (2015) to the 42% (2030) [4]. To that end, the focus is set on the Smart Communities and their regulation, allowing them to consume, produce and sell renewable energy. This kind of low-level organizations bring several benefits to the individuals forming part of them, and to society as a whole, as it has been stated.

This work contributes to the research fields related to these aspects so important and close to us. Chapter 2 will develop an advance sensorless control of the motor of an EV, providing with simulations and experimental results to test its usefulness. This kind of control techniques are desirable since brings the opportunity of reduce costs and increase reliability of the system.

The charging of the EVs is a key point of its adaptation by society, and in Chapter 3, an onboard charger topology is developed and tested. Such charger is able to control the energy flow and the current quality demanded by a smart home. It uses the storage normally available to the EVs and explores the advantages of hybridization with other storage system, a supercapacitor. The integration of such charger with the drive system of the EV is then analyzed, studying a solving the difficulties that arise, providing experimental results.

Chapter 4 is devoted to the analysis and correction of the vibrations developed in the motor, when is attached to any structure. Experiments are used to measure the vibrations and then a correction algorithm is developed an tested in simulation. Chapter 5 summarizes the conclusions of the work developed.

2

Sensorless control of the PMSM

2.1 Introduction

The Permanent Magnet Synchronous Machine (PMSM) is widely regarded as one of the most used rotative electrical machine, along with the Induction Motor. It has found its place mainly in the EV. The main reasons for that are the high efficiency, high torque to size ratio and remarkable robustness and reliability. For decades, the synchronous machines were not present in the variable speed applications due to the lack of velocity regulation options. That changed with the rise of the power electronics and they have become a very interesting option in the traction applications.

In order to control the motor, there are several options regarding control strategies. Among them, the vector control of the PMSM is the more relevant one found in the literature and industry, and it is still target of research and development [5–8]. This control technique is based in the DC motors control, aiming to separate the flux and torque variables so they are independently con-

trolled. Since the vector control consists on transferring the currents variables to the rotor magnetic field reference system, this control strategy is often referred as Field Oriented Control (FOC).

As the FOC is based in expressing variables in the direction marked by the rotor field, the acquisition of the accurate rotor angle is key to a good performance of the system. The solution of this problem is often extra pieces of equipment as resolvers or encoders. They are referred as rotatory electrical transducers, the former being analog devices while the latter are digital ones. This devices translate the rotor angle to a signal that can be measured by a control platform and used in the FOC. Nevertheless, the use of such gear represents extra complexity of the system, increases the manufacturing cost and reduces the system reliability [9, 10]. Moreover, the use of encoders can be a source of estimating errors and could deteriorate the system perfomance [11].

In order to tackle the issues described, and since the machine itself resembles the configuration of a resolver, sensorless techniques have been studied and reserched for many years now [12–15]. They aim to estimate the angular position of the rotor without the need of any external equipment, by making use of the machine and the equations that describe its behaviour. Getting rid of the extra hardware would mean a great benefit for many industrial and commercial applications.

2.1.1 Sensorless techniques classification

Depending on the speed range, sensorless strategies can be classified into different groups, as it can be observed in Figure 2.1. If the speed is high enough, the estimation is usually made based on machine models estimators. The open-loop estimators are purley based on integrating the Back-Electromotive Force (BEMF) measurement without correction, while the closed-loop models try to improve their robustness by including other quantities [15–21]. Since the BEMF

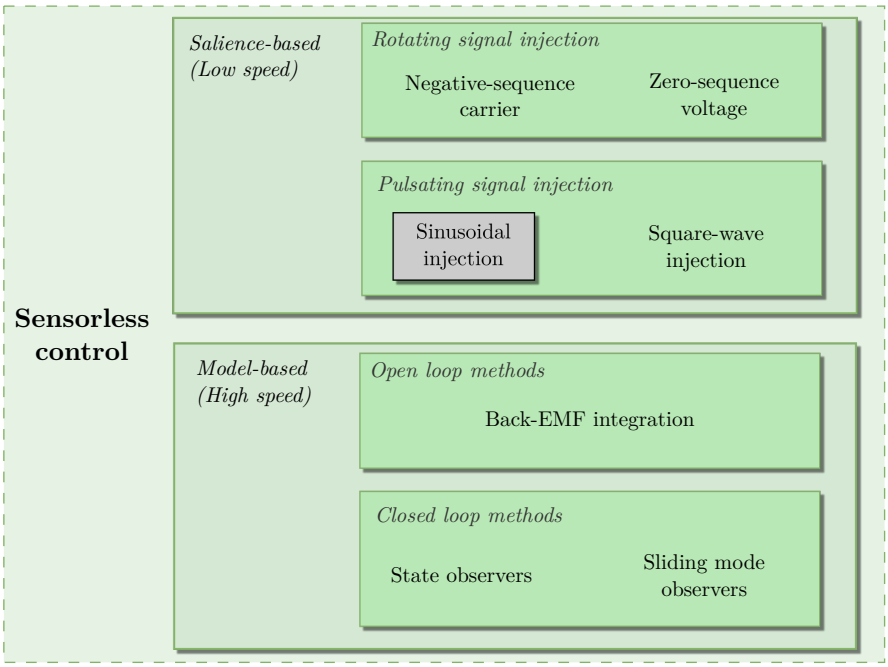

Figure 2.1: Sensorless categories classification. The estimation technique investigated in this work is marked with a grey rectangle.

is proportional to the rotor speed, the main limitation is acquiring a good signal when the speed is low or close to zero.

Focusing on the low speed operation, the main group is the high frequency injection. This kind of techniques exploits the resemblance of the machine with the resolver transducer. They inject a high frequency signal along with the fundamental excitation into the machine [22–27]. This signal is modulated with the rotor position, and the carrier signal porting the rotor information can be later on processed and extracted from the measured current. They exploit the anisotropy of the machine, i.e., the fact that the reluctance of the airgap in the machine varies along the angle considered depending on the rotor position. It is said that the machine presents a salience based on this reluctance variance.

Although they have proven good results, the introduction of the high frequency signal means extra losses, noise and vibrations. Moreover, the signal recovery for the estimation of the rotor position can prove to be difficult and requires a high signal to noise ratio.

Diving deeper into the high frequency injection techniques, the clasiffication branches into several groups, according to the signal injection properties. Since the FOC works using the rotor Synchronous Reference Frame (SRF), the signal injection can be done in this reference frame as well [28, 29]. The injection is then made along the d-axis, in order to avoid injecting torque producing currents [30]. Since only one component is injected, this technique is often referred as pulsating vector injection. It has the advantage of having a simple signal processing and good estimation results [30]. However, there have been reports of steady state errors and convergence issues while starting the motor [30–32]. Other possibility is to use a rotating signal injection, made in the stationary reference frame [32–35]. They share similarities in the signal processing process but in the comparations made between both [36], the pulsating vector injection was found to be more precise. Nevertheless, the rotating vector provided more robust estimations, specially during transients.

To overcome the problems that raise from the use of signal injection, several modifications have been proposed. Some authors propose to use the zero-sequence voltage as the carrier for the rotor position estimation [23, 37–39]. Compared to the previous techniques, the zero-sequence carrier estimation can raise the injection frequency to higher values. This means a reduction of torque ripples and noise. Nevertheless, the measurements of the zero-sequence carrier is troublesome, needing access to the neutral point of the machine and voltage sensors, which are not present in the system otherwise.

Other proposal is to modify the waveform of the injected signal. Instead of injecting a sinusoidal wave into the machine, there has been a trend to use

Reference	Voltage Injection	% of Rated Voltage
[42]	100 V	78.74
[30]	40 V	66.6
[43]	45 V	56.25
[41]	30 V	40.65
[31]	40 V	33.33
[44]	45 V	28.48
[30]	40 V	17.39
[45]	40 V	17.39
[23]	4 V	11.11
[46]	25 V	10.87
[47]	20 V	9.09
[48]	5.8 V	7.25
[49]	14 V	6.08
[50]	20 V	5.26
[32]	7.75 V	3.52

Table 2.1: Different injection levels found in the literature

a pulsating square-wave injection [23, 40]. This kind of injection also shares with the zero-sequence injection the advantage of being able to significantly raise the injection frequency, but is simpler to acquire the signals needed since they make use of the equipment already present in the system. However, most of these estimation techniques need to compute derivatives of the currents measured, making them specially sensitive to noise and inverter non-linearities [41].

2.1.2 Challenges encountered

No matter what is the sensorless thechnique used, the injected voltage's magnitude represents one of the biggest concerns found in the literature. In general, rising the injection frequency is desirable but by doing so, the carrier signal porting the rotor information will decrease for the same voltage. So the injected

voltage will have to raise as well in order to maintain a good signal to noise ratio.

Most of the research consulted need a signal in the range of 30-50 V [30–32, 41, 43–45] and only a few in the 10-30 V range [23, 46, 47, 49, 50]. Moreover, looking at Table 2.1 one can see that if the injected voltage is compared to the rated voltage of the machine under test, the ratios are still high. This fact is specially true for the case of Surface Mounted PMSM (SMPMSM), because the low saliency ratio they present. This ratio represents how easily the rotor can be located in terms of the airgap reluctance. Therefore, SMPMSM will require a higher injection to be able to track the rotor. This fact motivates the need of further developing the signal processing of the sensorless methods in order to be able of extracting as much information as possible from a low amplitude signal [42, 47].

2.1.3 Goal of the research

This work aims to enhance the performance of the sensorless technique applied to a SMPMSM. It explores the high frequency sinusoidal injection done in the SRF, marked in Figure2.1. The goal is to modify the existing signal processing found in the literature trying to achieve a good performance with the lowest injection possible.

Throughout the chapter, the system used for testing the sensorless control of the machine will be detailed and a simulation model will be developed. Afterwards, the sensorless technique under study will be explained and the expressions that describe it will be developed. Then, the proposed enhanced demodulation will be presented, providing simulations and experimental results to test it.

2.2 Mathematical modelling and simulation

The modelling and simulation of the system is carried out using the Simulink tool from MATLAB. Starting with the differential equations that dictate the behaviour of the physiscal system, its different parts are modelled as blocks that can then be connected and easily manipulated.

In this section, the model for the different parts of the system will be developed. The system model can break down into the following parts:

- Meassures and sampling. This part will take care of the sampling down of the measured variables from other parts of the system
- Sensorless algorithm. This model will take the currents and will make estimations for both speed and rotor position.
- Control. This part of the system will use the measured variables and determine the inputs needed by the power electronics so that the system behaves as commanded.
- Power electronics. This part is in charge of generating the voltage signals needed by the machine, as commanded by the control part.
- Machine model. This is the model that simulates the behaviour of the electrical machine.

The overall system model is depicted in Figure 2.2, where the measured variables are marked with the subscript 'm'. The inputs of the system are the DC bus voltage V_{DC}, two of the three phase currents i_{ab}, and the rotor position θ. The sensorless model will provide with estimations for both speed and rotor position, labeled as ω_{sl} and θ_{sl} respectively. The outputs of the control model will be the the switching signals for the power electronics, s_{abc}, that will serve as the inputs

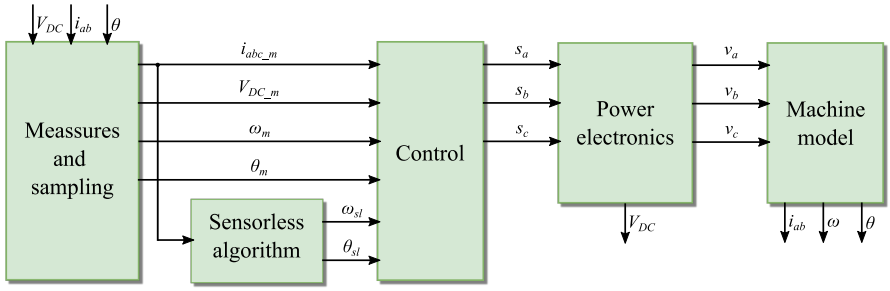

Figure 2.2: General scheme of the system modelling used for simulation

for the power electronics model. Lastly, the phase voltages v_{abc} generated by the power electronics are the inputs for the machine model.

The division of the system model into the parts described is chosen in order to make the transitions from the simulation to the experimental part as smooth as possible. Thus, the sensorless algorithms and the control scheme during the simulation phase can be used in the experimental platform as they will have the same inputs and outputs.

2.2.1 Machine modelling

Simulation of the PMSM is made in the synchronous frame, and its general scheme is shown in Fig. 2.3. This means that the three-phase voltages provided by the power electronics will be transferred to a reference system synced with the rotor, referred as the dq reference system. This transformation is made using the $dq0$ transform, so the dq voltages are obtained as follows

$$[v_{0dq}] = [T][v_{abc}], \tag{2.1}$$

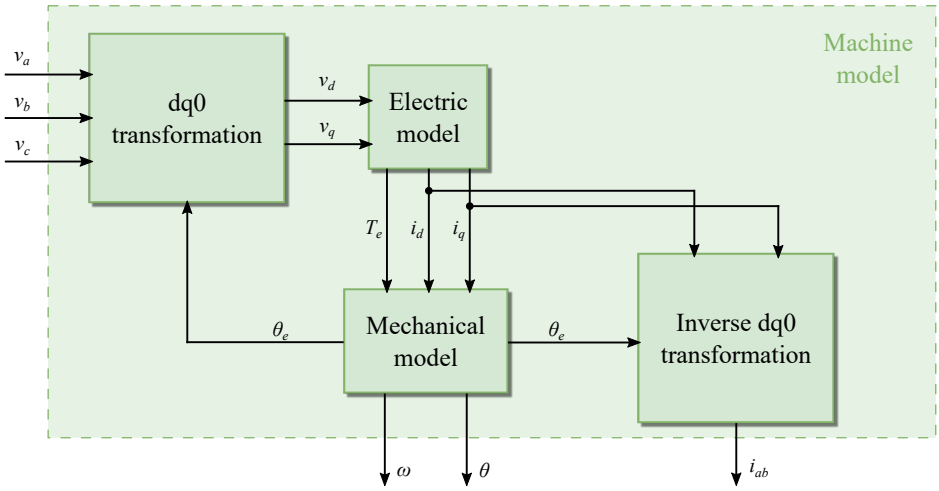

Figure 2.3: Simulation model for the PMSM using the *dq* reference frame

where T is the *dq*0 or Park transform matrix. This matrix is the combination of two transformations. The first will transform the voltages from the *abc* reference frame where into the $\alpha\beta\gamma$ reference frame, known as the Clarke transform

$$\begin{bmatrix} v_\gamma \\ v_\alpha \\ v_\beta \end{bmatrix} = [C] \begin{bmatrix} v_a \\ v_b \\ v_c \end{bmatrix} = \sqrt{\frac{2}{3}} \begin{bmatrix} \frac{1}{\sqrt{2}} & \frac{1}{\sqrt{2}} & \frac{1}{\sqrt{2}} \\ 1 & -\frac{1}{2} & -\frac{1}{2} \\ 0 & \frac{\sqrt{3}}{2} & -\frac{\sqrt{3}}{2} \end{bmatrix} \begin{bmatrix} v_a \\ v_b \\ v_c \end{bmatrix}, \tag{2.2}$$

where C is the Clarke transform. In this reference frame, the coordinates are orthogonal to each other, and the v_γ component is only non zero in non-balanced systems, balanced system with harmonics whose order is multiple of three or systems with DC component. Therefore, it is normally neglected and so it will be done for the rest of the analysis. By multiplying by the Park transform, this orthogonal system will rotate synced with the rotor. Thus, one can have

$$\begin{bmatrix} v_d \\ v_q \end{bmatrix} = [P] \begin{bmatrix} v_\alpha \\ v_\beta \end{bmatrix} = \begin{bmatrix} \cos\theta_e & \sin\theta_e \\ -\sin\theta_e & \cos\theta_e \end{bmatrix} \begin{bmatrix} v_\alpha \\ v_\beta \end{bmatrix}, \tag{2.3}$$

where S is an rotation matrix and θ_e is the rotor angle, in electrical radians. It follows that, the following holds for a machine with a certain amount p of pole

pairs

$$\theta_e = p\theta. \tag{2.4}$$

Once the voltages has been transferred to the rotor synchronous frame, the motor currents are derived. The dq voltages can be expressed as a function of the machine parameters, and the equations modelling the circuit are

$$\begin{bmatrix} v_d \\ v_q \end{bmatrix} = \begin{bmatrix} R_s + L_d \frac{d}{dt} & -\omega L_q \\ \omega L_d & R_s + L_q \frac{d}{dt} \end{bmatrix} \begin{bmatrix} i_d \\ i_q \end{bmatrix} \begin{bmatrix} \omega \lambda_m \\ 0 \end{bmatrix}, \tag{2.5}$$

where L_{dq} are the direct and quadrature inductance, R_s is the rotor resistance and λ_m is the rotor magnet flux . In order to solve this differential equations for the currents, Laplace transform is applied and so the currents can be expressed as

$$\begin{aligned} I_d(s) &= \frac{V_d(s) + \Omega_e(s) L_q I_q(s)}{R_s + L_d s} \\ I_q(s) &= \frac{V_q(s) - \Omega_e(s) L_d I_d(s) - \Omega_e(s) \lambda_m}{R_s + L_q s}, \end{aligned} \tag{2.6}$$

where the uppercase variables represent the Laplace domain version of their temporal counterparts shown in (2.5), and s is the Laplace operator. Simulink takes care of the conversion from and to both domains, so the outputs of the electric model are temporal variables.

The interacion of the current and the fluxes of the machine is the cause of the appearance of the electromagnetic torque T_e, which can be expressed as a function of currents and inductances given a linear relationship between flux and current

$$T_e = p(L_d - L_q) i_d i_q + \lambda_m i_q. \tag{2.7}$$

It is interesting to see how the torque has two components. One is due to the product of the i_d and i_q currents and the difference in reluctance between the d-axis and q-axis, therefore it is called reluctance torque. The second one is due

to the magnets flux, and is only proportional to the current in the q-axis. This allows to control the torque produced by the machine by setting the i_q current to a certain value. This specially the case for SMPMSM, since they present a negligible reluctance torque due to the low salience factor.

Now that we have the main electrical variables of the simulation model, the mechanical variables will be computed next. The machine follows the second Newton's law and so the following holds

$$\begin{aligned} \sum T &= J\frac{d\omega}{dt} + F_r\omega \\ T_e(s) - T_L &= J\Omega(s)s + F_r\Omega(s) \\ \Omega(s) &= \frac{T_e - T_L}{Js + F_r}, \end{aligned} \tag{2.8}$$

where J is the moment of inertia, T_L is the load torque and F_r is the friction coefficient. The Laplace transform is used again to solve the system, and although the load torque could also time dependant, here is left as a constant for simplicity reasons. Last, the mechanical position of the rotor can be obtained by integrating the mechanical speed calculated in (2.8) by simply integrating as

$$\Theta(s) = \Omega(s)\frac{1}{s}. \tag{2.9}$$

Finally, the output currents of the machine model are in the *abc* reference system, and they are obtained from i_{dq} using the inverse Park and Clarke transforms

$$\begin{bmatrix} i_\alpha \\ i_\beta \end{bmatrix} = [P]^{-1} \begin{bmatrix} i_d \\ i_q \end{bmatrix} = \begin{bmatrix} \cos\theta_e & -\sin\theta_e \\ \sin\theta_e & \cos\theta_e \end{bmatrix} \begin{bmatrix} i_d \\ i_q \end{bmatrix} \tag{2.10}$$

$$\begin{bmatrix} i_a \\ i_b \\ i_c \end{bmatrix} = [C]^{-1} \begin{bmatrix} 0 \\ i_\alpha \\ i_\beta \end{bmatrix} = \sqrt{\frac{2}{3}} \begin{bmatrix} \frac{1}{\sqrt{2}} & 1 & 0 \\ \frac{1}{\sqrt{2}} & -\frac{1}{2} & \frac{\sqrt{3}}{2} \\ \frac{1}{\sqrt{2}} & -\frac{1}{2} & -\frac{\sqrt{3}}{2} \end{bmatrix} \begin{bmatrix} 0 \\ i_\alpha \\ i_\beta \end{bmatrix} \tag{2.11}$$

An example of the waveforms obtained using the PMSM simulation model described can be observed in Figure 2.4. Three-phase voltages are applied to

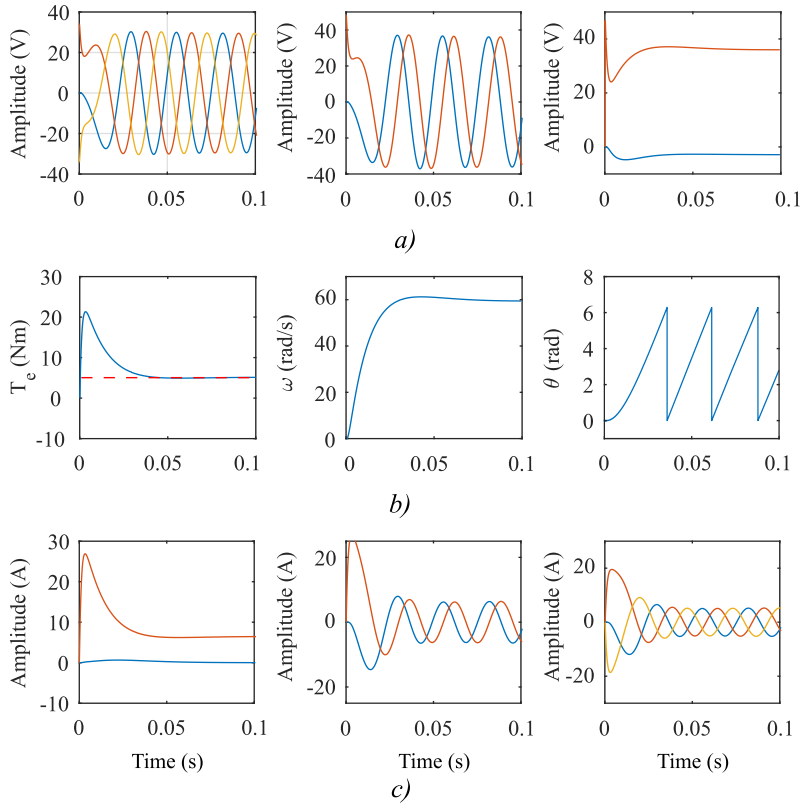

Figure 2.4: Waveforms of PMSM simulation model. a) From left to right transformation of the voltages from the *abc*, to $\alpha\beta$, to *dq*. b) From left to right: electromagnetic and constant load torque, rotor speed and rotor angle. c) From left to right: transformation of the machine currents from *dq*, to $\alpha\beta$, to *abc* reference frames

the model, and they are transferred to the *dq* reference frame, a process that is depicted in Figure 2.4a) and follows (2.2) and (2.3). Therefore, currents flow through the machine windings which gives raise to an electromagnetic torque according to machine parameters and following (2.7). This torque, together with the load applied to the machine, will accelerate the motor according to (2.8) and the rotor start to turn. This is showed in Figure 2.4b). Lastly, the *dq* currents are

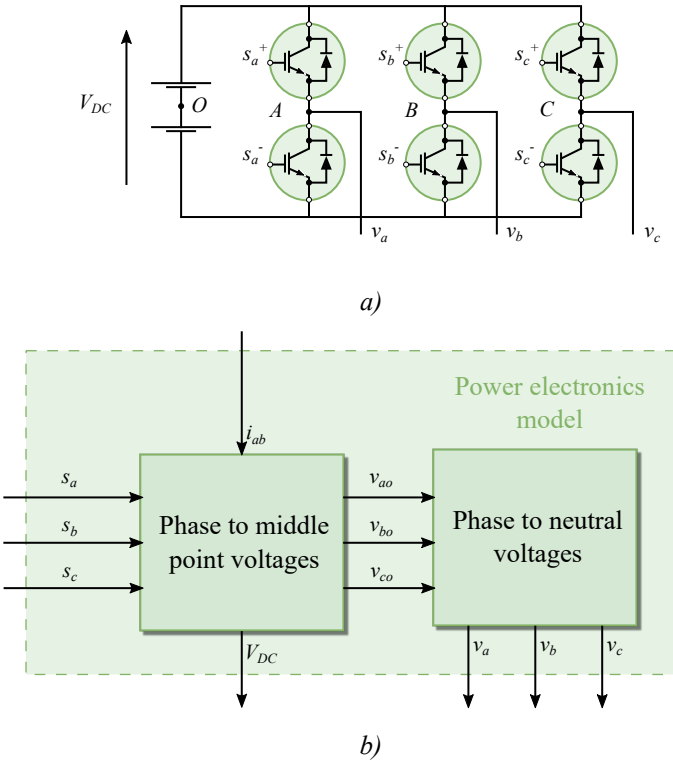

Figure 2.5: Power electronics included in the simulation. a) Circuit of the power topology employed. b) Simulation model of the topology

transferred back to the *abc* reference frame, as can be observed in Figure 2.4c).

2.2.2 Power electronics modelling

The power electronics used in this simulation is depicted in Fig. 2.5. The transformation from CC to to CA is made by means of a two-level three-branch inverter, using IGBT, which is shown in Fig. 2.5 a). With this configuration, three voltages with variable amplitude and frequency can be formed to drive the motor in the whole range of operation. Both switches in a branch are never turned on at the same time, so there is no shortcircuit of the DC bus. Therefore, having only

two states for a switch, high and low, taking branch A for instance, the following condition is met

$$s_a^+(t) = \overline{s_a^-(t)}, \forall t, \tag{2.12}$$

where the bar over $s_a^-(t)$ indicates the negation of its state,i.e., low if it is high and vice versa.

Following the simulation scheme depicted in Fig. 2.5 b), the next step is to compute the phase to middle point voltages. So, by continuing using branch A as reference

$$\begin{cases} s_a^+ = 1, s_a^- = 0 \rightarrow v_{ao} = \dfrac{V_{DC}}{2} - v_{sw} \\ s_a^+ = 0, s_a^- = 1 \rightarrow v_{ao} = -\dfrac{V_{DC}}{2} - v_{sw}, \end{cases} \tag{2.13}$$

where v_{ao} is the phase to middle point voltage and v_{sw} is the voltage drop in the switch. The voltage drop in the switch is computed taking into account the branch current and the switch state, according to the following relationship

$$\begin{aligned} s_a^+ = 1 &\begin{cases} i_a > 0 \rightarrow v_{sw} = V_{EB} + |i_a| R_{EB} \\ i_a \leq 0 \rightarrow v_{sw} = V_D + |i_a| R_D \end{cases} \\ s_a^+ = 0 &\begin{cases} i_a > 0 \rightarrow v_{sw} = -\left(V_D + |i_a| R_D\right) \\ i_a \leq 0 \rightarrow v_{sw} = -\left(V_{EB} + |i_a| R_{EB}\right) \end{cases} \end{aligned} \tag{2.14}$$

where V_{EB} and V_D are the voltage drops through the electronic breaker and reverse diode, and R_{EB} and R_D are the resistance of the electronic breaker and diode, accordingly. Having the phase to middle point voltages calculated, one can proceed to obtain the neutral to middle point and phase to neutral voltages as

$$v_{no} = \frac{1}{3}\left(v_{ao} + v_{bo} + v_{co}\right) \tag{2.15}$$

$$v_{an} = v_{ao} - v_{no}. \tag{2.16}$$

The power electronics model provides waveforms as the ones depicted in Figure 2.6. Depending on the switching state of each branch (Figure 2.6 a)), there

Parameter	Description	Value
V_{EB}	Electronic breaker voltage drop	3.7 V
V_D	Diode voltage drop	1.8 V
R_{EB}	Electronic breaker resistance	76×10^{-3} Ω
R_D	Diode resistance	32×10^{-3} Ω

Table 2.2: Inverter parameters used for simulation

will be a voltage drop in each element defined by (2.14). Following (2.13), the phase to middle point voltages are calculated (Figure 2.6d)) and used for the computation of the neutral to middle point voltage shown in Figure 2.6 c). Finally, the phase voltages are formed using (2.16) and are depicted in Figure 2.6 e). The inverter parameters used for the calculation of the voltages are gathered in Table 2.2.

2.2.3 Control modelling

The control model drives the motor in order to follow the references set by the user. The control model is split into two different parts, as shown in Fig 2.7: the first will compute the voltage references needed for the machine, the second one will generate the switching signals needed for the power electornics model. The control strategy used for generating the voltage references is the FOC, while Pulse Width Modulation (PWM) will be used for gerating switching signals.

2.2.3.1 Field Oriented Control

Using the same principle as the one explained in Section 2.2.1, sinusoidal variables are transferred to the rotor syncrhonous frame and become constant in the steady state. The simulation submodel for the FOC is shown in Fig. 2.8. The speed and angle used for this model can be selected from the estimation provided by the sensorless algorithm or the measured from the machine.

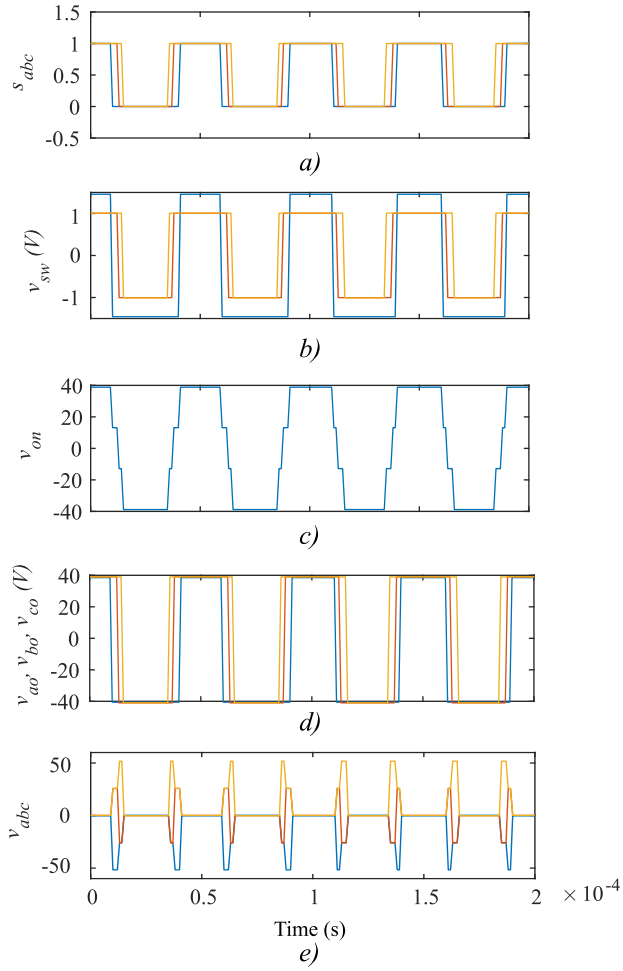

Figure 2.6: Inverter simulation model waveforms. a) Switching signals for the three branches. b) Voltage drop in each branch according to (2.14). c) Neutral to middle point voltages following (2.15). d) Phase to middle point voltage for each phase according to (2.13). e) Phase voltages of the three branches as in (2.16)

Conceptually, from the control theory point of view, the FOC uses two different control loops in cascade. The speed controller is the outer loop, and its output will serve as input for the inner loop, the current controller. The speed

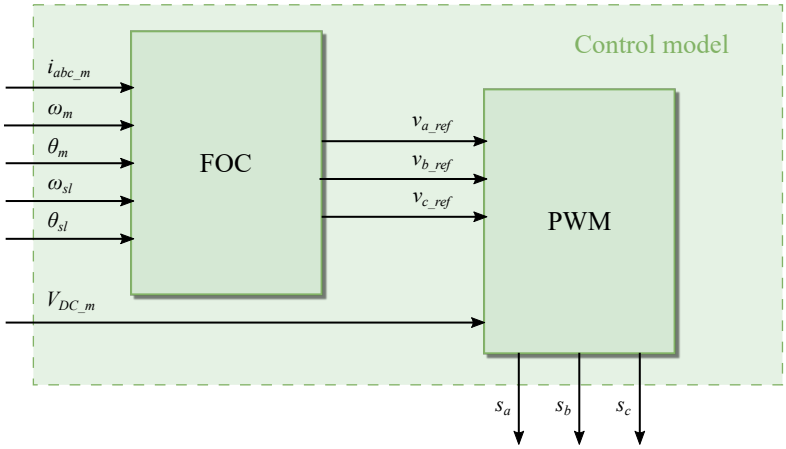

Figure 2.7: Control model including the two control submodels: FOC and PWM

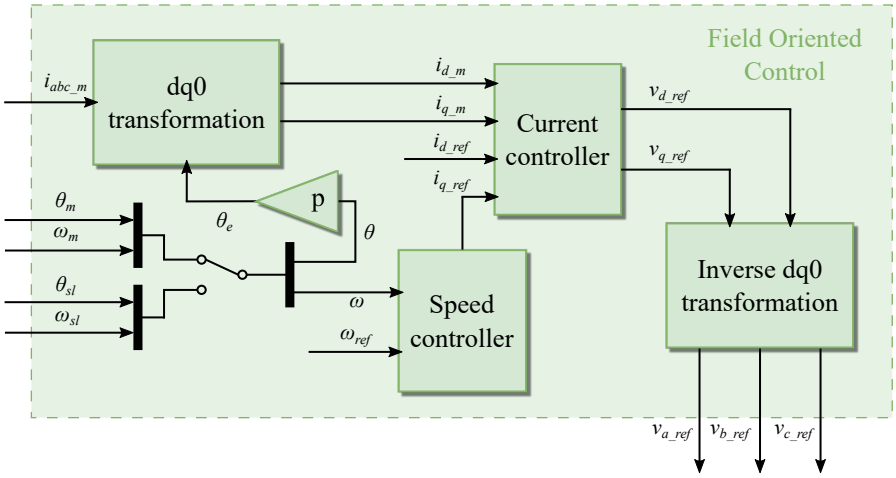

Figure 2.8: Field Oriented Control simulation model

controller actuates on the motor speed, trying to make it equal to the reference set by the user. The difference between reference and measured quantities will be used by a Proportional-Integral (PI) controller to produce an actuating signal that will affect the measured variable. Eventually, the difference will come down

to zero and the steady state has been reached. Therefore, one can write

$$i_{q\_ref}(t) = PI_{\omega}(K_{p\_\omega}, K_{i\_\omega})e_{\omega}(t) = K_{p\_\omega}e_{\omega}(t) + K_{i\_\omega}\int e_{\omega}(t)dt, \tag{2.17}$$

where i_{q_ref} is the quadrature reference current and e_{ω} is the speed error signal. The term PI_{ω} refers to the function of the PI controller, that is dependent of the two constants K_{p_ω} and K_{i_ω}. The speed error signal is obtained as

$$e_{\omega}(t) = \omega_{ref}(t) - \omega_{m}(t). \tag{2.18}$$

The PI controller is modelled as a transfer function in the Laplace domain, as it was made in the machine modelling. Therefore, (2.17) can be expressed as

$$I_{q\_ref}(s) = \left(K_{p\_\omega} + K_{i\_\omega}\frac{1}{s}\right)E_{\omega}(s). \tag{2.19}$$

The output of the speed controller, $i_{q\_ref}(t)$, is the input of the current controller, along with the d-current reference and the measured currents transferred to the rotor frame, i_{d_m} and i_{q_m}. As it was stated when (2.7) was introduced, the current in the q-axis is the main responsible for torque generation in the machine. Although the current in the d-axis has other applications, like to raise the speed over the nominal speed (field weakening operation), for the case under study only produces extra losses. Therefore, the current reference for the d-axis is set to 0, so to achieve constant torque angle fixed at 90 degrees. The measured currents are compared to the references, and error signals are generated for the current regulators PI controllers following the next expressions

$$\begin{aligned}
V_{d_ref}(s) &= \left(K_{p_i_d} + K_{i_i_d}\frac{1}{s}\right)E_{i_d}(s) \\
V_{q_ref}(s) &= \left(K_{p_i_q} + K_{i_i_q}\frac{1}{s}\right)E_{i_q}(s) \\
E_{i_d}(s) &= I_{d_ref}(s) - I_{d_m}(s) \\
E_{i_q}(s) &= I_{q_ref}(s) - I_{q_m}(s)
\end{aligned} \tag{2.20}$$

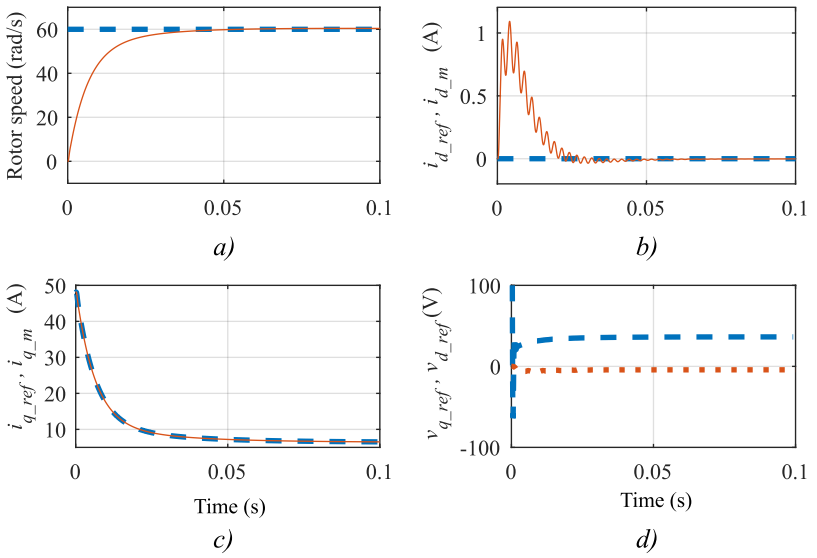

Figure 2.9: Simulation waveforms showing the functioning of the FOC model. a) Speed reference (dashed blue) and motor speed (solit orange). b) i_{d_ref} (dashed blue) and i_{d_m} (solid orange) currents. c) i_{q_ref} (dashed blue) and i_{q_m} (solid orange) currents. d) v_{q_ref} (dashed blue) and v_{d_ref} (dotted orange) voltage references

Finally, the voltage reference are generated transferred the field voltages references to the stator reference frame

$$\begin{bmatrix} v_{\alpha\_ref} \\ v_{\beta\_ref} \end{bmatrix} = [P]^{-1} \begin{bmatrix} v_{d\_ref} \\ v_{q\_ref} \end{bmatrix} = \begin{bmatrix} \cos\theta_e & -\sin\theta_e \\ \sin\theta_e & \cos\theta_e \end{bmatrix} \begin{bmatrix} v_{d\_ref} \\ v_{q\_ref} \end{bmatrix} \tag{2.21}$$

$$\begin{bmatrix} v_{a\_ref} \\ v_{b\_ref} \\ v_{c\_ref} \end{bmatrix} = [C]^{-1} \begin{bmatrix} 0 \\ v_{\alpha\_ref} \\ v_{\beta\_ref} \end{bmatrix} = \sqrt{\frac{2}{3}} \begin{bmatrix} \frac{1}{\sqrt{2}} & 1 & 0 \\ \frac{1}{\sqrt{2}} & -\frac{1}{2} & \frac{\sqrt{3}}{2} \\ \frac{1}{\sqrt{2}} & -\frac{1}{2} & -\frac{\sqrt{3}}{2} \end{bmatrix} \begin{bmatrix} 0 \\ v_{\alpha\_ref} \\ v_{\beta\_ref}. \end{bmatrix} \tag{2.22}$$

The operation of the FOC simulation model can be observed in Figure 2.9. When a speed reference is set, the difference with the measured speed (Figure 2.9 a)) will be fed to the PI controller and it will generate an i_{q_ref} (Figure 2.9 c)) This reference, along with the i_{d_ref} that equals 0, will be compared

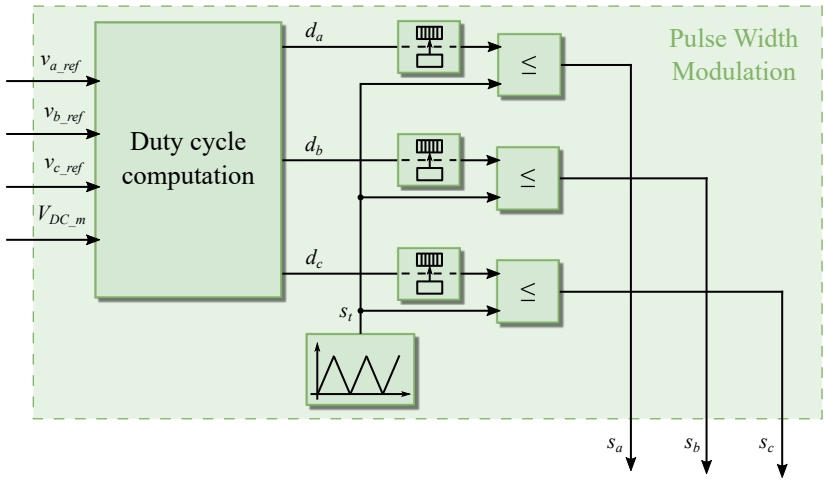

Figure 2.10: PWM simulation scheme

with their measured counterparts and the error used in the current PI controllers (Figure 2.9 b and Figure 2.9 c))). Finally, the controllers output will be the voltage references in the dq reference frame (Figure 2.9 d)).

2.2.3.2 Pulse Width Modulation

In order to generate the gate signals needed by the inverter, PWM is used and its general scheme is shown in Fig 2.10. The duty cycles are generated by reducing the voltage references in amplitude so their values are in the interval $v_{abc\_ref} \in (0, 1)$ and centered at 0.5 following the expression

$$d_{abc} = \begin{bmatrix} d_a \\ d_b \\ d_c \end{bmatrix} = \frac{1}{2} + \frac{1}{V_{DC}} \begin{bmatrix} v_{a\_ref} \\ v_{b\_ref} \\ v_{c\_ref} \end{bmatrix}. \tag{2.23}$$

Once the duty cycles are computed, the switching signals for the inverter are generated by comparing the duty cycles with a triangular wave. However, since the switching signals are used by the rest of the simulation model at a higher

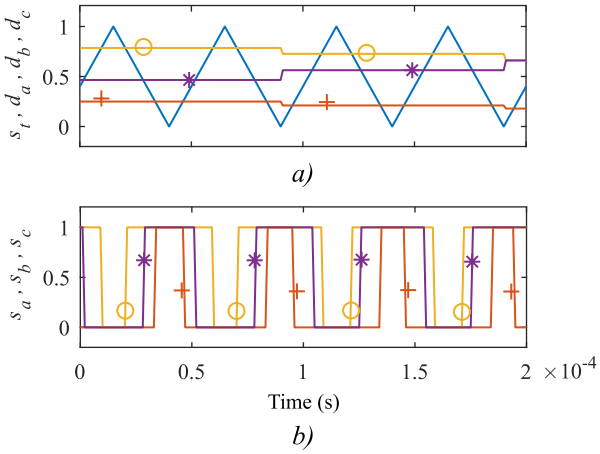

Figure 2.11: PWM waveforms from the simulation model. a) Triangular wave signal (solid blue) and duty cycles for phases a (yellow with hollow circle markers), b (purple with asterisks markers) and c (red with plus markers). b) Switching signals generated for the three phases (same markers and colors as in a))

sampling rate, the duty cycles must be oversampled. Nevertheless, Simulink takes care of that by inserting rate transition blocks. The triangular wave is characterized by the following expression

$$s_t = \begin{cases} \dfrac{1}{T_c/2}t & 0 \leq t \leq T_c/2 \\ -\dfrac{1}{T_c/2}t + 2 & T_c/2 < t \leq T_c \end{cases} \tag{2.24}$$

where T_c is the switching time selected for the inverter. The switching signals for branch a, for instance, are generated using the comparison

$$s_a = \begin{cases} 1 & d_a \leq s_t \\ -1 & otherwise \end{cases} \tag{2.25}$$

The model developed for the PWM control of the inverter computes signals as the ones depicted in Figure 2.11. In this example, $T_c = 5 \times 10^{-5}$ s while the duty cycles updates each $T_s = 10^{-4}$ s. Figure2.11 a) shows the triangular wave

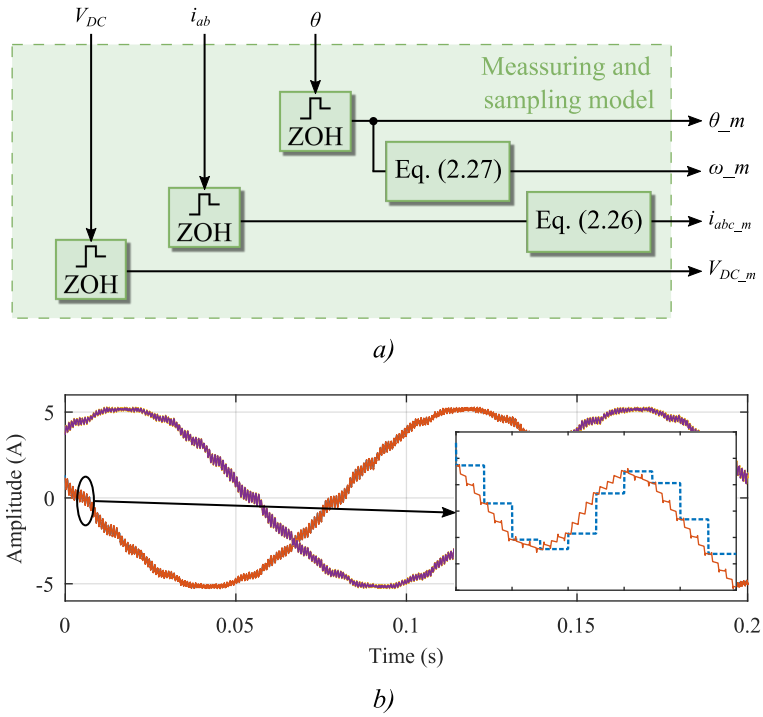

Figure 2.12: Meassuring and sampling in simulation. a) Simulation model of the sampling process. b) Simulation results showing the sampling process. In the detailed view, the real signal is depcted with solid orange line, the sampled one is in dashed blue

s_t along with the duty cycles d_{abc} and Figure 2.11 b) the switching signals s_{abc} generated following (2.25).

2.2.4 Meassures and sampling modelling

The meassures and sampling model will simulate de conversion of the analog signals to digital signals which the control platform can meassure and operate with. It downsamples the measured varibles and reconstruct the third current,

given that in a balanced three-phase system the following holds

$$\begin{aligned} i_a + i_b + i_c &= 0 \\ i_c &= -\left(i_a + i_b\right). \end{aligned} \tag{2.26}$$

Moreover, the speed is computed from the meassured rotor position simply as

$$\omega_m = \frac{d\theta_m}{dt}. \tag{2.27}$$

The model implemented is presented in Figure 2.12 a), and consists in zero-order hold. The sampling time in the sensorless and control models will be significantly lower compared to the one employed in the rest of the system. The main reason is to guarantee a transition to experimental procedures as smooth as it is possible, since the control algorithm can be heavy on resources and the control platform used could not be able to run it properly. This effect is demonstrated in Figure 2.12 b), where the sampling of two currents is done. In the detailed view, it can be oberved how the sampling interval is some orders of magnitude lower. For that simulation, the main sampling time is 10^{-6} s while the sampling interval is 10^{-4} s.

Another issue that the sampling brings forward is the need of having a sampling frequency fast enough for the application at hand. The sensorless techniques under study in this work will inject a high frequency signal to the machine. Moreover, their accuracy and performance depend on the quality of the signal recovered. This is also depicted in Figure 2.12 b), where it can be observed that along with the fundamental current of higher amplitude, there is a smaller one with a much higher frequency. Knowing that in the example the sampling rate is 10^{-4} s, and that in half period one is able to count 4 different values, it can be deduced that the high frequency current has a frequency of 1250 Hz. According to Nyquist sampling theorem, the sampling frequency has to be at least twice the higher frequency of the highest frequency signal sampled. This will ensure

that no aliasing will occur to the meassured signals. However, in order to have enough margin for a good reconstruction of a signal, specially for a sinusoidal one, at least 4 points are needed. Putting it in other words, one should at least have $T_s/T_{sc} = 4$, being T_s the fundamental sample time for the simulation, and T_{sc} the sampling time used for the control and sensorless algorithms.

2.2.5 Sensorless algorithm

The sensorless model will provide estimations for the rotor angle and speed, by injecting a high frequency voltage into the machine. This leds to a high frequency current that is modulated with the rotor position. The information is then recovered and used for generating the estimations. This section will use complex vectors and different reference frames. In order to transfer variables from one frame to another, the Park transform introduced in 2.2.1 will be used, but in the exponential form. In general, one can write

$$\begin{aligned} [P] &= \begin{bmatrix} \cos\theta & \sin\theta \\ -\sin\theta & \cos\theta \end{bmatrix} \equiv e^{-j\theta} \\ [P]^{-1} &= \begin{bmatrix} \cos\theta & -\sin\theta \\ \sin\theta & \cos\theta \end{bmatrix} \equiv e^{j\theta}. \end{aligned} \tag{2.28}$$

2.2.5.1 Pulsating sinusoidal injection

In this sensorless scheme, the high frequency voltage is injected in the synchronous reference frame, following the expression

$$\boldsymbol{u_c^{\hat{R}}} = U_c \cos(\omega_c t) \tag{2.29}$$

where U_c is the injection voltage's peak value and ω_c is the high frequency pulsation. The superscript $\hat{R}$ indicates that is a variable expressed in the estimated rotor's reference frame, and the bold notation that is a complex vector. The cosine function implies that the amplitude of the injected voltage will fluctuate

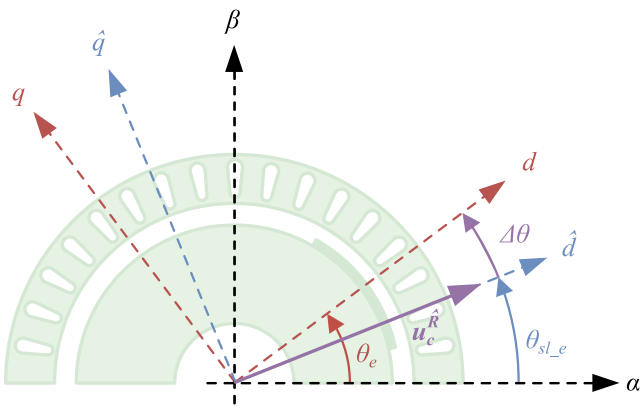

Figure 2.13: Vector diagram of the voltage injection and different reference frames

following

$$\left|\boldsymbol{u}_{\boldsymbol{c}}^{\hat{\boldsymbol{R}}}\right| \in [-U_c, U_c] \tag{2.30}$$

This means that the vector defined by (2.29) is pulsating along the direct axis of the frame defined by the estimated angle, as it is depicted in Fig. 2.13. If the vector is transferred to the stator reference frame, (2.29) becames

$$\boldsymbol{u}_{\boldsymbol{c}}^{\boldsymbol{S}} = \boldsymbol{u}_{\boldsymbol{c}}^{\hat{\boldsymbol{R}}} e^{j\theta_{sl\_e}} = U_c \cos(\omega_c t) e^{j\theta_{sl\_e}}, \tag{2.31}$$

where θ_{sl_e} is the estimated rotor angle in electrical radians. The superscrip S indicates that is a variable in the stator reference frame, i.e., the $\alpha\beta\gamma$ reference frame introduced in section 2.2.1. If (2.31) is transferred to the real rotor reference frame, defined by the rotor's real angle θ_e, one can have

$$\boldsymbol{u}_{\boldsymbol{c}}^{\boldsymbol{R}} = \boldsymbol{u}_{\boldsymbol{c}}^{\boldsymbol{S}} e^{-j\theta_e} = U_c \cos(\omega_c t) e^{j(\theta_{sl\_e} - \theta_e)}. \tag{2.32}$$

Recalling (2.1) and taking into account that the voltage applied is (2.32), the following differential equations can be derived

$$U_c \cos(\omega_c t) e^{j(\theta_{sl\_e} - \theta_e)} = L_s \frac{d\boldsymbol{i_c^R}}{dt}. \tag{2.33}$$

For (2.33) to hold, some assumptions are made:

- The rotor speed ω is low enough so the voltage part depending on the fluxes (magnet and current-produced) can be neglected, i.e., one focuses in the low speed region fore sensorless operation.
- The frequency of the voltage injected is high enough so the resistive voltage drop can also be neglected, compared to the inductive voltage drop.
- The inductances considered are only the fundamental ones and there is no mutual inductance terms, i.e., $L_{dq} = L_{qd} = 0$.

In order to solve (2.33), real and imaginary components are separated and so one can write

$$\begin{aligned} \Re(\boldsymbol{i_c^R}) &= i_{cd}^R \\ \Im(\boldsymbol{i_c^R}) &= i_{cq}^R, \end{aligned} \tag{2.34}$$

where i_{cd}^R and i_{cq}^R are the real and imaginary components of i_c^R, respectively. This leads to the following pair of equations, applying (2.34) to (2.33)

$$\begin{aligned} L_d \frac{di_{cd}^R}{dt} &= U_c \cos(\omega_c t) \cos\left(\theta_{sl\_e} - \theta_e\right) \\ L_q \frac{di_{cq}^R}{dt} &= U_c \cos(\omega_c t) \sin\left(\theta_{sl\_e} - \theta_e\right). \end{aligned} \tag{2.35}$$

Solving these equations by integrating leads to

$$\begin{aligned} i_{cd}^R &= \int \left(\frac{U_c}{L_d} \cos(\omega_c t) \cos\left(\theta_{sl\_e} - \theta_e\right) \right) dt \\ i_{cq}^R &= \int \left(\frac{U_c}{L_q} \cos(\omega_c t) \sin\left(\theta_{sl\_e} - \theta_e\right) \right) dt, \end{aligned} \tag{2.36}$$

whose solutions are

$$\begin{aligned} i_{cd}^{R} &= \frac{U_c}{L_d \omega_c} \sin(\omega_c t) \cos\left(\theta_{sl\_e} - \theta_e\right) \\ i_{cq}^{R} &= \frac{U_c}{L_q \omega_c} \sin(\omega_c t) \sin\left(\theta_{sl\_e} - \theta_e\right). \end{aligned} \tag{2.37}$$

It is worth noting that in (2.36) the electrical angle of the rotor and its estimation, θ_{sl} and θ_{sl_e}, are also time dependent. However, since the period of the high frequency signal is much higher than the rotation period, they can be regarded as constant. Thus, the solution of (2.33) can be formed using (2.37) as

$$\boldsymbol{i_c^R} = i_{cd}^{R} + j i_{cd}^{R} = \frac{U_c}{\omega_c} \sin(\omega_c t) \left(\frac{1}{L_d} \cos\left(\theta_{sl\_e} - \theta_e\right) + j \frac{1}{L_q} \sin\left(\theta_{sl\_e} - \theta_e\right) \right), \tag{2.38}$$

which can be expressed as complex space vectors using Euler's formula as

$$\begin{aligned} \boldsymbol{i_c^R} = \frac{U_c}{\omega_c} \left(\frac{e^{j\omega_c t} - e^{-j\omega_c t}}{2j} \right) \Bigg[\frac{1}{L_d} \Bigg(\frac{e^{j(\theta_{sl\_e} - \theta_e)} + e^{-j(\theta_{sl\_e} - \theta_e)}}{2} \\ + \frac{1}{L_d} \left(\frac{e^{j(\theta_{sl\_e} - \theta_e)} - e^{-j(\theta_{sl\_e} - \theta_e)}}{2j} \right) \Bigg] . \end{aligned} \tag{2.39}$$

By operating and grouping terms one can get

$$\begin{aligned} \boldsymbol{i_c^R} = \frac{U_c}{4jL_dL_q} \Big[(L_d + L_q) e^{j(\omega_c t + \theta_{sl\_e} - \theta_e)} - (L_d - L_q) e^{j(\omega_c t + \theta_e - \theta_{sl\_e})} \\ - (L_d + L_q) e^{j(\theta_{sl\_e} - \theta_e - \omega_c t)} + (L_d - L_q) e^{j(\theta_e - \theta_{sl\_e} - \omega_c t)} \Big] \end{aligned} \tag{2.40}$$

Finally, transferring (2.40) back to the stator frame yields

$$\begin{aligned} \boldsymbol{i_c^S} = \boldsymbol{i_c^R} e^{j\theta_e} = \frac{U_c}{4j\omega_c L_d L_q} \Big[(L_d + L_q) e^{j(\omega_c t + \theta_{sl\_e})} \\ - (L_d - L_q) e^{j(\omega_c t + 2\theta_e - \theta_{sl\_e})} - (L_d + L_q) e^{j(\theta_{sl\_e} - \omega_c t)} \\ + (L_d - L_q) e^{j(2\theta_e - \theta_{sl\_e} - \omega_c t)} \Big] \end{aligned} \tag{2.41}$$

Equation (2.41) represents the stator currents as measured by the current sensors of the systems. It can be noted that the vector current is made of four different vectors. The dominant term in the angle component is the injection

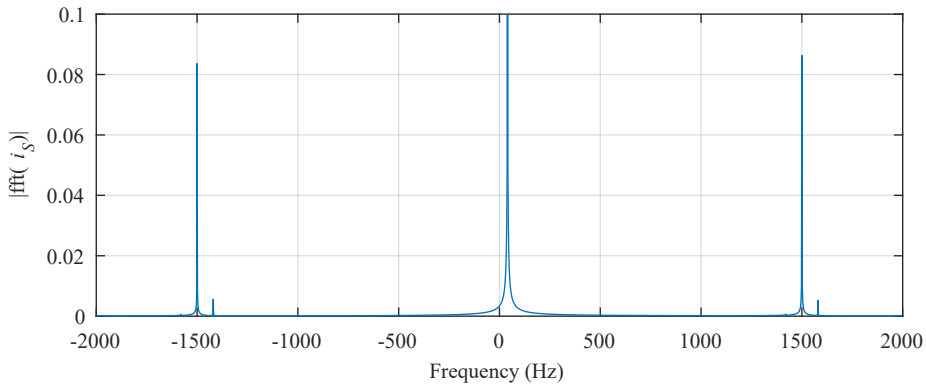

Figure 2.14: Frequency spectrum of the high frequency injection current

pulsation. Hence, two of them rotate in the positive direction and the other two in the negative direction. This situation is depicted in Figure 2.14.

In addition, as it can be observed in Figure 2.14, two of the components are proportional to the sum of the inductances, while the other two are proportional to the difference. It can be noted that the real angle of the rotor is contained in the angle of the vectors whose magnitude is proportional to the differential inductance, i.e., $L_d - L_q$. This fact gives an idea of the difficulty of estimating the rotor position in a surface mounted permanent magnet machine, where both inductances take similar values.

If the currents represented by (2.41) are transferred to a frame rotating at a speed defined by $\omega_c t + \theta_{sl\_e}$ the following is obtained

$$\begin{aligned} \boldsymbol{i_c^{\omega_c t+\theta_{sl\_e}}} = \boldsymbol{i_c^S} e^{-j(\omega_c t+\theta_{sl\_e})} = \frac{U_c}{4j\omega_c L_d L_q} \left[(L_d + L_q)\right. \\ - (L_d - L_q)e^{j(2\theta_e - 2\theta_{sl\_e})} - (L_d + L_q)e^{j(-2\omega_c t)} \\ \left. +(L_d - L_q)e^{j(2\theta_e - 2\theta_{sl\_e} - 2\omega_c t)}\right]. \end{aligned} \tag{2.42}$$

From 2.42 one can see that two components are displaced to very high frequencies, while retaining the information of the rotor position at low frequencies. The error

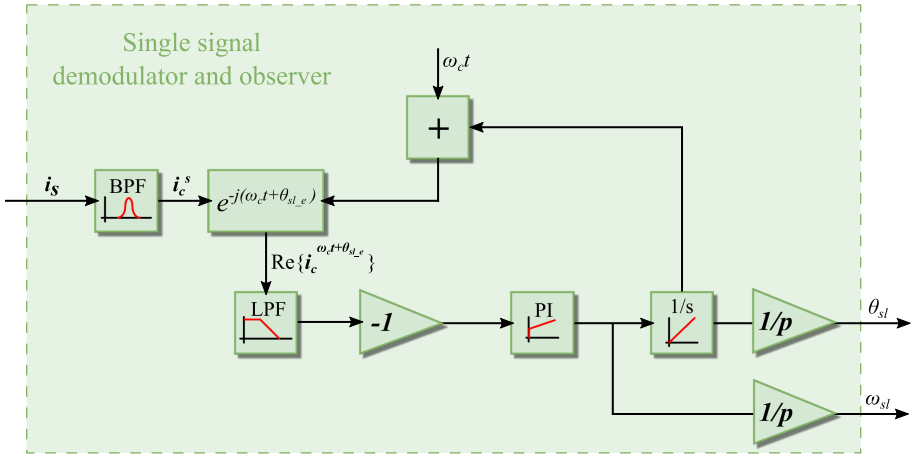

Figure 2.15: Observer for estimating position using one signal

committed is defined as $\Delta\theta_e = \theta_e - \theta_{sl\_e}$, as shown in Figure 2.13. Therefore, (2.42) can be rewritten as

$$\boldsymbol{i_c^{\omega_c t+\theta_{sl\_e}}} = -\frac{U_c}{2\omega_c L_d L_q}\left[(L_d - L_q)\Delta\theta_e + jL_q\right]. \tag{2.43}$$

As (2.43) shows, the real part of this current is proportional to the error in the estimation of the rotor. Note that only the low frequency terms are represented, the high frequency terms can be filtered out using a Low Pass Filter (LPF). Thus, forcing the real part of this signal to be zero would result in $\theta_e = \theta_{sl\_e}$.

In order to achieve a correct estimation, (2.42) can be used by a tracking observer in order to estimate the rotor position. Such a tracking observer can take the form of the one depicted in Figure 2.15. The high frequency current vector $\boldsymbol{i_c^S}$ is separated from the total current vector measured from the machine, $\boldsymbol{i^S}$, by means of a Band Pass Filter (BPF). The carrier current vector is then transferred to a reference frame rotating at $\omega_c t + \theta_{sl\_e}$. The real part is filtered

to retain the low frequency content, and then multiplied by -1 before feeding it to the PI controller. When the input of the controller is 0, the estimation will be correct and the output will be the rotor speed.

The use of filters represents another important fact, that is the increment of phase lag in the signal filtered. This introduces a source of error in the estimation of the rotor angle that will be corrected afterwards. The BPF is designed as a concatenation of a LPF and a High Pass Filter (HPF). The cut-off frequency of each filter,f_c, is selected accordingly in order to leave a window wide enough to allow a good recovery of the signal. Thus, one can write

$$\begin{aligned} f_{c\_LPF} &= f_c + w_f \\ f_{c\_HPF} &= f_c - w_f, \end{aligned} \tag{2.44}$$

where w_f is the width of the band allowed in the filter. Figure 2.16 represents the bode diagram of this kind of filter, where $f_c = 1500$ Hz and $w_c = 200$ Hz. Note that the attenuation of the amplitude at frequencies around the cut-off frequency is almost zero, whereas the lag is not as small. Moreover, the lag phase is not symmetrical around the cut-off frequency (the window is symmetrical, it does not seem so in Figure 2.16 due to logarithmic scale). Nevertheless, since the components of the signal represented by (2.43) will be located at different frequencies depending on the rotor speed, there will always be a speed-dependent phase lag that will need correction.

Another conclusion driven by (2.43) is that the signal recovered is directly proportional to the injection voltage, but inversely proportional to the injection frequency. It is desirable to lower the injection voltage as much as possible, since it is a source of noise and losses. As for the injection frequency, the closer it is to the FOC operation frequencies, the higher impact it will have on the system performance. It is clear that, in order to be able to do both things, and still

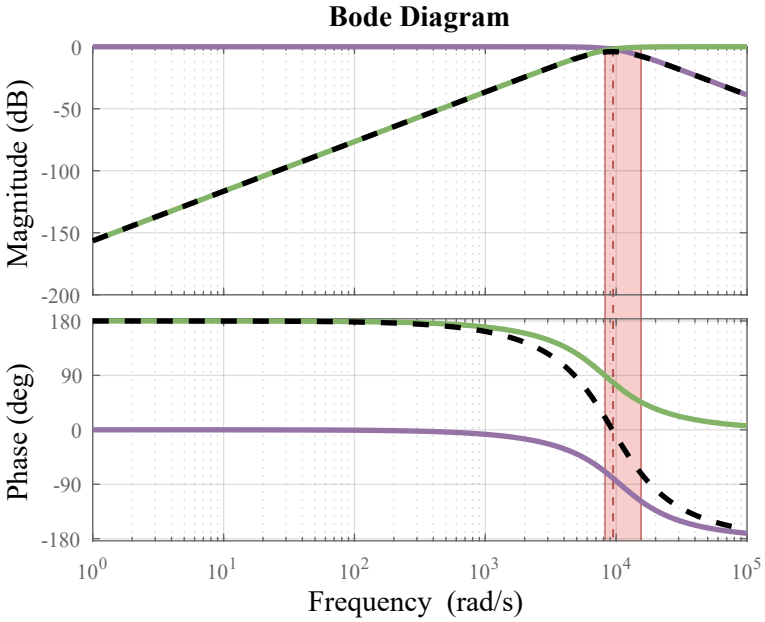

Figure 2.16: Bode diagram of the LPF,HPF and BPF. The green line represents the LPF, the purple line the HPF, and the resultant BPF in dashed black. The dashed red line represents the cut-off frequency (1500 Hz) and the solid red lines represent the width of the window ($2\omega_c = 400$ Hz)

have a reasonable signal to noise ratio for the sensorless algorithm to work, all information available in (2.42) should be used.

2.2.5.2 Enhanced demodulation

Similarly as it was done in (2.43), one can extract the rotor position from the other component in (2.42) containing it. To do so, this last expression is taken to a reference frame rotating at $-\omega_c t + \theta_{sl\_e}$ resulting in

$$\begin{aligned} \boldsymbol{i_c^{-\omega_c t+\theta_{sl\_e}}} = \boldsymbol{i_c^S} e^{-j(-\omega_c t+\theta_{sl\_e})} = \frac{U_c}{4j\omega_c L_d L_q} \left[-(L_d+L_q)\right. \\ + (L_d - L_q)e^{j(2\theta_e - 2\theta_{sl\_e})} + (L_d+L_q)e^{j(-2\omega_c t)} \\ \left. -(L_d - L_q)e^{j(2\theta_e - 2\theta_{sl\_e} - 2\omega_c t)}\right]. \end{aligned} \tag{2.45}$$

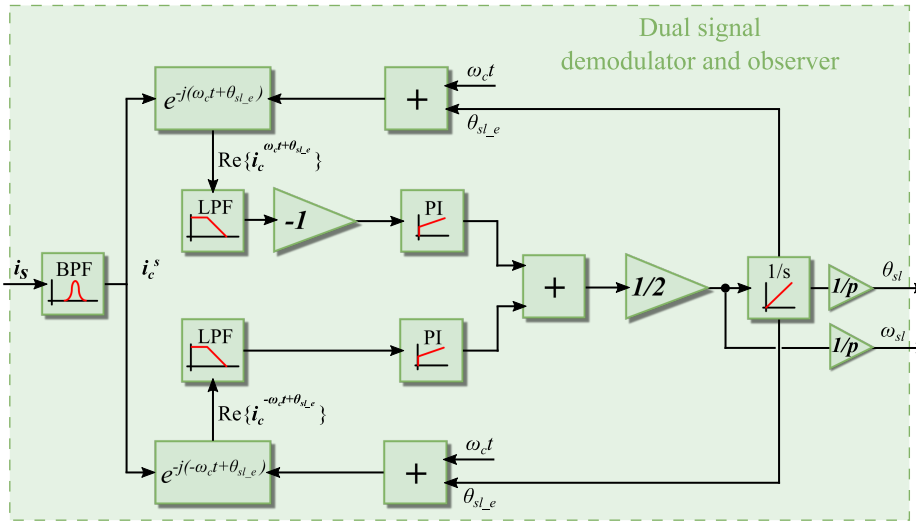

Figure 2.17: Observer for estimating the position using both signals

Again, if we retain only the low frequency content and further develop the expression, (2.45) can be expressed as

$$\boldsymbol{i_c^{-\omega_c t+\theta_{sl\_e}}} = -\frac{U_c}{2\omega_c L_d L_q}\left[(L_d - L_q)\Delta\theta_e + jL_q\right]. \tag{2.46}$$

The signal represented by (2.46) can be used together with (2.43) for estimating the rotor position. An observer for such a purpose is depicted in Figure 2.17. Note that the only difference between the demodulation applied to (2.43) and (2.46) is a minus gain after transferring both signals to the adequate reference frame. This will have the advantage of cancelling out extra noise in both components, as it will be seen in the following simulations.

In order to illustrate the functioning of the sensorless scheme, the first simulation conducted will be a simplified version that will not include the speed controller or the inverter. Thus, direct references will be given for the v_{α_ref} in order to rotate the rotor to a certain position. The voltages given to the machine

Parameter	Description	Value
L_d	Direct-axis inductance	1.616×10^{-3} H
L_q	Quadrature-axis inductance	1.871×10^{-3} H
R_s	Stator resistance	0.7 Ω
λ_m	Rotor magnet flux	0.1323 Vs/rad
J	Rotor inertia	3.6×10^{-3} kgm^2
F_r	Rotor friction coefficient	2.25×10^{-3} Ns

Table 2.3: PMSM parameters used for simulation

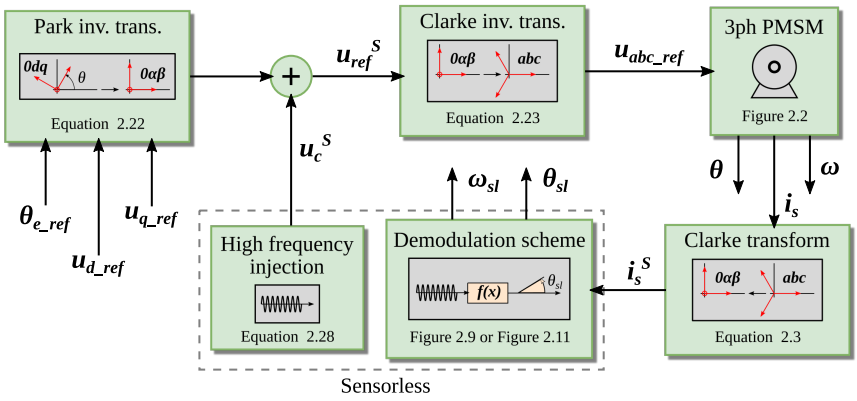

Figure 2.18: Simplified simulation scheme for sensorless testing

will be the references, assuming that the inverter ideally transforms references into real voltages. Such simulation scheme can be observed in Figure 2.18 and the PMSM parameters for the simulation are gathered in Table 2.3. As it was stated previously, the rotor will align with the angle θ_{e_ref}. This is achieved by supplying a constant positive and non-zero value to u_{d_ref} and by setting $u_{q\_ref} = 0$. The result of transferring the resulting voltage vector to the stator coordinates plus the injection voltage vector is u^S_{ref}. Note that the sensorless model uses the estimated angle to transfer the injection vector (2.29) from the estimated rotor reference frame to the stator reference frame (2.31). This situation is depicted

Parameter	Description	Value
T_s	Fundamental step time	10^{-4} s
u_{d_ref}	Direct-axis voltage reference	5 V
u_{q_ref}	Quadrature-axis voltage reference	0 V
θ_{ref}	Electrical angle reference	$\pi/3$ rad
U_c	Injection voltage's magnitude	3 V
fc	Injection voltage's frequency	1250 Hz
f_{LPF}	Cut-off frequency of the LPF	500 Hz
k_{p_sl}	Proportional gain of the estimation PI controller	1000
k_{i_sl}	Integral gain of the estimation PI controller	10000

Table 2.4: Simulation parameters used in simulation depicted in Figure 2.18

in Figure 2.19, and the main simulation's parameters are shown in Table 2.4. In $t = 0.1$ s the angle reference θ_{ref} changes from 0 to its final value, $\pi/3$ radians, as it can be seen in Figure 2.19 c). At this moment, it can be seen how the voltage references, although constant, vary seen from the rotor's reference frame, due to the difference between θ_{ref} and θ (Figure 2.19 a and Figure 2.19 b)). Moreover, the injected voltage, although only injected in the direct axis, it is present in the quadrature axis until the estimation equals the real rotor angle.

The functioning of the sensorless scheme proposed in Figure 2.17 compared to the single demodulation scheme of Figure 2.15 is depicted in Figure 2.20. If we were to use only one of the two signals for demodulating the rotor positions, the results would be the ones showed in the Figure 2.20 a), marked in yellow or purple, depending in the rotation direction. The estimated mechanical angles θ_{sl}^{+} and θ_{sl}^{-} are obtained using the single demodulation from Figure 2.15 applied to both (2.43) and (2.46) respectively. It can be observed whow they converge to the wrong value initially, although they react to rotor position changes. This can be exploited using the dual signal observer, obtaining the signal labeled as θ_{sl} (green with cross markers). In Figure 2.20 b) the errors are shown confirming

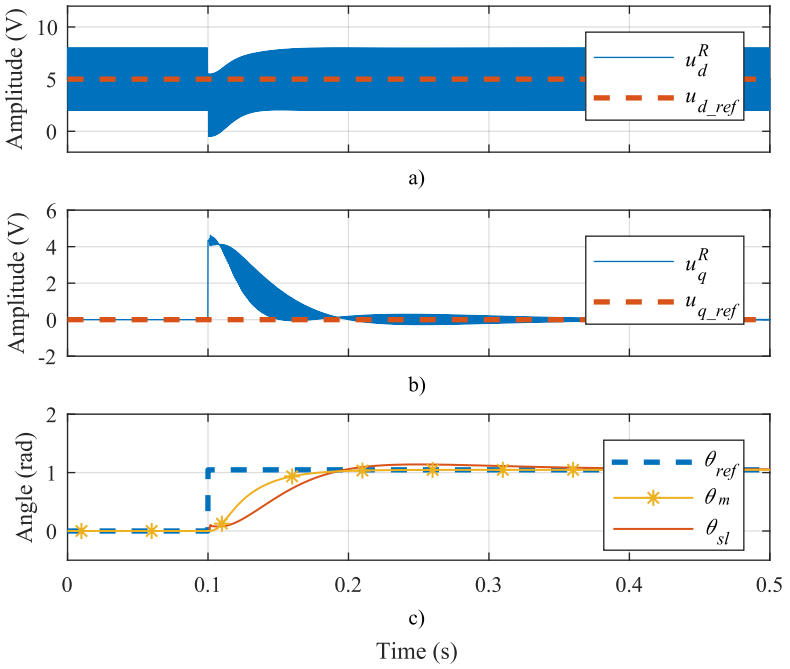

Figure 2.19: Simulation results using the simulation represented in Figure 2.18. a) Direct-axis voltage reference (dashed orange) and machine's voltage (solid blue). b) Quadrature-axis voltage reference (dashed orange) and machine's voltage (solid blue). c) Reference angle (dashed blue), machine's mechanical angle (yellow with asterisks markers) and estimated angle (solid orange)

that by using both signals, the correct position is estimated.

2.2.5.3 Full system simulation

For the next simulation, the power electronics and the FOC are implemented as well. This will allow to test the sensorless scheme under a more realistic situation. The simulations follow the scheme depicted in Figure 2.21. It uses the PMSM parameters displayed in Table 2.3, as well as the ones gathered in Table 2.5. Note that there is a difference between the fundamental step time and the control step

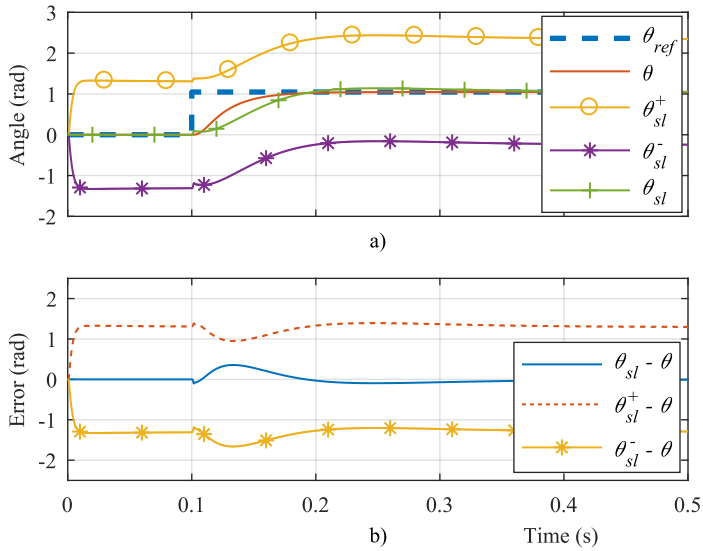

Figure 2.20: Angle estimations using the simulation represented in Figure 2.18. a) Reference angle (solid blue), machine's angle (dashed orange), estimated angle from positive sequence signal (yellow with circle markers), estimated angle from negative sequence signal (purple with filled circle markers) and dual signal estimated angle (green with cross markers). b) Error signals: dual estimation error solid blue), positive signal estimation error (dashed orange) and negative signal estimation error (yellow with filled circle markers)

time of two orders of magnitude. The reason is that the power electronics and the motor models will be running faster than the control itself, as it was explained in section 2.2.4.

Figure 2.22 shows the demodulation of the carrier signal by the sensorless control proposed, as well as the speed estimation. Figure 2.22 a) shows the carrier current in the stator coordinates i^S_C, as recovered by the BPF from the motor currents. It is interesting to note here how the high frequency currents is modulated in amplitude with the rotor position. Recalling (2.41), one can see how the terms with larger amplitde, i.e. the ones proportional to the sum of

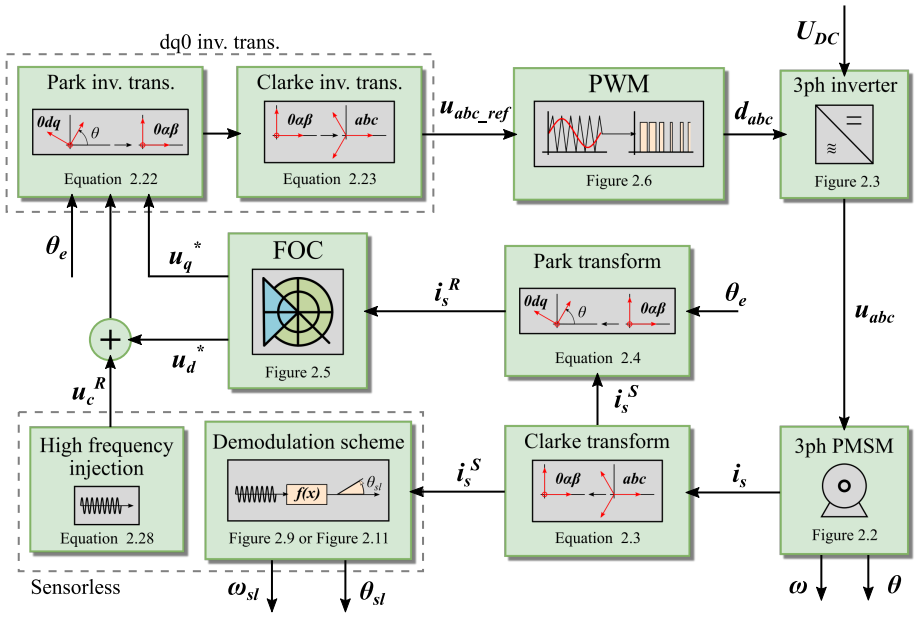

Figure 2.21: Sensorless simulation scheme

direct and quadrature inductances, are also proportional to $e^{j(\omega_c t+\theta_{sl\_e})}$, hence the amplitude modulation. In the detailed view of the right it can be observed how the sinusoidal wave is recovered using 8 points por period. As it was stated before, rising the injection frequency could compromise this step.

Figure 2.22 b) and Figure 2.22 c) depicts the same signal as Figure 2.22 a), once it is transferred to the positive and negative reference frames, $i_c^{\omega_c t+\theta_{sl\_e}}$ and $i_c^{-\omega_c t+\theta_{sl\_e}}$. Here it is also interesting to note from the magnified part of the figure how the components with higher amplitudes are displaced to even higher frequencies, being easier to remove the parts of the signal that does not contain the rotor position.

Lastly, Figure 2.22 d) shows the estimated rotor speed, ω_{sl}, computed using the previous signals as described by the Figure 2.17. The figure displays the

Parameter	Description	Value
T_s	Fundamental step time	10^{-6} s
T_{sc}	Control step time	10^{-4} s
ω_{ref}	Speed reference	100 rpm
U_c	Injection voltage's magnitude	5 V
fc	Injection voltage's frequency	1250 Hz
f_{LPF}	Cut-off frequency of the LPF	1500 Hz
f_{c_BPF}	Cut-off frequency of the BPF	1500 Hz
b_{BPF}	Band pass of the BPF	200 Hz
k_{p_sl}	Proportional gain of the estimation PI controller	1000
k_{i_sl}	Integral gain of the estimation PI controller	10000
k_{p_ω}	Proportional gain of the speed loop PI controller	0.2
k_{i_ω}	Integral gain of the speed loop PI controller	1
$k_{p\_i_d}$	Proportional gain of the d-axis current PI controller	4.68
$k_{i\_i_d}$	Integral gain of the d-axis current PI controller	46.8
$k_{p\_i_q}$	Proportional gain of the q-axis current PI controller	10
$k_{i\_i_q}$	Integral gain of the q-axis current PI controller	40

Table 2.5: Simulation parameters used in simulation depicted in Figure 2.21

start up of the rotor from standstill, and it can be observed that although the estimation of the speed is successfull, there is still quite high frequency content that could interfere with the speed controller. Thus, the output speed is filtered using a second order LPF, shown in orange in Figure 2.23

The sensorless scheme proposed is then employed to drive the motor controlled by the FOC, and the results are presented in Figure 2.23. Here, the control is run in a full sensorless mode, i.e the angle used for the FOC is the estimated one. Figure 2.23 a) and Figure 2.23 b) depict the current in rotor coordinates i_s^R. The reference for the d-axis current is set to 0, and the d-axis reference is given by the speed controller. The speed reference is given using a fast ramp to ensure a smooth acceleration profile, as shown in Figure 2.23 c). Here, also the measured and estimated are shown, proving a good tracking of the rotor. Lastly, the rotor

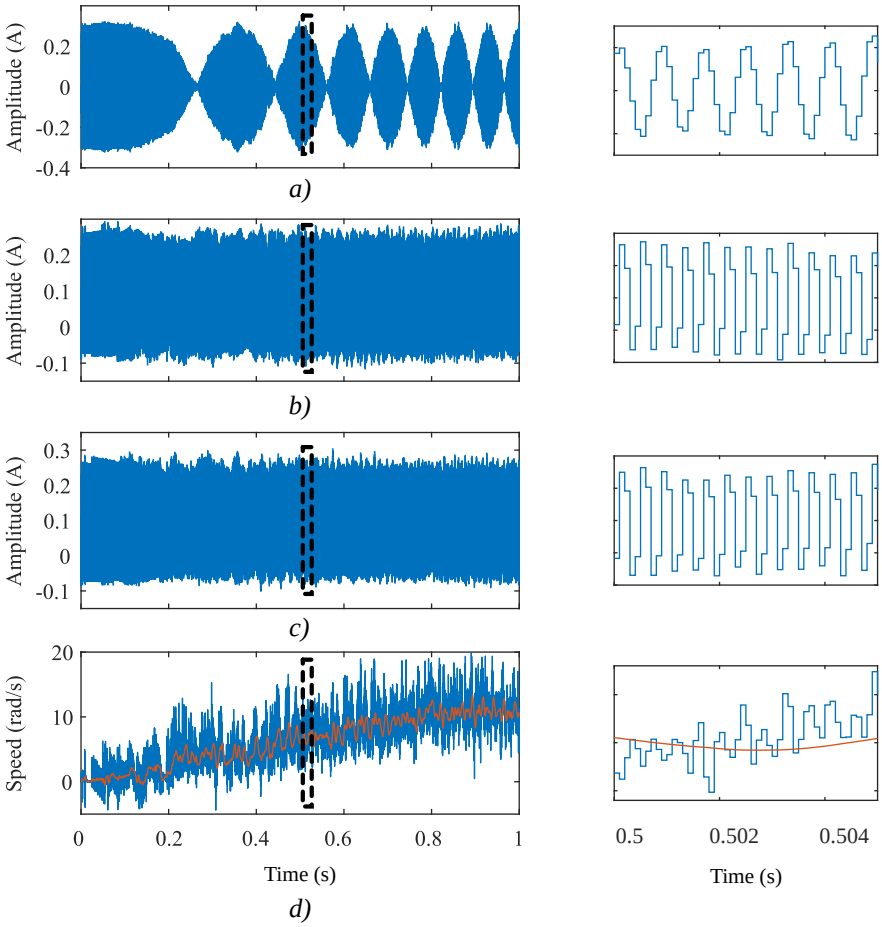

Figure 2.22: Simulation results of the proposed sensorless control. Magnified details of the waveforms on the right. a) High frequency carrier current $\boldsymbol{i_c^S}$, as recovered by the BPF. b) Positive rotative frame current $\boldsymbol{i_c^{\omega_c t+\theta_{sl\_e}}}$. c) Negative rotative frame current $\boldsymbol{i_c^{\omega_c t+\theta_{sl\_e}}}$ d) Estimated speed as computed (blue) and filtered (orange). ω_{sl}

angle, estimated and measured, can be observed in Figure 2.23 d), showing that close to zero angle error is committed.

An important fact that needs consideration is the DC bus voltage used for the

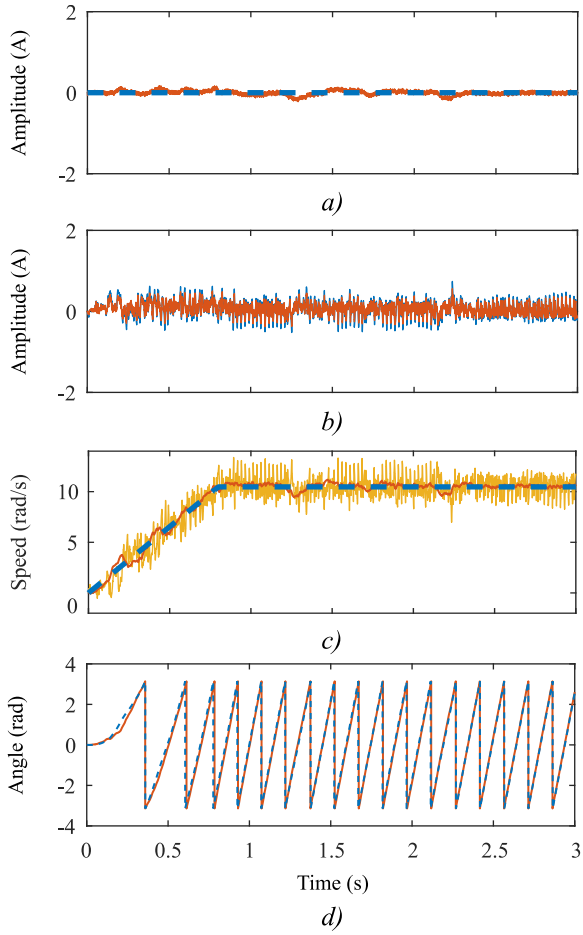

Figure 2.23: Simulation results of the FOC control using the sensorless scheme proposed. a) i_d reference (dashed blue) and measured (solid orange) current. b) i_q reference (dashed blue) and measured (solid orange) current. c) Rotor speed: reference (dashed blue), measured (orange) and estimated (yellow). d) Rotor angle measured (dashed blue) and estimated (solid orange)

system control. Figure 2.24 shows how different voltage levels affect the system ability to form the phase voltages according to the duty cycles commanded. In Figure 2.24 a), the duty cycles for the three branches are depicted, and one

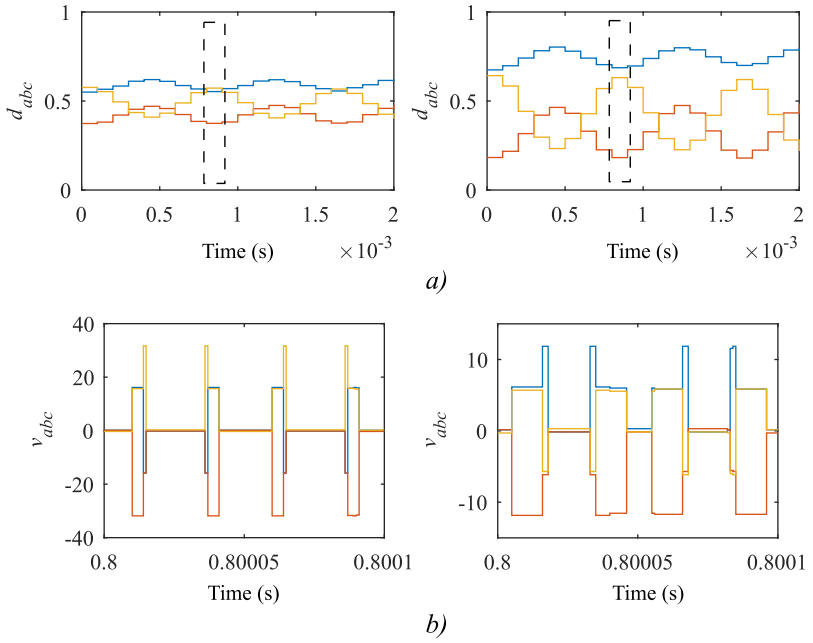

Figure 2.24: DC bus voltage influence on duty cycle and phase voltages . On the left figures, $V_{DC} = 20$ V and on the right ones, $V_{DC} = 50$ V. a) Duty cycles for the three branches. b) Phase voltages formed using the duty cycles marked inside a rectangle in a)

can notice how the amplitudes get smaller when the V_{DC} voltages is higher, in agreement with (2.23). This affects to the quality of the phase voltages formed using these duty cycles, showed in Figure 2.24 b). This, in turn, will affect the quality of the high frequency currents recovered from the machine. Therefore, the performance of the sensorless control will also be worsened. This can be observed in Figure 2.25), where the same speed reference is given to the system, only changing the V_{DC}. The difference in the performance is noticeable, having a much cleaner estimation speed and no oscillations when the V_{DC} is lower and the duty cycles are closer to 1.

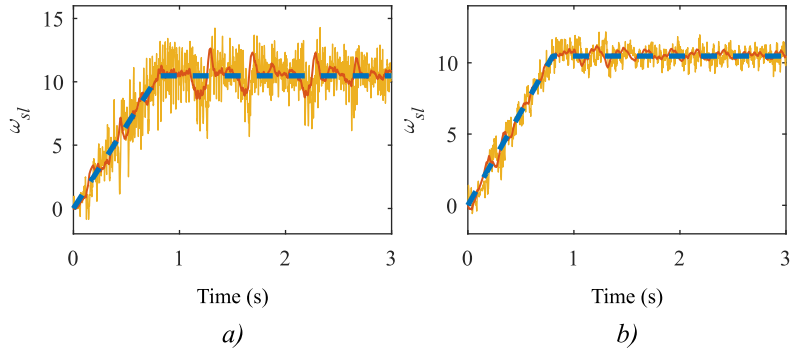

Figure 2.25: DC bus voltage influence on sensorless control performance. a) $V_{DC} = 50$ V. b) $V_{DC} = 20$ V

2.3 Experimental validation

The validation of the sensorless scheme developed is carried out by testing and comparing it to the traditional scheme under study. In this section, the control platform, testbench and results will be described and presented.

2.3.1 Control platform and testbench

The testbench used for the experiments is depicted in Figure 2.26. It is conformed of the following components:

- SMPMSM. The machine employed is a PMSM with surface mounted magnets, having the same parameters already presented in the simulation section (Table 2.3).

- Control platform. The control platform used in this work is a dSPACE MicrolabBox. It is in charge of running the control algorithms, meassuring and sampling the variables needed for the system, determine the rotor real position using the resolver included in the machine and generate the PWM signals for driving the inverter.

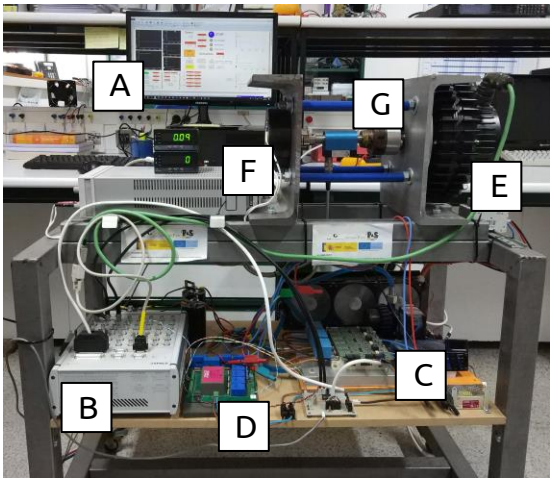

Figure 2.26: Testbench used for the experiments. A: PC running ControDesk software. B: dSPACE control platform. C: Inverter and drivers. D: Meassurements board. E: SPMSM. F: Electromagnetic brake and DC supply source. G: Torque meter

- PC with ControlDesk software. This software is used for interacting cirectly with the control platform, without the need of recompiling the code onto the platform. It allows faster development and tweaking of the system.

- Inverter and drivers. The inverter used is made up of three IGBT modules SKiM406GD066HD from SEMIKRON, while the driver is the SKiM63 Eval Driver. The DC power supply consists on a three-phase autotransformer connected to a three-branch diode bridge. The DC bus is made up of two 2.2 mF capacitors in series, connected to the inverter, as it was described in Figure 2.5 a).

- Meassuring board. In order to meassure the variables we are interested in with the control platform, there is a need of signal conditioning. Current variables are converted to voltages by means of LEM LA-25 current

transducers, and the voltages levels are lowered to the ranges the control platform can handle using LEM LV-50 voltage transducers. Moreover, analog low pass filters are used for elimination of commutation noise in the signals prior sampling. Also, voltage buffers are employed for decoupling the filters and meassuring resistors from the Analog to Digital Converters.

- Loading device. For loading the machine, an electromagnetic break is employed. This device takes a DC current and compacts the magnetic dust inside it, for applying torque to the shaft. The DC voltage supplied is in turn commanded remotely by the control platform, by means of an analog output port.

- Torque meter. The meassurement of the torque will be carried out using a Lorenz DR-2112 torque meter coupled between the motor and the load. The output is an analog signal that can be visualized using the oscilloscope or measured by the control platform using an analog input. The torque and speed meassurements are also depicted in digital displays on top of the test bench.

2.3.2 Frequency and voltage amplitude selection

For determining the limits of operation of the sensorless control developed, experimental tests using different injection voltages and frequencies are carried out. First, the importance of the injected voltage's amplitude is measured by fixing the injection frequency at 1250 Hz and varying the amplitude. The results of this experiment can be observed in Figure 2.27, where the estimated rotor position for the different voltages is shown. The rotor is fixed at a random position, and the response of the proposed sensorless control is plotted. The voltage levels range from the bare minimun that it was found sufficient for the algorithm to work (3 V) up to the 10% of the machine's nominal voltage. It can be observed

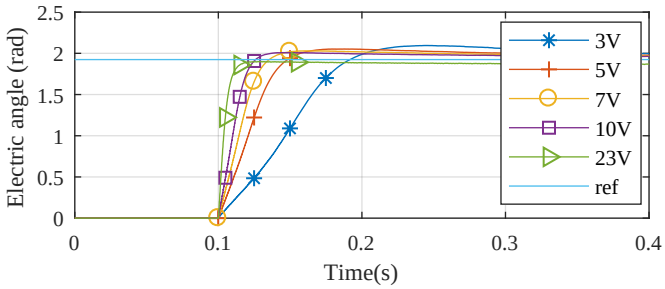

Figure 2.27: Sensorless estimated position speed for different injected voltage amplitude levels

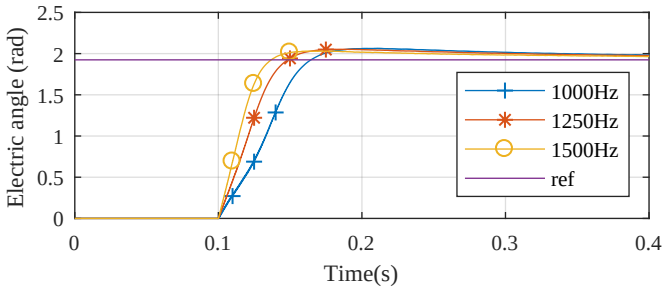

Figure 2.28: Sensorless estimated position speed for different injected voltage frequencies

how the response gets faster as the voltage level gets higher. However, the higher the voltage level, the more noise and vibrations the machine is going to produce. From Figure 2.27 it can be observed how there is approximately the same gain in the sensorless estimation speed from 3 V to 5 V than the one from 5 V to 23 V, so for the next experiments 5 V is going to be selected as the injected voltage's amplitude.

Next, for the selected injection voltage's amplitude, different carrier frequencies will be testes in the same fashion. This is depicted in Figure 2.28, where for the same amplitude of $U_C = 5$ V, the frequency varies along three different possibilities. The frequency used in the last experiment (1250 Hz) is compared

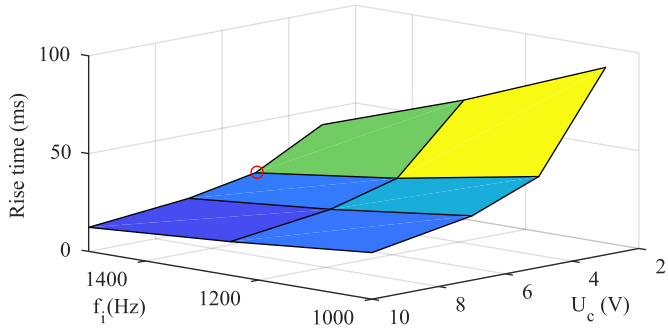

Figure 2.29: Response time of the sensorless angle estimation for different combinations of the injected voltage's amplitude and frequency. Selected combination marked with the red circle

to higher and lower values. Although by looking to the results, choosing higher frequencies seems to be the right choice, the difficulties of rising the injection frequency has already been discussed. For the rest of the experiments, 1500 Hz has found to be the better choice in terms of fast response and feasibility.

The last two experiments can be summarized in Figure 2.29, where the rise time of all the combinations tried are depicted. It can be observed how the difference between the selected option and those with higher values on both voltage amplitude level or frequency is not worth the problems mentioned and guarantees a good system performance.

2.3.3 Comparison of demodulation schemes

In this section, both demodulation schemes presented in Section 2.2.5 are experimentally tested. In addition to the parameters of the motor showed in Table 2.3, the main parameters for the experimental setup are now gathered in Table 2.6. During the experimental tests of this section, the FOC uses the measured rotor angle.

As it was found during the simulation tests, the single demodulation scheme

Parameter	Description	Value
Sampling frequency	10	kHz
Switching frequency	10	kHz
Injection voltage	5	V
Injection frequency	1500	Hz
Analog LPF f_c	3.2	kHz
Estimator LPF f_c	500	Hz
Estimation compensation coefficient k_0	0.0083	-
Estimation compensation coefficient k_1	0.0091	-
DC bus voltage	100	V
PMSM rated power	6700	W
Rated voltage	230	V
Rated speed	3000	rpm

Table 2.6: Parameters of the experimental setup

presents convergence issues that renders it unusable. This can be confirmed in the experiments whose results are depicted in Figure 2.30. In this test, the sensorless alogorithm is turned on for estimation, and then a speed reference of 200 rpm is applied to the rotor, using a ramp. From Figure 2.30 a) and Figure 2.30 b) it can be observed how there is an convergence error from the moment the sensorless is activates. Although from Figure 2.30 c) it can be seen how the speed estimation is correct, the error introduced in the rotor angle would render the system unstable.

The same test is then conducted but using the proposed dual demodulation scheme that uses both components. The results are shown in Figure 2.31. As it can be observed Figure 2.31 a) and b), the convergence error is no longer present. The speed estimation is correct as in the previous case, as Figure 2.31 c) shows.

As it could be observed in Figure 2.31 b), there is still a small error is committed, which is related to the processing delays and phase lags introduced by the filters. If this error is represented against the rotor speed, the results are the ones depicted in Figure 2.32. It is clear that there is a linear dependency between

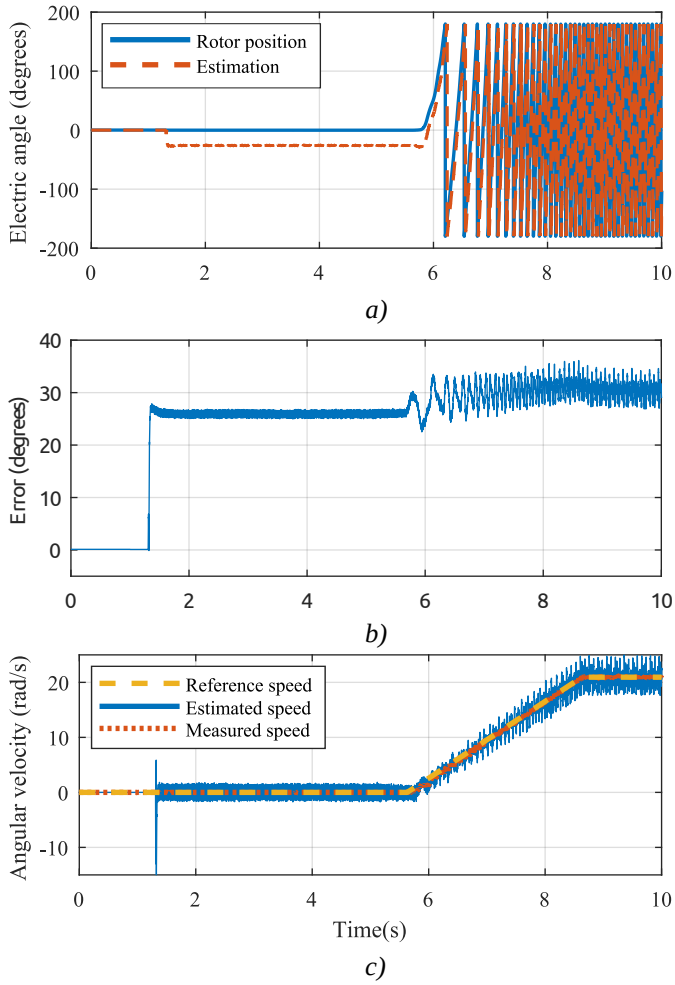

Figure 2.30: Motor start-up while executing the single demodulation scheme. a) Rotor (solid blue) and estimated (dashed orange) angles. b) Error commited in the estimation. c) Reference (dashed yellow), measured (dotted orange) and estimated (solid blue) speeds

the error committed and the rotor speed. This can be explained recalling the explanation of Figure 2.16. The lag introduced by the filters will be dependant on

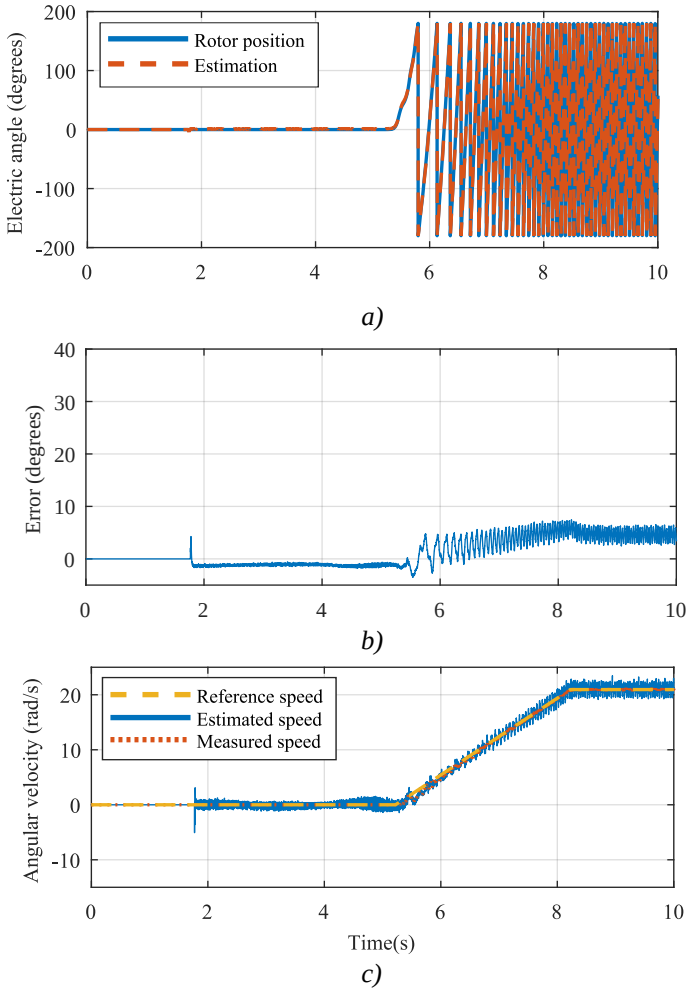

Figure 2.31: Motor start-up while executing the dual demodulation scheme. a) Rotor (solid blue) and estimated (dashed orange) angles. b) Error commited in the estimation. c) Reference (dashed yellow), measured (dotted orange) and estimated (solid blue) speeds

the speed and thus, the error in the estimation. The rotor estimated position can be adjusted taking into account this fact in the following manner

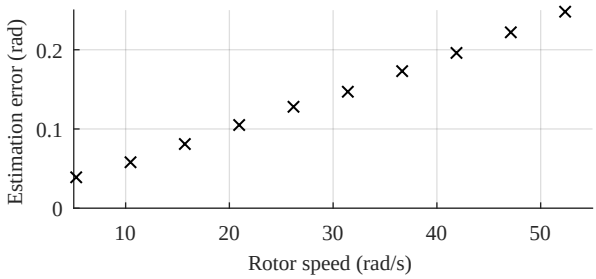

Figure 2.32: Lineal relationship between speed and error

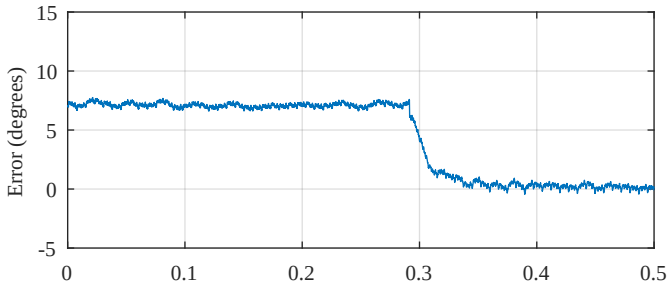

Figure 2.33: Estimated rotor position correction. The rotor is spinning at 200 rpm, correction applied at $t \approx 0.3$ s

$$\theta'_{sl} = \theta_{sl} + e(\omega) \approx k_1 \omega_{ref} + k_2, \tag{2.47}$$

where ω_{ref} is the reference speed and k_1, k_2 are the linear regression coefficients. The reson of using the reference speed instead the actual estimated speed is to avoid including another algebraic loop in the estimation algorithm. Figure 2.33 shows the estimated position when the rotor is spinning at a speed of 200 rpm, before and after of applying the correction explained.

2.3.4 Sensorless control of the machine

For the remaining experimental tests, the estimated position θ_{sl} will be the one used for the FOC. The meassured position will only be used for monitoring pur-

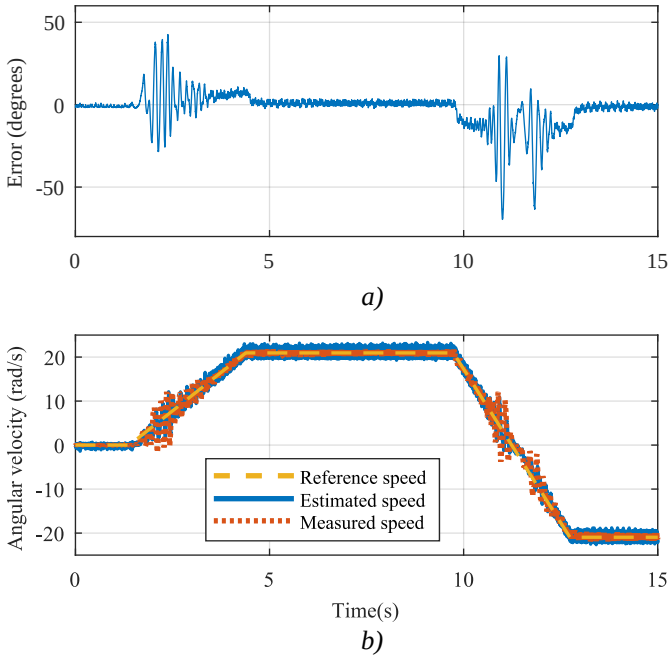

Figure 2.34: Start-up of the motor and zero crossing experiment. a) Error commited in the angle estimation. b) Reference (dashed yellow), estimated (solid blue) and measured (dotted orange) speeds

poses, so the machine will operate in full sensorless mode. The compensation described in (2.47) is applied for all cases. For all the experiments, the start up procedure includes the following

1. A constant and positive voltage is applied to the d-axis using a fixed angle of 0. This ensures that the d-axis is aligned with the rotor axis.

2. Any difference between the angle meassured from the resolver and the reference of 0 is cancelled as offset.

3. The high frequency injection is turned on and the estimated angle is the one used for the FOC. The rotor is kept still by setting the speed reference

to 0.

4. The machine is started by setting a reference speed.

The first test consists on the motor start up from still up to a reference speed of 200 rpm. This speed is maintained for some seconds and then a reference speed of -200 rpm is given to the motor. This will check the system behaviour when the rotor crosses the 0 speed reference. The results are shown in Figure 2.34. From Figure 2.34 a) it can be seen how even if there are oscillations when the speed is close to 0, the system is able to operate successfully. It is important to note that the injection is kept as low as possible in order to minimize noise and vibrations in the system. Higher voltages could render better results, at the expense of these risks. Figure 2.34 b) depicts the correct estimation and operation of the system speed.

The next experiment will test the ability of the control to withstand loading of the machine. While running at a speed of 200 rpm, a 10 Nm load will be applied using the electromagnetic brake. It is maintained during some seconds and then it will be realeased. The results of the experiment are shown in Figure 2.35. The figure represents the current demanded by the machine in the q-axis, i.e., the one producing the torque. The current rises from nearly zero, when the machine has no torque applied, to 14 A, as it can be seen in Figure 2.35 a). From Figure 2.35 b) one can see how the loading affects to the speed of the motor, which recovers the value set as reference quickly.

The last experiments conducted are related to the start-up of the motor to different very low reference speeds, with and without load. In the tests made until now, the reference speed has always been set to 200 rpm. For these ones, the references will be lowered to 150, 100 and 50 rpm, the last one being below the 2 % of the machine's nominal speed. The results of the start up experiments with no load are shown in Figure 2.36. The references are given in rpm, but

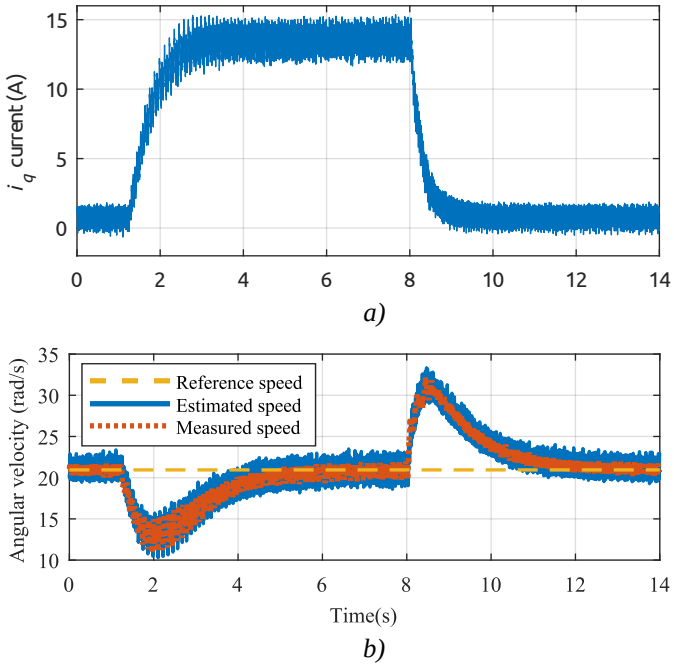

Figure 2.35: Loading experiment

all the signals shown are expressed in rad/s. From the image one can see how the motor is able to start for all the references set, including the lowest one. It is interesting to note how for higher speed references, the estimated speed ω_{sl} as higer high frequency ripple, and yet the measured speed of the rotor as almost no ripple. This is due to the speed controller bandwidth, that is chosen so it neglects this high frequency noise. Nevertheless, when the reference is low enough, although the high frequency noise in ω_{sl} is lower, there are also lower frequency components that are transferred to the speed controller and they show in the measured speed.

The same start-up experiment is now repeated, but loading the motor from the start, with the same loading conditions as in Figure 2.35. The results are

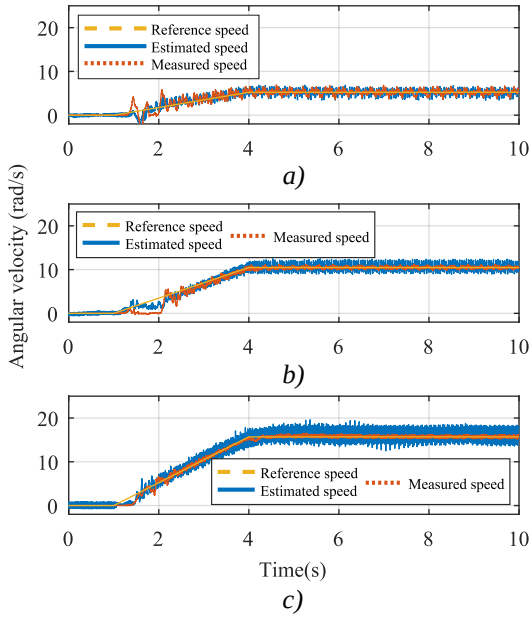

Figure 2.36: Start-up of the motor for different speeds with no load. Reference (dashed yellow), estimated (solid blue) and measured (dotted orange) speeds. a) 50 rpm. b) 100 rpm. c) 150 rpm

gathered in Figure 2.37. The behaviour of the system is similar to the one described in the previous experiment. The loading impacts heavily in the low frequency noise, specially in the case of the lowest speed reference. This is due to the non linearities of the power electronics, that deforms the injected voltage and thus, affects negatively the sensorless performance. This non linearities are more severe when loading and are subject of study by many researches. However, it is out of the scope of this work.

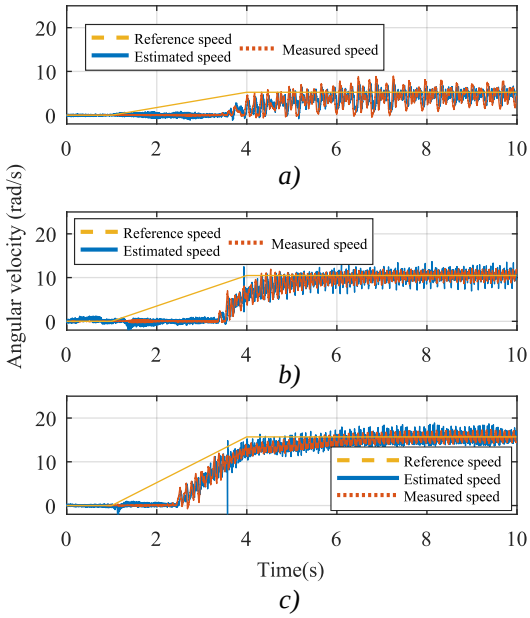

Figure 2.37: Start-up of the motor for different speeds with 10 Nm load. Reference (dashed yellow), estimated (solid blue) and measured (dotted orange) speeds. a) 50 rpm. b) 100 rpm. c) 150 rpm

2.4 Conclussions

The sensorless control for a SMPMSM has been studied and improved by proposing a new enhanced demodulation scheme, able to operate with a very low injection. The following conclussions can be drawn from this work:

1. Sensorless control of the PMSM is still a very difficult task, specially for the case considered of a SMPMSM. The low saliency ratio make it hard to track the rotor position due to the low anisotropy. Still, the enhanced demodulation technique proposed performs correctly including in the low speed region.

2. The injected voltage plays a key role in the estimation performance of the

demodulation process. With the proposed technique, a 5 V injection was found enough to control de machine successfully. This represents only a 2.17 % of the rated voltage of the machines. Higher results could render better results, but at the expense of higher noise and losses.

3. The injection frequency is another important variable to consider. It is desirable to raise it as much as possible, but by doing so, the carrier current recovered will become smaller in amplitude. Therefore, it will become more sensitive to noise.

4. The sampling frequency needs also to be taken into account since it will determine how high the injection frequency can be. In order to allow a good signal recovery, it should be several times higher than the injection frequency. Given that the sensorless technique used employs a sinusoidal carrier, for this work the best results for a sampling frequency $T_s = 10^{-4}$ s were obtained for an injection frequency of 1500 Hz.

3

Vehicle to Grid operation

3.1 Introduction

The rise in the electric energy demand is expected to be covered by distributed generation based on renewable energies. The downside of the renewable generation is the need of energy storage, but thanks to the great advance in Energy Storage System (ESS), that future is closer day by day. This is going to be the beginning of the Smart Communities [51, 52].

The benefits coming from distributed generation and energy storing apply to both consumers and producers. On the one hand, the consumers could obtain benefits in terms of savings in their electric bills [53], given that the energy consumed could be provided closeby, in distributed generators of the community. This energy supply could be direct, if the demand matches the generation time, or indirect, by means of ESS, with proper management.

On the other hand, the owners of the distributed energy resources will also benefit from this trend. Generally speaking, the distributed generation based in photovoltaic panels or wind generation located near consumers is non-manageable [54]. This means that the energy is only available the moment is being generated.

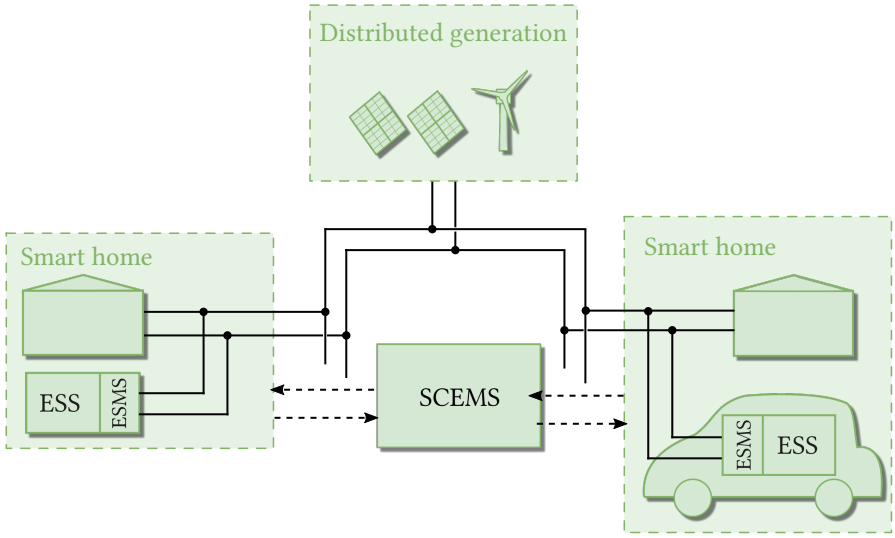

Figure 3.1: Diagram of a smart community, showing smart homes coordinated by the SCEMS

However, coordinating with local consumers and ESS allow the owners to sell or accumulate the energy locally. Later, the exceeding energy could be sold to the market during high-price time periods, independently of the generation timetable [55]. Moreover, the management of the renewable energy injection to the grid is always a great advantage for the distribution grid operation [56, 57], which is a benefit for everyone.

It is clear that ESS are a vital aspect of the energy management system of the smart community [58, 59]. Most of the research focuses on the high capacity (10-100 MWh) storage systems [60]. Nevertheless, micro-storage systems located at home are receiving wide attention nowadays, with a capacity of few kWh [61]. These micro-storage systems provide a more flexible solution for smart communities, allowing the consumers to store a small amount of energy locally. This will allow them to provide for demand peaks, relieving the community of

the intermittency and variability of renewable energy generation. The control of such storage systems is done by a central Smart Community Energy Management System (SCEMS). Its role is to act as a aggregator of resources, coordinating them to provide users the benefits aforementioned. The diagram of a smart community such as the one described can be seen in Figure 3.1. From the diagram, it is clear that the local ESS can be stationary storage systems located in each home, or non stationary storage systems, such as the batteries used in EVs.

3.1.1 Grid functions of the ESMS

Among other functions, the SCEMS is responsible for generating set-points of both active and reactive power and sending them to each local ESS for charging/discharging, based on the expected demand and production.

Although the penetration of smart communities and ESS in desirable, most battery chargers on the market demand harmonic currents and reactive power [62] that would cause a great impact in the power quality of the distribution system [63, 64]. Thus, there is a need for research in new control strategies applicable to the Energy Storage Management System (ESMS) that allow these chargers to operate within the smart grid goals [65].

Besides fulfilling the power requirements from the SCEMS, the power converter used for the ESS charger can be used to provide further active functions to the grid, such as active power filtering [66, 67]. If each ESS in the smart community provides the harmonic current demanded by the home it is placed in, a global improvement of power quality can be achieved.

3.1.2 EV chargers integration

The EV is gaining popularity due to environmental concerns and motivates research related to it. Special interest is put into the charging process, since the energy stored in the EV battery can also be used for grid services [68], behaving

as ESS available to the Smart Community, as shown in Figure 3.1. The charger topologies also receives a fair amount of attention, since it is desirable to charge the EV with the higher efficiency and as fast as possible [69].

According to the charging power level, chargers can be roughly classiffied into Level 1 (up to 1.92 kW), Level 2 (up to 19.2 kW) and Level 3 (from 20 kW onwards) [70, 71]. The higher the charging power, the more complex the charger will be, needing more components or bigger ones. Therefore, Level 3 chargers are located off-board while the other two are usually located on-board. Although three phase connections to the grid allows faster charging, single phase outlets are still the main source of energy available to EV owners [72].

Due to the fact that the propulsion and charging systems share quite a few elements, there is a trend of integrating the charging system into the power electronics already present for driving the motor [73–75]. In this case, the onboard charger becomes an Integrated Onboard Charger (IOC). The propulsion inverter can be easily adapted for the charging process, and the motor windings could be employed as inductive filters.

Some authors propose to use additional rectifiers for the AC/DC conversion from the grid, then the machine windings are used as inductors for a DC/DC converter [76–78]. The main drawback is the need of additional components that will translate into an increment of the cost, losses, volume and weight. In other cases, as in this work, the machine windings is used as a grid filter connected between the grid and the converter, which is used later on for AC/DC conversion [79–83]. The principal disadvantage is the generation of a charging torque in the shaft due to the grid currents flowing through the machine.

3.1.3 Challenges encountered

The majority of bidirectional chargers that are addressed in the literature target the active power flow control [84] and only a few focus their efforts in reactive

power flow control [85, 86]. Nevertheless, the benefits of developing a local strategy for harmonic compensation within the homes fo the smart community have not been yet throughly investigated.

When integrating the machine with the charger, the cancellation of the torque generated has been receiving quite a lot of attention lately. The solutions proposed include using several machines [81], custom windings [79] and multiphase machines [77, 80, 87]. These innovative solutions require said special components that are still not present in the wide majority of EV systems. Moreover, the torque cancellation strategy in single phase chargers normally assumes that the phase connected to the grid is aligned with rotor d-axis, where no torque is produced [75, 77, 87]. This causes a lack of generality, since it is vital to have an optimized control strategy that guarantees the absence of vibrations in the system.

3.1.4 Goals of the research

The work developed in this charger has two main objectives in mind. On the one hand, it will try to provide the ESMS of an ESS with control strategies to fulfill the active and reactive power requierements set by the SCEMS. A control strategy for compensating harmonic currents will be developed to operate simultaneously with the power control ones. The three strategies will be tested in simulation and experiments. Moreover, the inclussion of hybridation in the ESS will be put to the test.

On the other hand, the integration of the charger developed with the drive system of an EV will be studied, and the problems that arise will be analized. The development of control strategies for solving the integration issues will be tested with simulations and experiments.

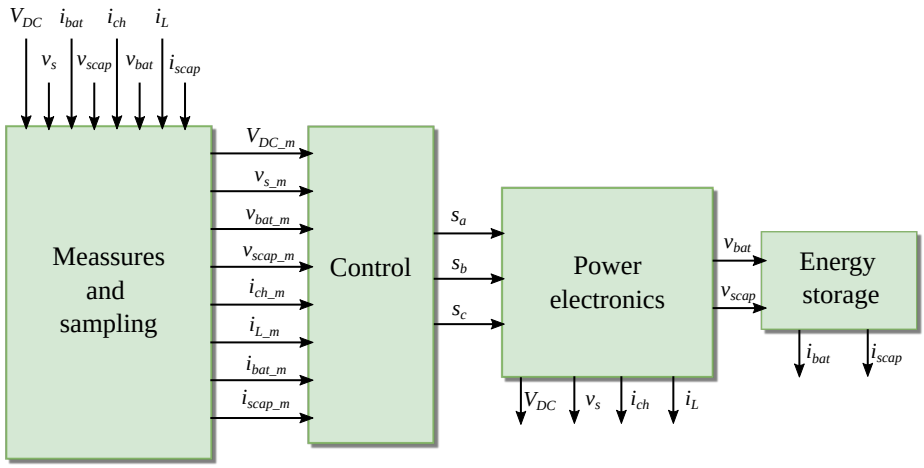

Figure 3.2: General scheme of the model employed for simulation

3.2 Charger description and modelling

As it was done in the previous chapter, the modelling and simulation of the charging system has been donde in MATLAB Simulink. Thus, it shares most of the elements defined in Section 2.2, although some of them are modelled differently. The whole system model is depicted in Figure 3.2. It breaks down to the following components:

- Measures and sampling. This part of the model is based in zero-order hold downsampling the main system variables.
- Control. This model takes the measures and compute the current references and required signals for the power electronics.
- Power electronics. This part of the system takes the control signals from the current controller and forms the voltages needed for the battery and supercapacitor.

Parameter	Description	Value
R_{AC}	AC inductive filter resistance	1×10^{-3} Ω
L_{AC}	AC inductive filter inductance	30×10^{-3} H
R_{bat}	Battery inductive filter resistance	1×10^{-3} Ω
L_{bat}	Battery inductive filter inductance	15.6×10^{-3} H
R_{scap}	Supercapacitor inductive filter resistance	2×10^{-3} Ω
L_{scap}	Supercapacitor inductive filter inductance	10×10^{-3} H

Table 3.1: Parameters of the inductive filters of the converter

- Energy storage. This is the part of modelling the energy reservoir to operate with, including the battery and the supercapacitor.

The inputs for the system are the DC bus, grid, supercapacitor and battery voltages ($V_{DC}, v_s, v_{scap}, v_{bat}$ respectively), as well as the charger, load, supercapacitor and battery currents ($i_{ch}, i_L, i_{scap}, i_{bat}$ respectively). The control model outputs will be the switching signals s_a, s_b, s_c needed for the power electronics model. Its outputs, the battery and supercapacitor voltages will be used by the energy storage models.

Similarly to the model made in the previous chapter, the inputs and outputs are selected to guarantee a smooth transitions to the experiments. Moreover, it allows having different time steps for the control model, and power electronics and energy storage models. This ensure a more realistic scenario.

The measures and sampling model is identical to the one described in Section 2.2.4, only varying in the number of inputs and outputs. Moreover, since a single-phase charger is used, there is only need for measuring one current. Thus, there is no need for using (2.26). This section will describe the remaining parts of the system model.

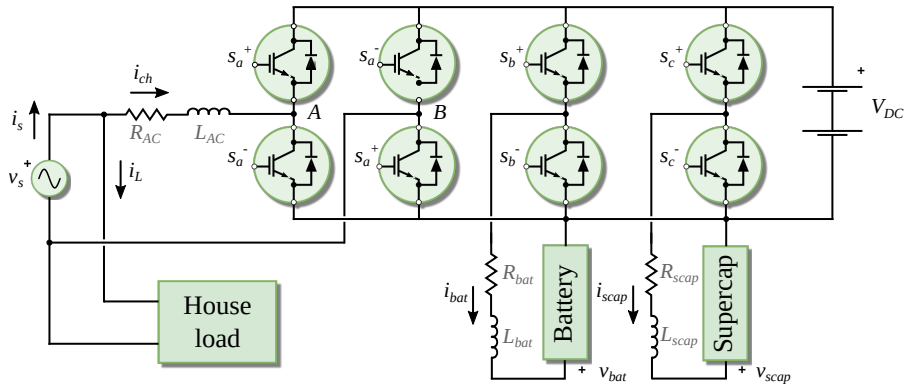

Figure 3.3: Power electronics and energy storage simulation models

Description	Value
IGBT internal resistance	1×10^{-3} Ω
IGBT snubber resistance	1×10^{-3} Ω
IGBT snubber capacitance	∞ F
Battery nominal voltage	48 V
Battery rated capacity	45 Ah
Battery initial SOC	40%
Supercapacitor rated capacitance	99.5 F
Supercapacitor rated voltage	48 V
Supercapacitor initial voltage	18 V
Supercapacitor equivalent DC series resistance	8.9×10^{-3} Ω

Table 3.2: Parameters of the power electronics and energy storage

3.2.1 Power electronics and energy storage modelling

The power electronics and energy storage models represent the charger topology under study, and it is depicted in Figure 3.3. It is composed of a two branch inverter for the connection to the AC grid, and a DC/DC converter for each ESS, all sharing the same DC bus. Each branch is formed by two IGBT switches, each one with a reverse diode. They take the switching signals from the control

model and outputs all the voltages and currents measured. Unlike it was done in Section 2.2.2, in order to speed up this simulations, the power electronics and energy storage system is modelled using Simulink powerlib library, and their main parameters are shown in Table 3.2. The parameters for the inductive filters are gathered in Table 3.1. The voltage v_s is modeled as a programmable voltage source with harmonic content as

$$v_s = \sqrt{2}V_{1s}\cos(2\pi 50) + \sqrt{2}\sum_{h>2} V_{hs}\cos(h\cdot 2\pi 50 + \phi_{hs}), \tag{3.1}$$

where h is the order of the harmonic, V_{hs} is the RMS value of the h order harmonic and $\phi_h s$ is the phase angle of said harmonic wave. similarly, the current i_L is modelled as a corrent source as

$$i_L = \sqrt{2}I_{1L}\cos(2\pi 50) + \sqrt{2}\sum_{h>2} I_{hL}\cos(h\cdot 2\pi 50 + \phi_{hL}), \tag{3.2}$$

being I_{hL} the RMS value of the order h harmonic and ϕ_{hL} its phase angle. The currents in the system follow the relationship

$$i_s = i_{ch} + i_L \tag{3.3}$$

where i_s is the current demanded from the grid and i_{ch} is the current provided by the charger.

3.2.2 Control modelling

The control model uses the measured variables for generating currents references. This references will be translated to duty cycles and switching signals that the charger's power electronics will use to ensure that the system currents follow the aforementioned references. The overall control model is depicted in Figure 3.4, where two submodels are seen. The current controller submodel generate the current references taking into account different parameters and the control strategies used. The current references are then used by the PWM submodel for generating the duty cycles and the switching signals.

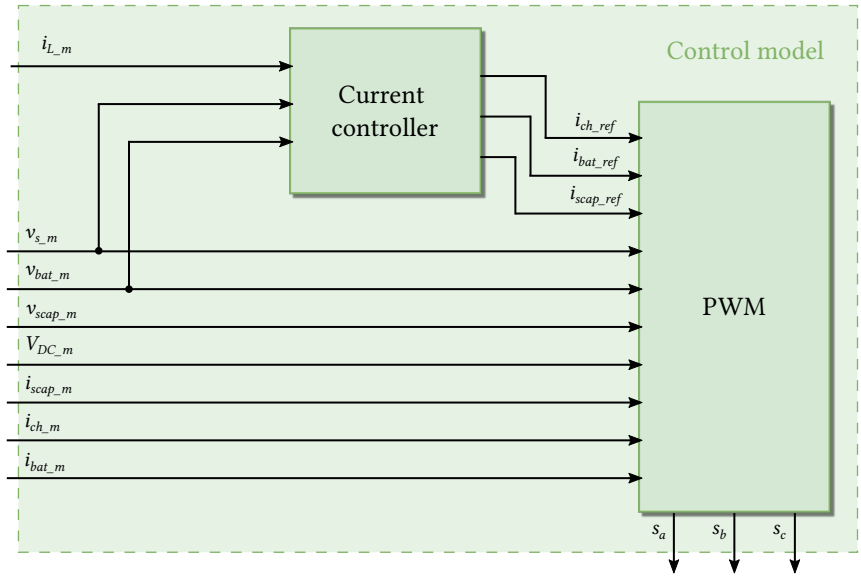

Figure 3.4: Control model including the current controller and the PWM sub-models

3.2.2.1 Current controller

The current controller simulation model implements all the control strategies adopted in the charger in order to produce the adequate references. The general scheme of such controller is depicted in Figure 3.5.

In order to be able to generate active and reactive power, detecting the phase voltage is needed. This is achieved by using a Single-phase Phase-Locked Loop (PLL). The diagram for this model can be observed in Figure 3.6. The goal of this subsystem is to generate two unitary signals: one in phase with the fundamental grid voltage v_0 and other displaced 90 degrees, v_{90}. To this aim, it forms a vector in the *abc* reference frame, although there is only phase a since it is a single phase system [88]. This vector is then transferred to the *dq* reference frame. In order to align the d-axis with phase a, the q-axis fundamental component v_{1q} must be

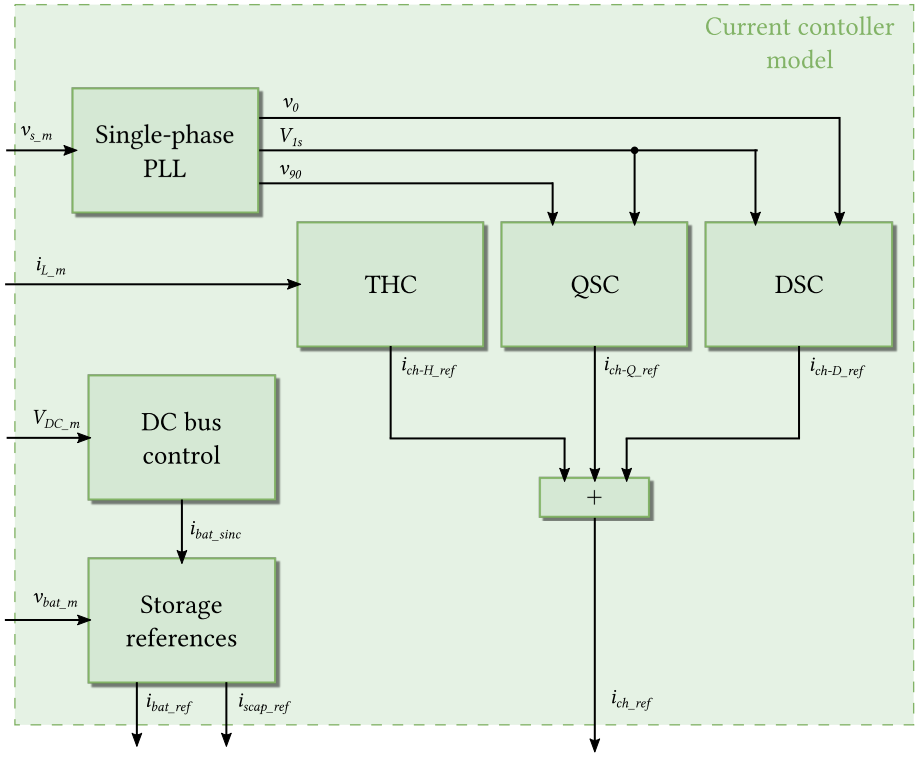

Figure 3.5: Current controller simulation model employed

0. Thus, the q-axis component is fed to a PI controller, whose output will be added with an initial constant $\omega_0 = 2\pi 50$, since the grid frequency is 50 Hz. The result is integrated and the voltage phase angle is obtained. The unitary signals are computed by applying the sine and cosine functions to this angle.

If the grid voltage has harmonics components, when the voltage vector is transferred to the dq frame, there will be oscillations. Since the the reference system is rotating at the same frequency as the voltage vector, the fundamental components u_{1d} and u_{1q} will be constant values. Therefore, the dq components obtained using the dq0 transformation are filtered to retain only the fundamental

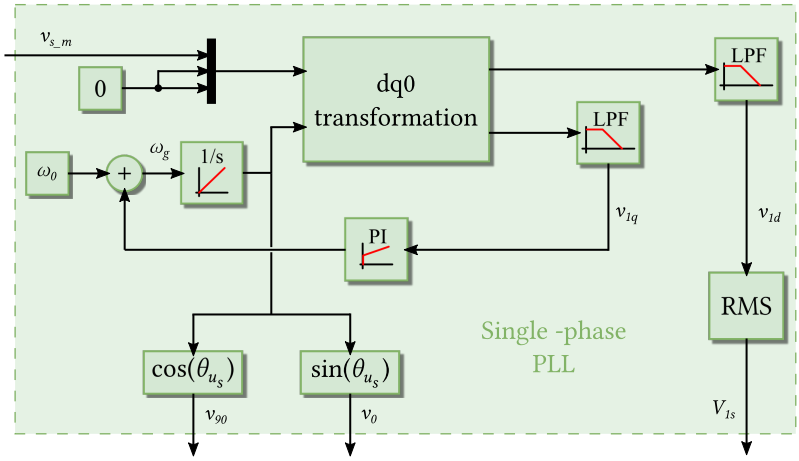

Figure 3.6: Single-phase PLL simulation model.

components. Moreover, the RMS value of the voltage V_{1s} refers to the RMS value of only the fundamental component of the grid voltage.

The functioning of the single-phase PLL described can be observed in the Figure 3.7. The simulated grid voltage v_{s_m} can be seen in Figure 3.7 a), and has a fundamental component $V_{1s} = 230$ V. Moreover, it has 3rd, 5th and 7th harmonic components whose RMS values relative to the fundamental component are equal to 5%, 4.5% and 4%, respectively. The extracted fundamental component v_{1s} is depicted in Figure 3.7 b), while the unitary signals v_0, v_{90} computed using the found phase angle are showed in Figure 3.7 c).

The converter is connected to an AC power supply (the grid) and a DC power supply (batteries and supercapacitor). Thus, it needs to generate current references for both sides. From the grid side, the current reference is made up of three terms coming from each control strategy: Direct Sinusoidal Current (DSC), Quadrature Sinusoidal Current (QSC) and Total Harmonic Compensation (THC). As it can be deduced from Figure 3.5, the global current reference current

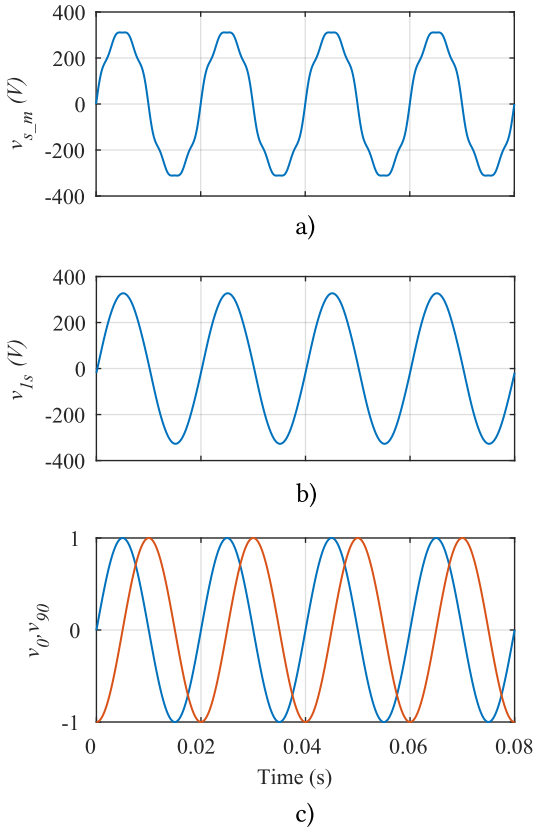

Figure 3.7: PLL simulation results. a) Grid voltage v_{s_m}. b) Fundamental component of the grid voltage V_{1s}. c) Unitary signals v_0, v_{90}.

for the grid connected side of the charger can be expressed as

$$i_{ch\_ref} = i_{ch-D\_ref} + i_{ch-Q\_ref} + i_{ch-H\_ref}, \tag{3.4}$$

where $i_{ch-D_r ef}, i_{ch-Q_r ef}, i_{ch-H_r ef}$ are the references from the DSC, QHC and THC control strategies respectively. Each one of the references is responsible of one property of the charger. The DSC is in charge of the active power and is

calculated as

$$i_{ch-D\_ref} = \frac{P_{ref}}{V_{1s}}\sqrt{2}v_0, \tag{3.5}$$

where P_{ref} is the active power reference set, and its sign will be the one deciding the direction of the energy flow. Dividing the power reference by the RMS value of the voltage's fundamental component gives the current RMS value that will provide the power needed. Multiplying by the unitary signal v_0 ensures that the reference current is in phase with the grid voltage. In a similar fashion, the QSC is in charge of the reactive power and its reference is described by

$$i_{ch-Q\_ref} = \frac{Q_{ref}}{V_{1s}}\sqrt{2}v_{90}, \tag{3.6}$$

being Q_{ref} the reactive power reference setpoint. Again, the sign of this reference determines the direction of the energy flow, and multiplying by v_{90} ensures that this current only provides reactive energy. This is due to the 90 degrees displacement between this signal and the grid voltage.

The last component of the reference current is the one from the THC control. Its goal is to compensate the harmonics of the load current i_L. To prevent overload of the charger, the maximum RMS current available as a function of the DSC and QSC currents is calculated as

$$I_{ch-H\_max} = \sqrt{I_{ch-n}^2 + I_{ch-P}^2 + I_{ch-Q}^2}, \tag{3.7}$$

where I_{ch-n} is the nominal RMS current of the charger and I_{ch-P}, I_{ch-q} are the RMS values of the reference currents from DSC and QSC control strategies. They are the results of the quotients in (3.5) and (3.6). Taking into account this limit, the THC current reference can be expressed as

$$i_{ch-H\_ref} = \begin{cases} -\left(i_L - i_{1L}\right) & \text{RMS}\left(i_L - i_{1L}\right) \leq I_{ch-H\_max} \\ -\left(i_L - i_{1L}\right) \cdot K & otherwise, \end{cases} \tag{3.8}$$

in which i_{1L} is the fundamental component of the load current, extracted using a single-phase PLL like the one in Figure 3.6, and K is a scaling factor defined as

$$K = \frac{I_{ch-H\_max}}{\mathrm{RMS}\left(i_L - i_{1L}\right)}. \tag{3.9}$$

Figure 3.8 depicts an example of the reference currents provided by the current controller described. i_{ch-D_ref} and i_{ch-Q_ref} currents from the DSC and QSC control strategies are shown in Figure 3.8 a), where it can be seen that there is a 90 degrees phase shift between the two. They are based on the signals from Figure 3.7 c), so they will only provide active and reactive power, respectively. Figure 3.8 b) presents an example of load current, with a rich harmonic content. The fundamental component is extracted and used to generate the i_{ch-H_ref} current as in (3.8) (no scaling is needed in this example). Lastly, the final i_{ch_ref} current is shown in Figure 3.8 c).

Moving on to the DC side, there are two power supplies: the battery and the supercapacitors. They are in charge of providing the energy needed to maintain charged the DC bus as well as the power required. The controller for the DC/DC converters have two main components: one in charge of maintaining the DC bus voltage equal to the reference; the other one takes care of the active power reference P_{ref}.

The DC bus control ensures that $V_{DC\_m} = V_{DC\_ref}$ using a PI controller. Thus, one can write

$$\begin{aligned} I_{bat\_sinc}(s) &= \left(K_{p\_i_{sinc}} + K_{i\_i_{sinc}} \frac{1}{s}\right) E_{i_{sinc}}(s) \\ E_{i_{sinc}}(s) &= V_{DC\_ref}(s) - V_{DC\_m}(s) \end{aligned} \tag{3.10}$$

where I_{bat_sinc} is the current needed for charging the DC bus at the required voltage, in the Laplace domain. As it was explained in Section 2.2.3.1, MATLAB takes care of the transformation of time signals to Laplace in order to use transfer functions. It will be delivered by the battery.

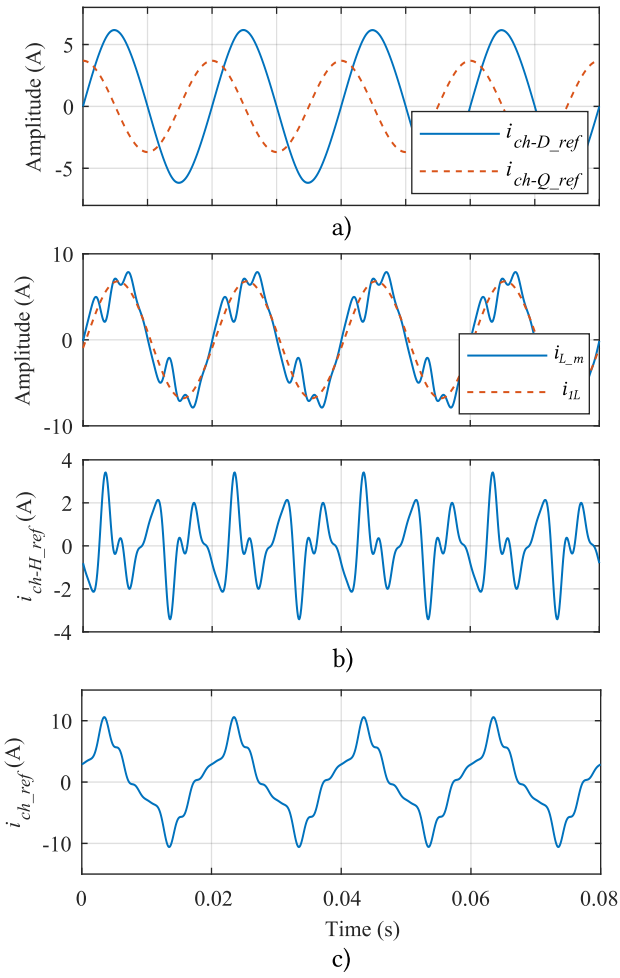

Figure 3.8: Reference currents given by the current controller. a) Reference currents from DSC (solid blue) and QSC (dashed orange) control. b) Load current (solid blue) and its fundamental component (dashed orange) at the top, THC reference current at the bottom. c) Reference current for the charger

The second component of the DC/DC controller is in charge of delivering the active power required by the SCEMS. The battery is again the one supplying the energy required, so the current needed will be P_{ref}/v_{bat_m}. However, since

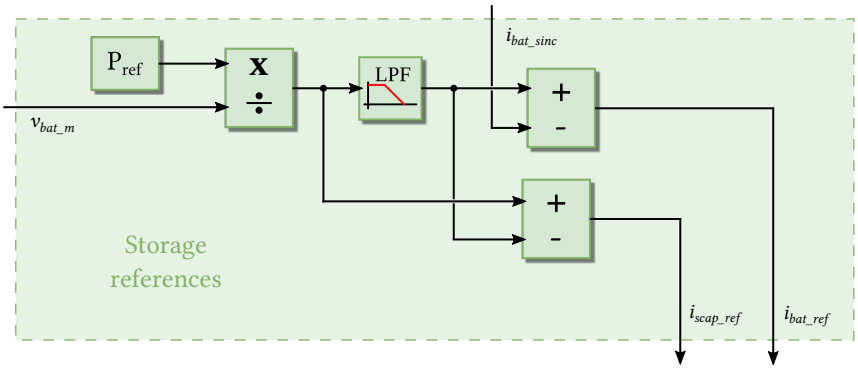

Figure 3.9: DC reference currents for the storage system

the battery mechanics is relatively slow and it is desirable to expand its lifetime as much as possible, the supercapacitor will provide the transient demands of energy. This is depicted in Figure 3.9, where the control logic for computing the DC storage currents can be observed. This current is dividided into two terms for each element following

$$\begin{aligned} i_{bat\_ref} &= \text{LPF}\left(\frac{P_{ref}}{v_{bat\_m}}\right) - i_{bat\_sinc} \\ i_{scap\_ref} &= \frac{P_{ref}}{v_{bat\_m}} - \text{LPF}\left(\frac{P_{ref}}{v_{bat\_m}}\right). \end{aligned} \tag{3.11}$$

Figure 3.10 shows the reference current generated for the DC side of the converter. A reference setpoint of 600 V is given for the DC bus, and at $t = 0.2$ s, an active power reference $P_{ref} = 400$ W is set. Figure 3.10 a) shows the reference voltage for the DC bus and the measured on. The charging of the DC bus is made by the battery, as it was stated in (3.11), and this can be seen in Figure 3.10 c). When the active power reference is applied, the current neded is provided first by the supercapacitor as it is observed in Figure 3.10 b), and later on by the battery.

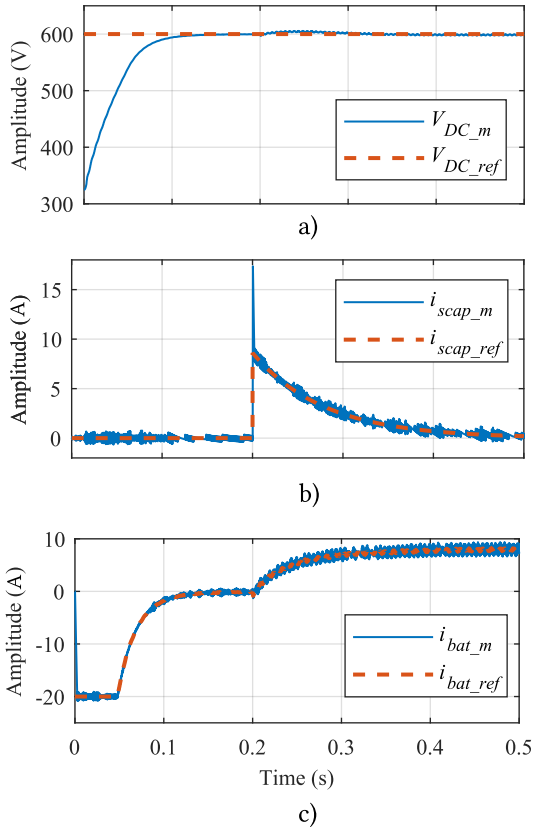

Figure 3.10: Simulation example of the generation of current references for the DC side. a) DC bus voltage, measured (solid blue) and reference (dashed orange). b) Supercapacitor reference (dashed orange) and measured (solid blue) currents. c) Battery reference (dashed orange) and measured (solid blue) currents

3.2.2.2 Pulse Width Modulation

The PWM simulation model is similar to the one depicted in Figure 2.10, except for the duty cycle computation part. Instead of using PI controllers for tracking the current references, deadbeat controllers are employed. The modificated scheme is shown in Figure 3.11. It takes the measured variables and current

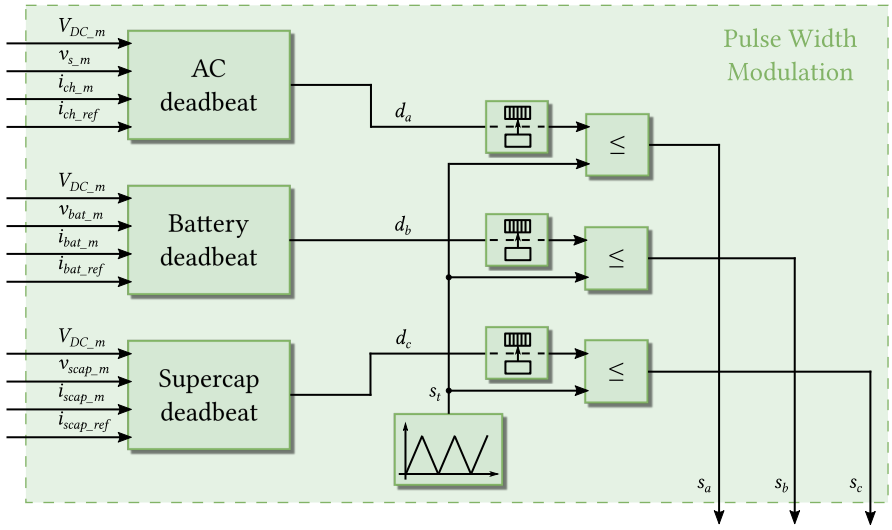

Figure 3.11: Duty cycle computation and PWM simulation scheme

references as inputs and outputs the switching signals for the power electronics model.

The deadbeat is in charge of computing the duty cycles for generating the switching signals for the IGBTs. The converter uses a bipolar PWM, so the same switching signal is applied to the top IGBT of the first branch and to the bottom one of the second (Figure 3.3). The same applies to the complementary switches of the mentioned branches. It uses the difference between the reference and measured current, as well as some other system parameters, to compute it. The process is based on the calculation of the voltage in the inductor, and Figure 3.12 depicts an example for the AC deadbeat. The duty cycle can be expressed as a function of the switching time T_c as

$$d_{AC} = \frac{T_{on}}{T_c} = \frac{(1 - T_{off})}{T_c}, \tag{3.12}$$

where T_{on}, T_{off} are the amounts of time that the IGBT is turned on and off

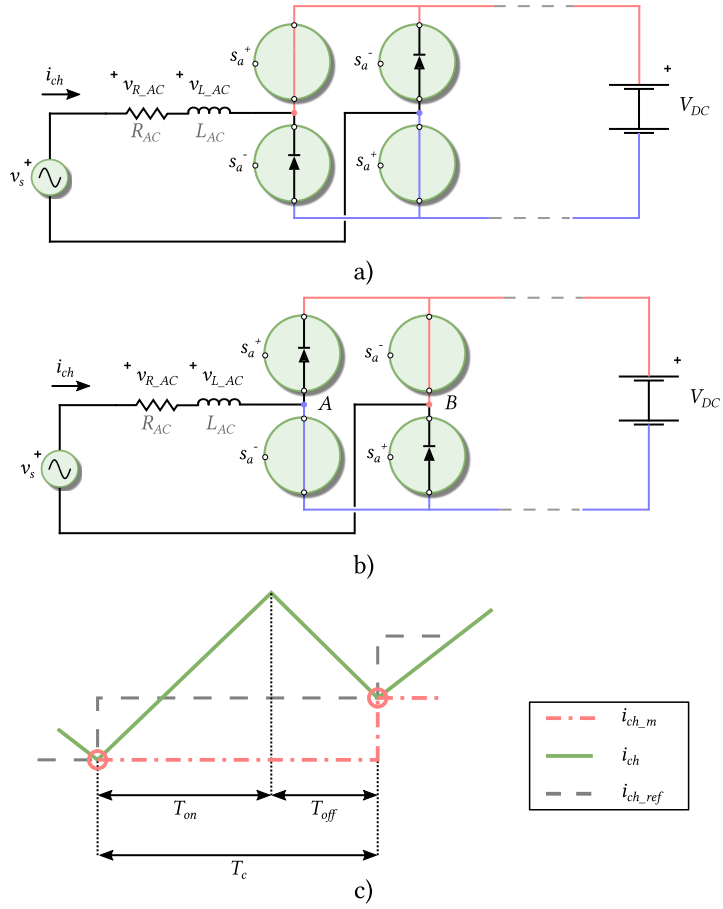

Figure 3.12: Duty cycle computation using the deadbeat current controller. a) Circuit of the converter when $s_a^+ = 1, s_a^- = 0$. b) Circuit of the converter when $s_a^+ = 0, s_a^- = 1$. c) Diagram of the measured (dashed-point red line), reference (dashed grey) and real (solid green) current flowing through the inductor.

respectively. During T_{on}, $s_a^+ = 1$ and $s_a^- = 0$. Given that the PWM uses a bipolar strategy as explained before, the circuit for the converter if only the two branches used for the AC side are represented along the DC bus, is the one depicted in Figure 3.12 a). From this circuit, it can be observed that the voltage

across points A and B is V_{DC}. Similarly, during T_{off}, the circuit is represented in Figure 3.12 b), and the voltage $V_{AB} = -V_{DC}$. Therefore, the voltage across the inductor as a function of the switching state will be

$$v_{L\_AC} = \begin{cases} v_s - v_{R\_AC} - V_{DC} & t \in T_{on} \\ v_s - v_{R\_AC} + V_{DC} & t \in T_{off}, \end{cases} \tag{3.13}$$

where v_{R_AC} is the voltage drop for the resistive part of the AC filter. Since the period of the grid voltage is way higher than the commutation period or switching time T_C, the grid voltage may be regarded constant along one commutation period. The current flowing through the inductor can be approximated by

$$v_{L\_AC} = L_{AC} \frac{\Delta i_{ch}}{T_c}, \tag{3.14}$$

The idea behind the deadbeat control is trying to cancel the error between the reference and measured current in one commutation period. Therefore, the increment of current in the inductor is defined as

$$\Delta i_{ch} = i_{ch\_ref} - i_{ch\_m}. \tag{3.15}$$

Thus, one can calculate the duty cycle needed to cancel the difference between both currents, as seen in Figure 3.12 c). Taking into account that $T_c = T_{on} + T_{off}$ and using (3.12), (3.13), (3.14) and (3.15) one can write

$$\begin{aligned} i_{ch\_ref} - i_{ch\_m} = & \frac{(v_s - v_{R\_AC} - V_{DC})\, d_{AC} T_c}{L_{AC}} \\ & + \frac{(v_s - v_{R\_AC} + V_{DC})\,(1 - d_{AC})\, T_c}{L_{AC}}. \end{aligned} \tag{3.16}$$

Solving (3.16) for d_{AC} yields

$$d_{AC} = \frac{(v_s + V_{DC} - v_{R\_AC})\, T_c - L_{AC}\,(i_{ch\_ref} - i_{ch\_m})}{2 V_{DC} T_c}. \tag{3.17}$$

A similar scenario is found for the deadbeat controllers of the DC side of the converter. The circuit diagrams as a function of the switching state of the branch

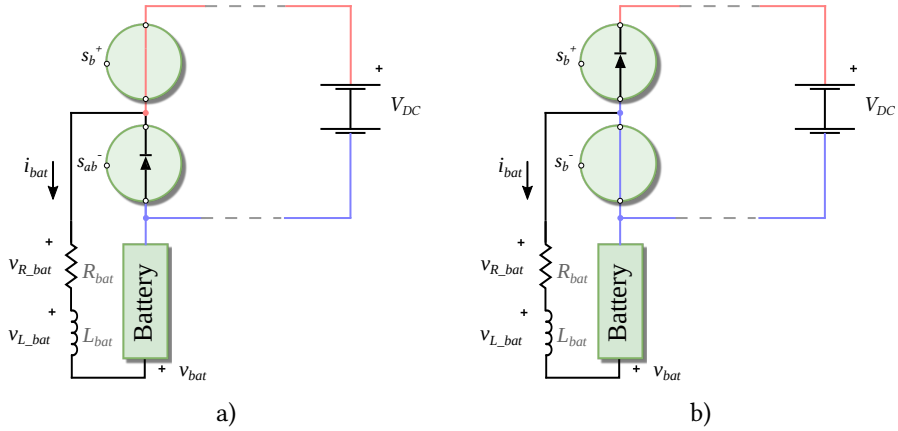

Figure 3.13: Circuit of the converter for the DC storage models according to switching states. a) Circuit of the converter when $s_b^+ = 1, s_b^- = 0$. b) Circuit of the converter when $s_b^+ = 1, s_b^- = 0$.

for the battery is depicted in Figure 3.13. In this case, the voltage across the inductor will be

$$v_{L\_bat} = \begin{cases} V_{DC} - v_{R\_bat} - v_{bat} & t \in T_{on} \\ -v_{R\_bat} - v_{bat} & t \in T_{off}, \end{cases} \tag{3.18}$$

being v_{R_bat} the voltage drop in the resistive part of the DC filter for the battery. Following the reasoning done for the AC side, the corresponding duty cycle for the battery can be expressed as

$$d_{DC\_bat} = \frac{(v_{bat\_m} + v_{R\_bat})\, T_c + L_{bat}\,(i_{bat\_ref} - i_{bat\_m})}{V_{DC} T_c}. \tag{3.19}$$

The case for the supercapacitor is completely analogous to the battery, therefore its duty cycle is given by the expression

$$d_{DC\_scap} = \frac{(v_{scap\_m} + v_{R\_scap})\, T_c + L_{scap}\,(i_{scap\_ref} - i_{scap\_m})}{V_{DC} T_c}. \tag{3.20}$$

Parameter	Description	Value
T_{sc}	Sampling time for the measures and control models	10^{-4} s
T_s	Fundamental time step for simulation	10^{-6} s
V_{1s}	Grid voltage fundamental component RMS	230 V
V_{3s}	Grid voltage 3rd harmonic component RMS	$5\%V_{1s}$ V
V_{5s}	Grid voltage 5rd harmonic component RMS	$4.5\%V_{1s}$ V
V_{7s}	Grid voltage 7rd harmonic component RMS	$4\%V_{1s}$ V
V_{DC_ref}	DC bus voltage reference	600 V
i_{ch-H_n}	Nominal current of the charger	10 A

Table 3.3: Parameters of the charger simulation

Component	Individual Harmonic Distortion (%)
I_{3L}	2.3%
I_{5L}	9.99%
I_{7L}	12.41%
I_{9L}	6.83%
THD	**30.67%**

Table 3.4: Typical harmonic content of the current demanded by a house. THD stands for Total Harmonic Distortion.

3.2.3 Charger simulation results

The simulation model described in the previous section will be now used to test its efficacy in several scenarios. The simulation parameters are the already presented in Table 3.1 and Table 3.2, plus the ones gathered in Table 3.3. For the first simulation test, the hybrid energy storage system is not used and only the battery is tested. Four different scenarios are carried out:

- Case A. The battery is being charged and reactive power is demanded from grid. P_{ref} = 1800 W, Q_{ref} = 1400 VAr. The house demands perfect sinusoidal current I_{1L} = 10 A with no harmonic content.

Variable	Total RMS (A)	Individual RMS (A)					THD (%)
	I	I_1	I_3	I_5	I_7	I_9	
i_L	5	4.78	1.21	0.48	0.59	0.33	30.67
i_s	9.244	9.24	0.19	0.09	0.14	0.1	2.94

Table 3.5: Harmonic content of the load and grid current for simulation results of case C

- Case B. The battery is discharging and injecting active and reactive power to the grid. $P_{ref} = -1800$ W, $Q_{ref} = -1400$ VAr. The house demands perfect sinusoidal current $I_{1L} = 10$ A with no harmonic content.

- Case C. Charging the battery and injecting reactive power. $P_{ref} = 1000$ W, $Q_{ref} = -600$ VAr. The house demands a fundamental component $I_{1L} = 5$ A, with the harmonics from Table 3.4.

- Case D. Discharging the battery and demanding reactive power. $P_{ref} = 1800$ W, $Q_{ref} = 1100$ VAr. The house demands a fundamental component $I_{1L} = 20$ A, with the harmonics from Table 3.4.

The results for the simulation tests described are presented in Figures 3.14-3.17. The variables $v_s, i_{ch\_m}, i_L, i_{ch-H\_ref}$ and i_s are represented in their steady state, while $v_{bat\_m}, i_{bat\_m}, i_{bat\_ref}, V_{DC\_m}$ and V_{DC_ref} are depicted from their initial values to steady state. The initial voltage of the DC bus equals the rectified grid voltage ($\sqrt{230}$ V). At $t = 0.05$ s the DC bus control model leads the DC voltage of the bus to its reference value, and at $t = 0.2$ s, all three strategies for the AC side of the converter (DSC, QSC and THC) are activated. For the remaining waveforms, two cycles are depicted when the steady state has been reached. As it can be seen, the charger is able to operate even under distorted grid voltage.

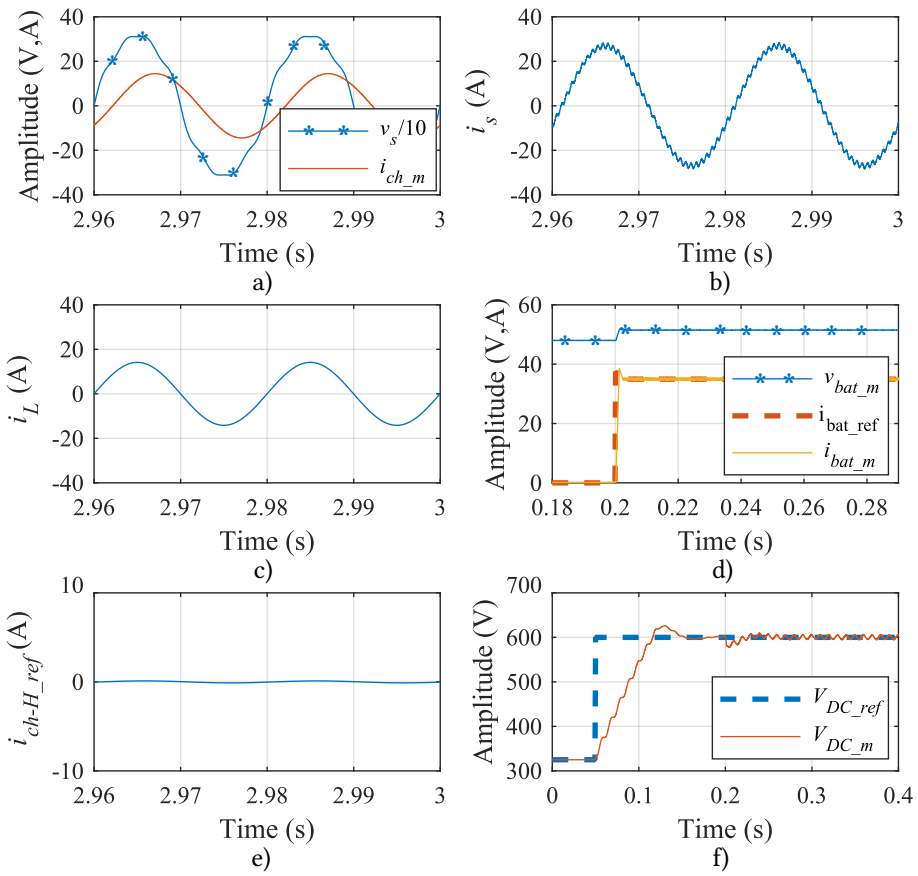

Figure 3.14: Simulation results of Case A. P_{ref} = 1800 W, Q_{ref} = 1400 VAr, I_{1L} = 10 A with no harmonic content. a) Grid voltage (blue asterisks markers) and charger current (solid orange). b) Grid current. c) House load current. d) Battery voltage (blue asterisks markers), battery's reference (dashed orange) and measured (solid yellow) current. e) THC reference current. f) DC bus reference (dashed blue) and measured (solid orange) voltages.

For the first two cases A and B, represented in Figure 3.14 and Figure 3.15, the house load demands current with no harmonic content, i.e, $i_{ch-H\_ref} = 0$. Therefore, the grid current i_s is also a pure sinusoidal wave, with only the switch-

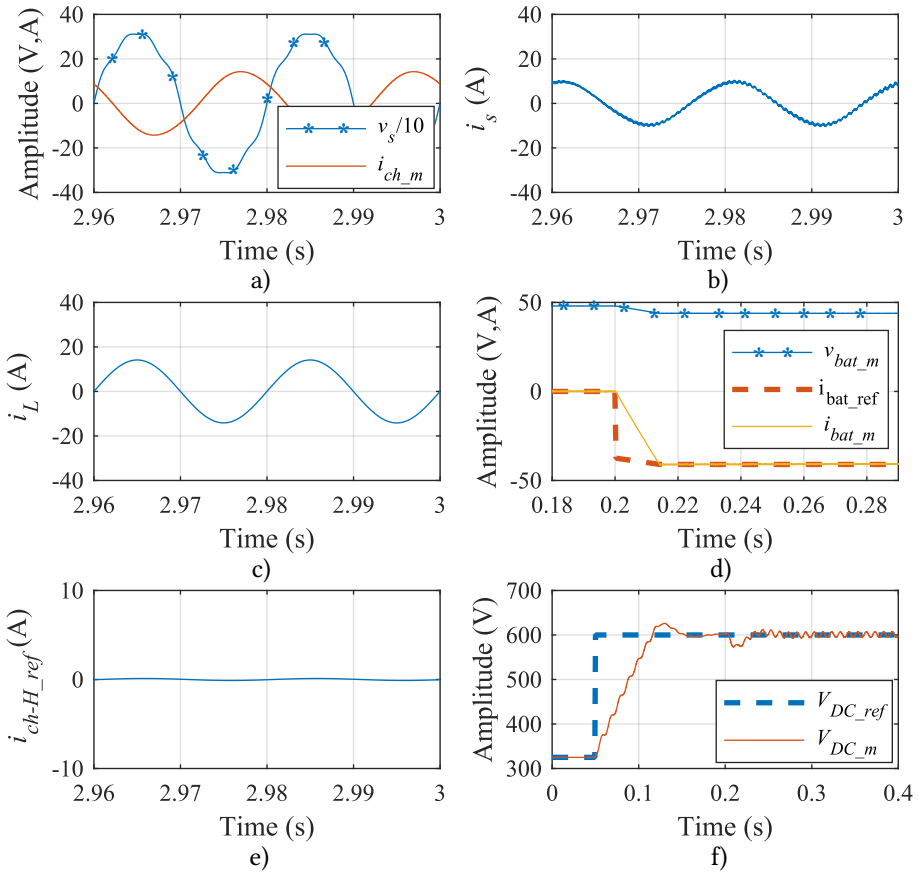

Figure 3.15: Simulation results of Case B. $P_{ref} = -1800$ W, $Q_{ref} = -1400$ VAr, $I_{1L} = 10$ A with no harmonic content. a) Grid voltage (blue asterisks markers) and charger current (solid orange). b) Grid current. c) House load current. d) Battery voltage (blue asterisks markers), battery's reference (dashed orange) and measured (solid yellow) current. e) THC reference current. f) DC bus reference (dashed blue) and measured (solid orange) voltages.

ing ripple.

For case C, the requierements for active and reactive power plus the harmonic content of the house represent a smaller current than the nominal charger current,

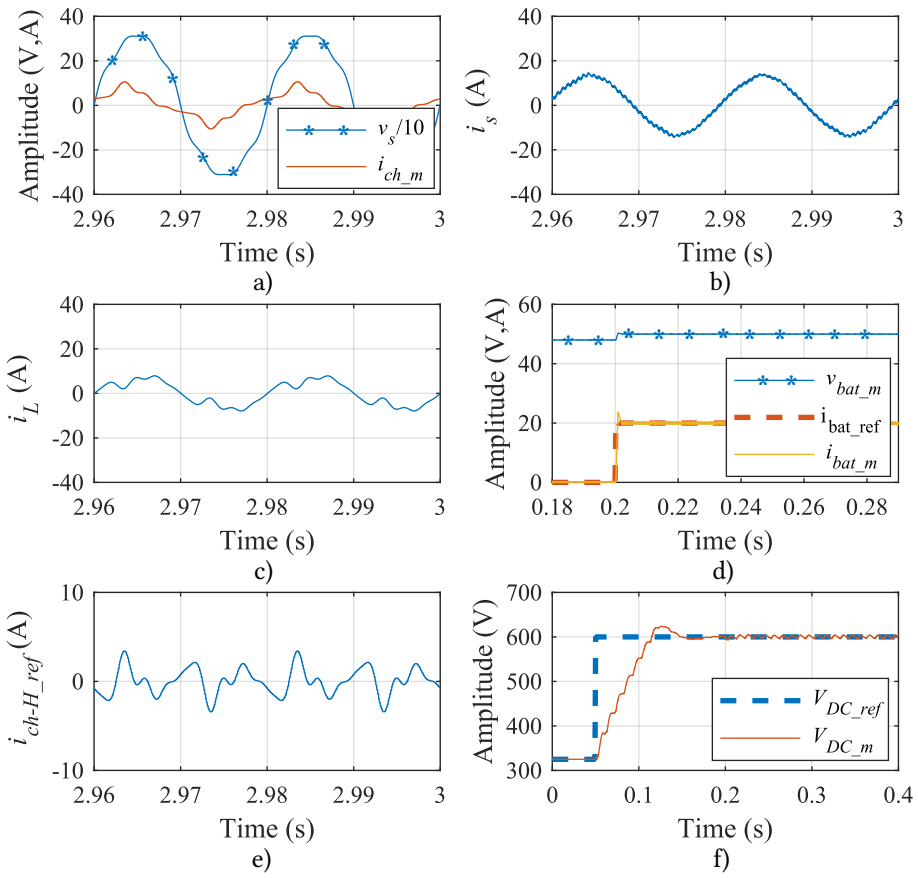

Figure 3.16: Simulation results of Case C. P_{ref} = 1000 W, Q_{ref} = −600 VAr, I_{1L} = 5 A with harmonic content. a) Grid voltage (blue asterisks markers) and charger current (solid orange). b) Grid current. c) House load current. d) Battery voltage (blue asterisks markers), battery's reference (dashed orange) and measured (solid yellow) current. e) THC reference current. f) DC bus reference (dashed blue) and measured (solid orange) voltages.

according to the system parameters in Table 3.3 and (3.7). Therefore, the system is able to do a full harmonic compensation following (3.8) and the grid current has no harmonic content, as it can be observed in Figure 3.16 b) and Table 3.5.

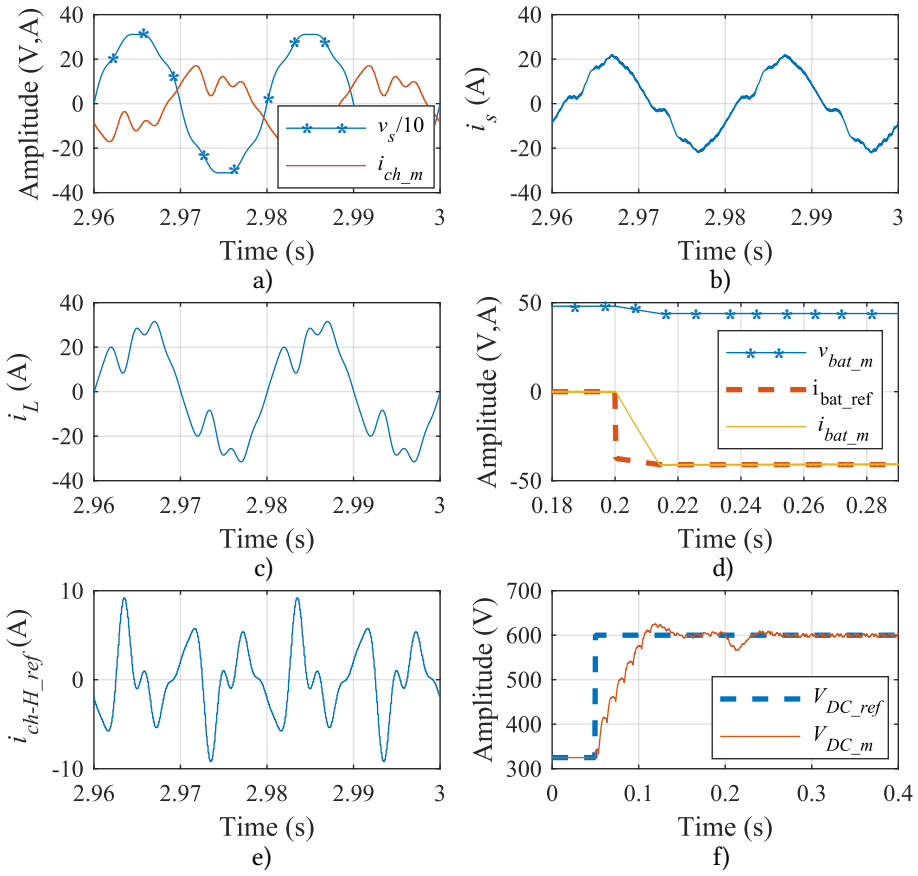

Figure 3.17: Simulation results of Case D. P_{ref} = 1800 W, Q_{ref} = 1100 VAr, I_{1L} = 20 A with harmonic content. a) Grid voltage (blue asterisks markers) and charger current (solid orange). b) Grid current. c) House load current. d) Battery voltage (blue asterisks markers), battery's reference (dashed orange) and measured (solid yellow) current. e) THC reference current. f) DC bus reference (dashed blue) and measured (solid orange) voltages.

In case D, the house current is greater than in the previous scenario. Thus, the charger is not able to provide the full i_{ch-h_ref} and it is scaled down following (3.9). The result is that the harmonic content is still present in the grid current

Variable	Total RMS (A)	Individual RMS (A)					THD (%)
	I	I_1	I_3	I_5	I_7	I_9	
i_L	20	19.11	4.83	1.91	2.37	1.31	30.67
i_s	13.405	13.26	1.56	0.62	0.82	0.49	14.56

Table 3.6: Harmonic content of the load and grid current for simulation results of case D

as the Figure 3.17 b) and the Table 3.6 show. Nevertheless, the THD of the i_s current is still reduced thanks to this partial compensation.

Finally, the hybrid storage system is tested by simulation. For this simulation test, only the DSC current strategy will be used for the AC side. A P_{ref} pattern will be applied and the DC reference current will be splitted for the battery and the supercapacitor. The results are presented in Figure 3.18. The pattern for the active power is depicted in Figure 3.18 b), and it is designed to make transitions from demanding power from the grid to injecting power to it. The goal is to avoid stressing the battery with sudden changes in current reference, taking advantage of the fast response of the supercapcitor. This can be observed in Figure 3.18 c) and Figure 3.18 d), where the reference and measured currents for both storage systems are shown. The changes in active power reference affects the voltage in the DC bus, but the system is able to maintain it at the reference setpoint as can be observed in Figure 3.18 a).

3.2.4 Charger experimental results

The charger described in the previous section is built in a prototype in order to validate the feasibility of the control strategies. A picture of the experimental setup is shown in Figure 3.19. It is composed of the following components

- Grid emulator. For the two first experiments, the grid will have harmonic content previously described in Table 3.3, to simulate the worse scenari-

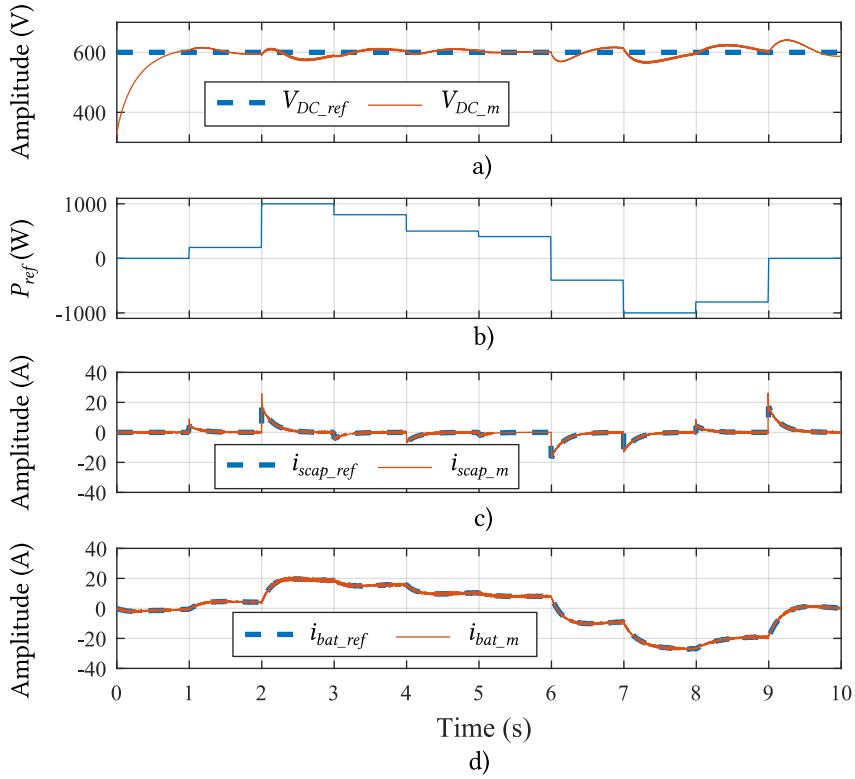

Figure 3.18: Simulation results using the hybrid storage with battery and supercapacitor. a) Reference (dashed blue) and measured (solid orange) DC bus voltage. b) Reference setpoint of active power. c) Reference (dashed blue) and measured (solid orange) supercapacitor current. d) Reference (dashed blue) and measured (solid orange) battery current.

ous the charger can work with. The device used is a Cinergia GE15 grid emulator.

- Power converter. A 4 branch IGBT converter SEMITEACH from SEMIKRON is employed for the power electronics. Two branches are used for the AC/DC converter and one branch for each DC/DC converter. Also, inductive filters for both the AC and DC sides are included.

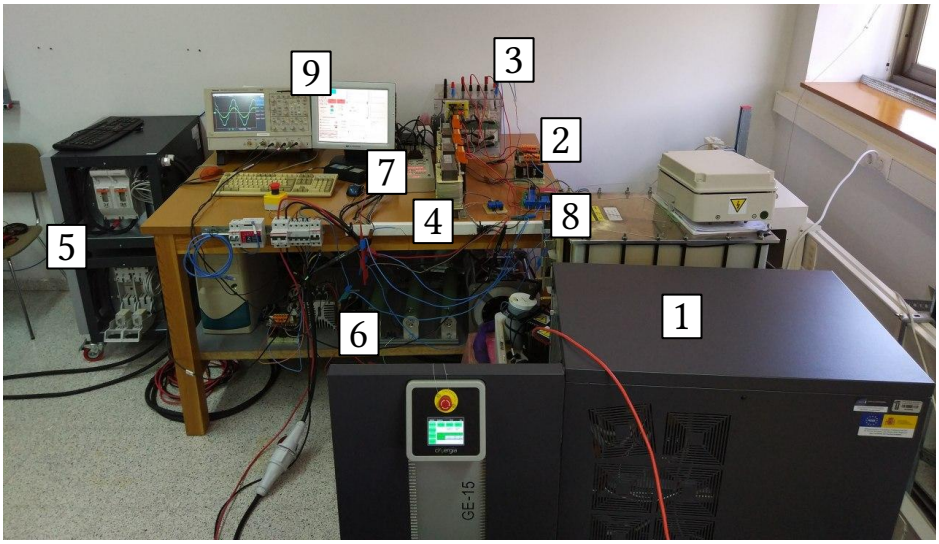

Figure 3.19: Experimental prototipe of the charger proposed: 1. Grid emulator; 2. AC filter; 3. Four branch converter; 4. DC filter; 5. Battery ESS; 6. Non-lineal load; 7. dSPACE; 8. Measuring board; 9. Host PC and oscilloscope

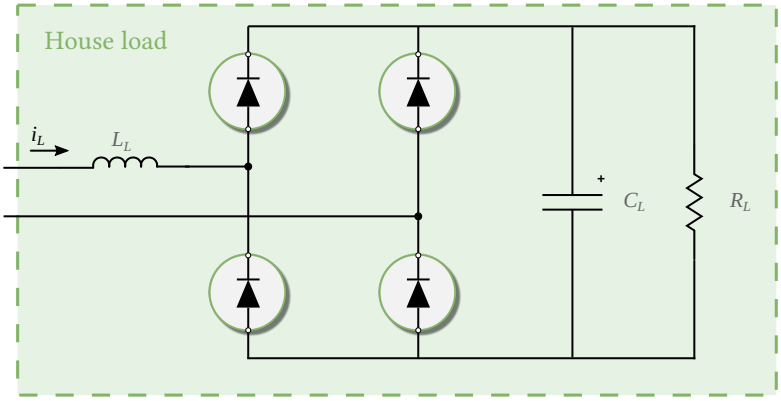

Figure 3.20: Non-lineal load providing harmonic content used for the experiments

- Energy storage. A Li-Ion battery module is employed for the first four experiments, the supercapacitor will be added in the last experiments to

Parameter	Description	Value
V_{1s}	Grid fundamental voltage	230 V
V_{5s}	Grid 5rd harmonic component RMS	$6\%V_{1s}$ V
V_{7s}	Grid 7rd harmonic component RMS	$5\%V_{1s}$ V
V_{DC_ref}	DC bus reference voltage	500 V
S_n	Charger nominal apparent power	10^3 VA
I_{ch-n}	Charger nominal current	4.35 A
v_{bat-n}	Battery nominal voltage	55.5 V
f_c	Switching frequency	10×10^3 Hz
f_s	Sampling frequency	5×10^3 Hz
R_{AC}	AC inductive filter resistance	1.34×10^{-3} Ω
L_{AC}	AC inductive filter inductance	8.4×10^{-3} H
R_{bat}	Battery inductive filter resistance	0.38 Ω
L_{bat}	Battery inductive filter inductance	15×10^{-3} H
R_L	Non-linear load resistance	110 Ω
L_L	Non-linear load inductor	110 Ω
C_L	Non-linear load capacitor	1.8×10^{-3} F

Table 3.7: Parameters of the experimental setup

test the hybridation.

- Control platform. Made up of a dSPACE DS1104 controlled by a PC running ControlDesk software. The models developed during the simulation stage are compiled into the platform.

- Measuring board. In charge of measuring all the variables needed depicted in Figure 3.2. It uses Hall-effect voltage and current sensors (LV25-P and LA55-P, respectively).

- Non-lineal load. To simulate the presence of the house demanding harmonic content in its current, the non-lineal load depicted in Figure 3.20 is built. It is made up of a inductive filter followed by a passive diode rectifier, which feeds a parallel RC load.

P_{ref} **(W)**	Q_{1_ref} **(VAr)**	P_m **(W)**	Q_{1_m} **(VAr)**	I_{ch} (A)	S_m (VA)	dPF	PF
1000	0	952	25	4.16	968.6	1	0.99
-800	600	-743	537	4.01	865.3	0.81	0.8
400	200	396	180	3.28	752.9	0.91	0.53
900	200	839	188	4.2	964.2	0.98	0.87

Table 3.8: Power terms in the experiments conducted

The general parameters of the prototype are presented in Table 3.7. Four experiments are conducted, two of them with distorted grid voltage and the other two with sinusoidal voltage supply. A Fluke 435 Power Quality Analyzer is used to measure the power terms developed during the tests. They are gathered in Table 3.8, together with the RMS value of the charger current I_{ch} and the displacement Power Factor (dPF) and Power Factor (PF). The former measures the displacement between the voltage and current fundamental waves, which is the classical power factor in case of linear loads supplied by sinusoidal voltage, and its value for the experiments can be obtained from the measured power terms as

$$dPF = \cos\left(\text{atan}\left(\frac{\text{Q}_{1\_\text{m}}}{\text{P}_{1\_\text{m}}}\right)\right) \tag{3.21}$$

where the subindex 1 in the power terms refer to the fundamental values. On the other hand, the PF takes into account all the power terms produced by the harmonic components of the currents caused by non lineal loads and is equal to

$$PF = \frac{P_m}{S_m}, \tag{3.22}$$

where S_m is the total apparent power. Lastly, since the battery is the one in charge of providing with the energy for the DC bus as it was explained in Section 3.2.2.1, it will cover for the system losses while transferring the energy from the grid to the storage and vice versa. Thus, the reference setpoint for the active

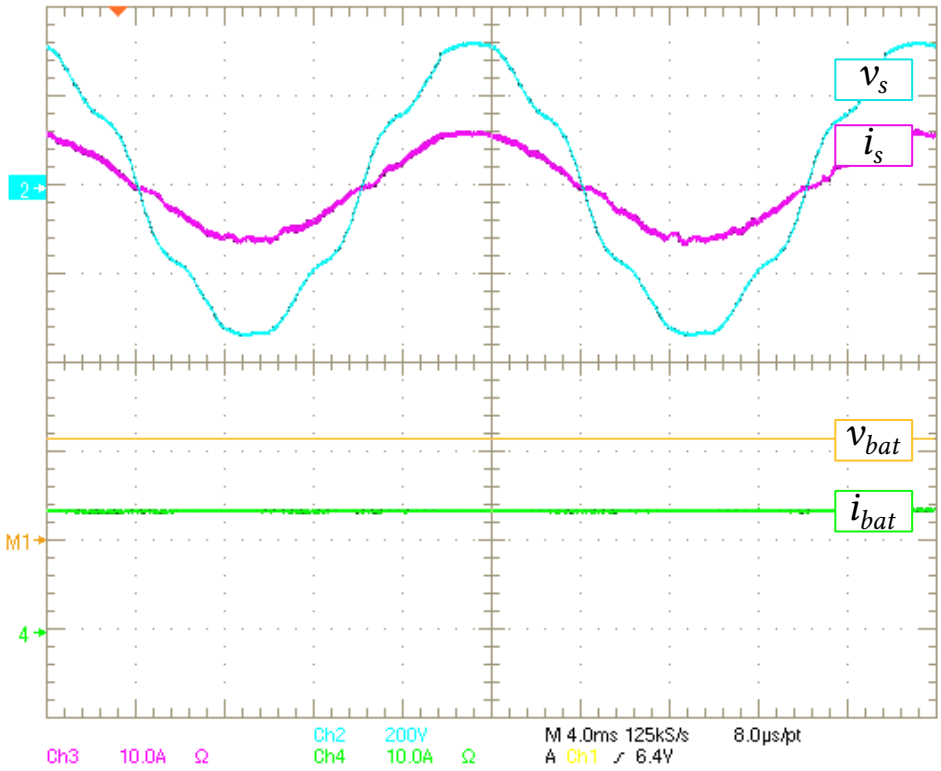

Figure 3.21: Experimental results testing the DSC control strategy. Grid voltage (200 V/div), grid current (10 A/div), battery voltage (50 V/div) and battery current (10 A/div)

power P_{ref} will be met on the grid side. The power at the battery will be higher when transferring power to the grid, and lower when the energy is transferred from the grid to the storage.

3.2.4.1 Active power control

First, the control of the active power managed by the charger using the DSC strategy is validated. To that aim, the charger is operated at its nominal power, i.e., $P_{ref} = 1000$ W. In this tests, no current for the house is considered ($i_L = 0$).

Nevertheless, the grid voltage used is distorted with the harmonic content in Table 3.7. The results of this experiments are presented in Figure 3.21 and in Table 3.8. Since the power reference setpoint is positive, the battery is charging and the battery current is positive. Moreover, the charger current i_{ch} is in phase with the voltage since it is drawing power from the grid. Although the grid voltage is distorted, the charger is able to extract the fundamental component v_{1s} and the current is in phase with it. This can be deduced from Table 3.8, since the dPF is equal to 1. Since there are no harmonics components in the current, but there are in the voltage, the PF is close but not equal to 1. The reason is that although $P = P_1$, $S \neq S_1$ due to the existance of more apparent power terms because of the voltage harmonics. There is error in the power demanded from the grid, but it is below 4.8 %.

3.2.4.2 Active power and fundamental reactive power control

For the second experiment, both the DSC and QSC control strategies are going to be tested to control the active and reactive power. In this case, the active power setpoint is $P_{ref} = -800$ W, so the battery will be transferring energy to the grid. Also, a reactive power reference is set following $Q_{1ref} = 600$ VAr. The reference is positive, meaning that the charger will absorb fundamental reactive power from the grid. Also, the grid voltage is distorted with the same harmonic content as the last case. The results are depicted in Figure 3.22, and the power measurements collected in Table 3.8. It can be observed how i_{ch} is no longer in phase with the voltage, since power is being taken from the grid and reactive power is being consumed. The power measurements show a 7 % and 10.5 % error compared to the active and reactive power setpoints, respectively. The dPF value is 0.81, which is coherent with the references set and (3.21).

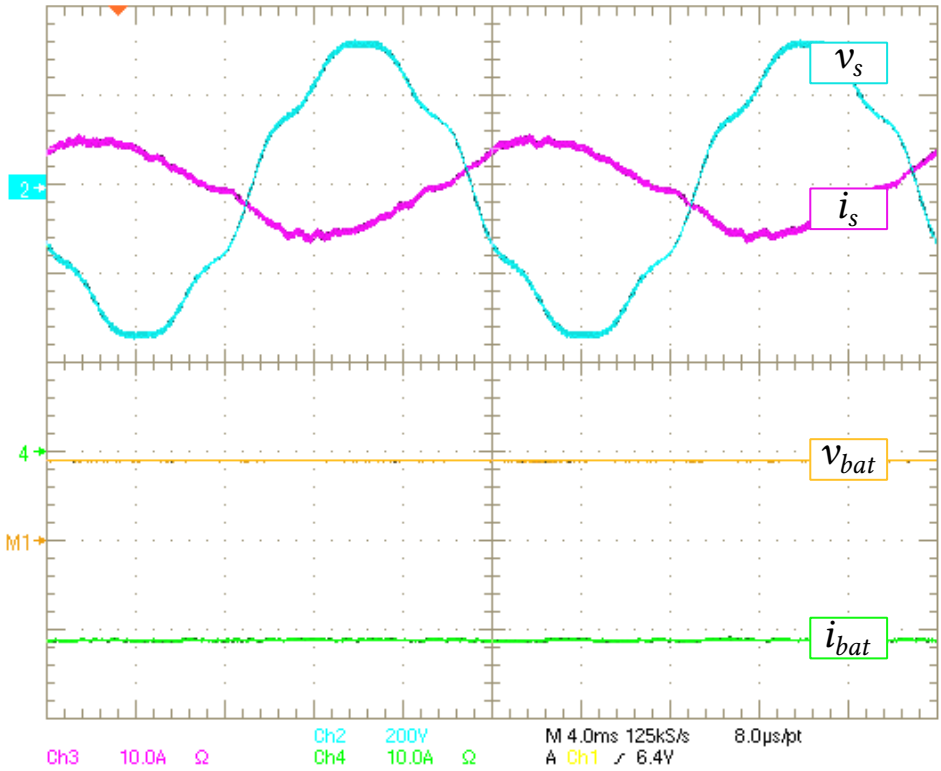

Figure 3.22: Experimental results testing the DSC and QSC control strategy. Grid voltage (200 V/div), grid current (10 A/div), battery voltage (50 V/div) and battery current (10 A/div)

	I_1 **(A)**	I_3 **(A)**	I_5 **(A)**	I_H **(A)**	**THD (%)**
i_L	3.5	2.5	1.2	2.828	80.8
i_s	5.3	0.6	0.3	0.95	17.9
i_{ch}	1.8	2.2	1.1	2.67	148.4

Table 3.9: Harmonic current components without saturation in THC

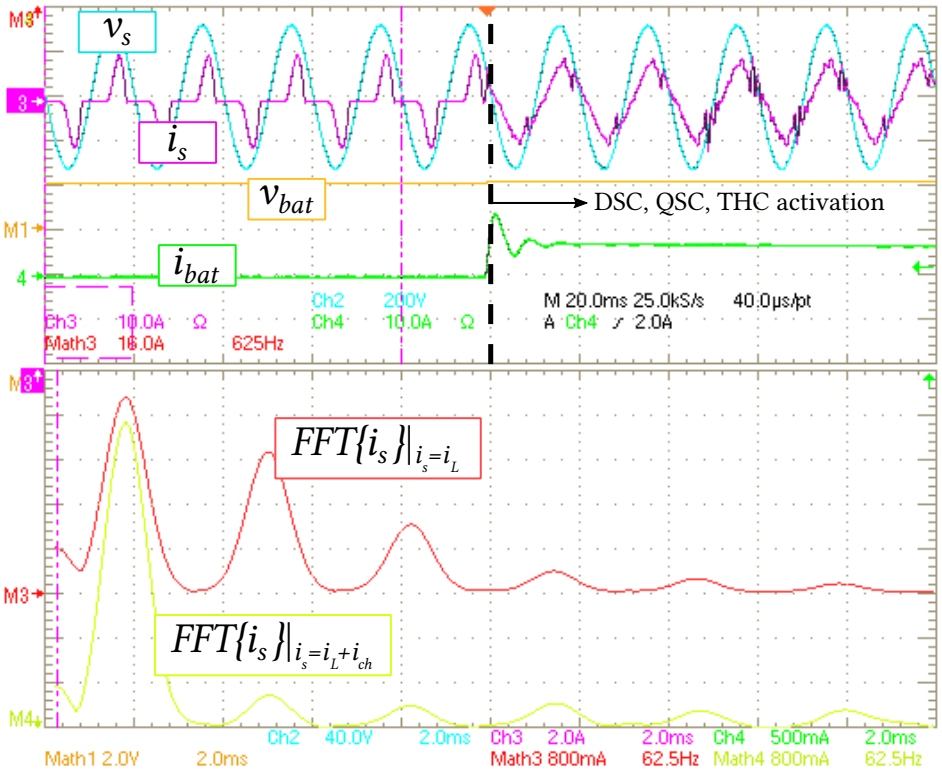

Figure 3.23: Experimental results testing the DSC, QSC and THC with no saturation. Grid voltage (200 V/div), grid current (10 A/div), battery voltage (50 V/div) and battery current (10 A/div). Harmonic spectrum of the grid current before and after the activation of the charger.

3.2.4.3 Active power, reactive power and harmonic control

Next, all the strategies discussed, DSC, QSC and THC will be testes in the last two experiments. For the first one, THC compensation with no saturation is considered. Then, the second one will increase the demand from the charger so it will have to saturate i_{ch-H_ref} in order to not exceed the nominal current.

The grid voltage for the following experiments is not distorted anymore. At the beginning, only the load will be demanding current and so $i_s = i_L$. Then,

	I_1 (A)	I_3 (A)	I_5 (A)	I_H (A)	THD (%)
i_L	3.5	2.5	1.2	2.828	80.8
i_s	7.2	1.2	0.4	1.4	19.4
i_{ch}	3.7	1.6	0.9	1.9	51.2

Table 3.10: Harmonic current components with saturation in THC

the charger with the three control strategies is turned on and the grid current will then be $i_s = i_L + i_{ch}$. The house current is coming from the load defined in Figure 3.20, whose RMS value is equal to 4.45 A. The fundamental component RMS I_{1L} is equal 3.51 A and the harmonic content $I_{hL} = 2.73$ A.

The first experiment is depicted in Figure 3.23, where the references are $P_{ref} = 400$ W and $Q_{1ref} = 200$ VAr. For this references, the values of the direct and quadrature current components are $I_{ch-D\_ref} = 1.74$ A and $I_{ch-Q\_ref} = 0.87$ A, according to (3.5) and (3.6). Then, taking into account the charger nominal current from Table 3.7 and using (3.7), one can get that $I_{ch-H\_max} = 3.89$ A. Since this value is greater than the load harmonic content I_{hL}, no saturation is needed according to (3.9). The battery is charging due to the positive reference setpoint, and so the current rises when the charger is activated. The figure also presents two frequency spectra. The upper one corresponds to the load current, equal to the grid current before the charger activation. The lower corresponds to the grid current, which is equal to the sum of both the load and the charger currents when the latter is activated. It can be seen how, the moment the charger is activated, the THC strategy cancels out most of the harmonic content in i_s. This can also be appreciated from the harmonic RMS values gathered in Table 3.9, which confirm the correct operation of the charger. Also, from Table 3.8, it can be seen how the power active and reactive references are met within a 1% and 10% error. Moreover, the dPF is very close to the theoretical value.

For the next experiment, the same load conditions are applied, but this time

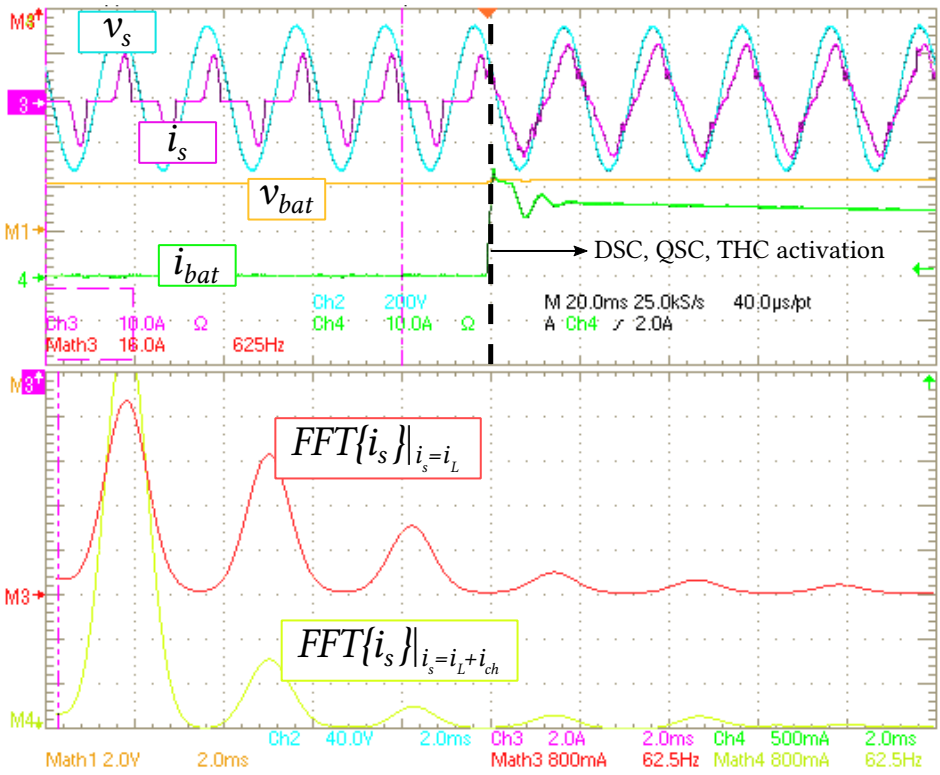

Figure 3.24: Experimental results testing the DSC, QSC and THC with saturation.Grid voltage (200 V/div), grid current (10 A/div), battery voltage (50 V/div) and battery current (10 A/div). Harmonic spectrum of the grid current before and after the activation of the charger.

P_{ref} = 900 W and Q_{1ref} = 200 VAr. Thus, following the same procedure as before, one can get that I_{ch-H_max} = 1.68 A for this case. Therefore, since I_{hL} is greater, the i_{ch-H_ref} current is scaled. From the results gathered in Table 3.10 and the harmonic spectra in Figure 3.24, the partial cancellation is clear. From the table results, it can be observed how the THD in this case is higher than in the previous one, but not that much. This is due to the fundamental component I_{1s} being greatly raised because of the increase in the active power reference.

Parameter	Description	Value
V_{1s}	Grid fundamental voltage	150 V
V_{DC_ref}	DC bus reference voltage	300 V
v_{bat-n}	Battery nominal voltage	55.5 V
v_{scap-n}	Battery nominal voltage	30 V
f_c	Switching frequency	10×10^3 Hz
f_s	Sampling frequency	5×10^3 Hz
R_{AC}	AC inductive filter resistance	1.34×10^{-3} Ω
L_{AC}	AC inductive filter inductance	8.4×10^{-3} H
R_{bat}	Battery inductive filter resistance	0.38 Ω
L_{bat}	Battery inductive filter inductance	6×10^{-3} H
R_{scap}	Supercapacitor inductive filter resistance	0.4 Ω
L_{scap}	Supercapacitor inductive filter inductance	8.4×10^{-3} H

Table 3.11: Parameters of the experimental setup for the hybridate storage

The results in fulfilling the power terms are displayed also in Table 3.8, where it can be seen that the error for the active and reactive power references are 6.8% and 6%, respectively. This results validate the operation of the charger in the situations described.

3.2.4.4 Storage hybridation

The last set of experiments for this section includes the hybridation storage including the supercapacitor. The tests are carried out using the topology from Figure 3.3 and the parameters collected in Table 3.11. Since the main goal of these experiments is to test the behaviour of the system when the active power reference is splitted among the storage systems, the non lineal load will not be employed.

The first is depicted in Figure 3.25, where the charger is turned on at a certain time, setting $P_{ref} = 500$ W. The oscilloscope capture shows how the DSC strategy demans pure sinusoidal current from the grid, being the charger current

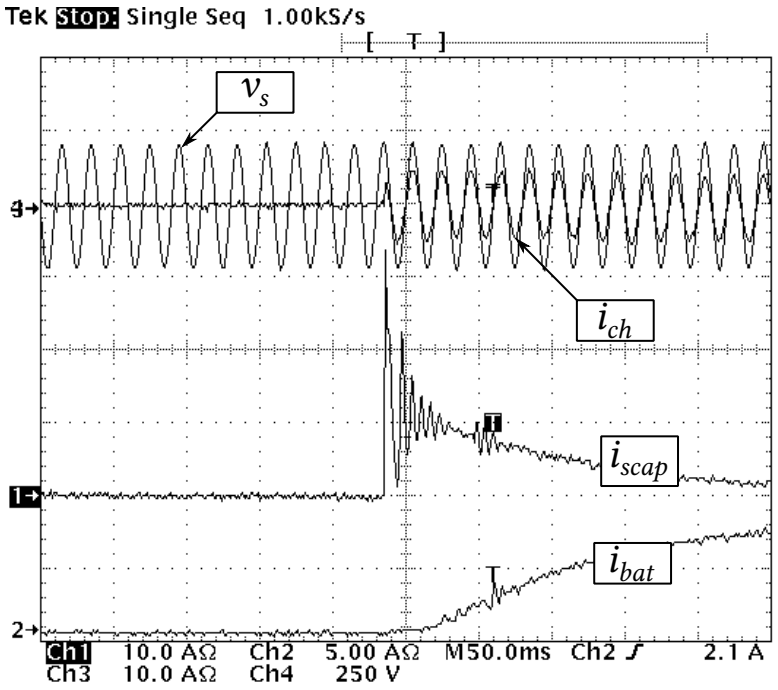

Figure 3.25: Experiment results testing DSC and hybrid storage. Charger turning on setting a $P_{ref} = 500$ W. Grid voltage (250 V/div), charger current (10 A/div), supercapacitor current (10 A/div) and battery current (5 A/div).

completely in phase with the grid voltage. This energy is transferred to the DC bus, and at the same time, using (3.11), the power reference is used to generate references for the storage systems. The current assigned to the supercapacitor will be the initial peak, while the battery slowly takes over.

The next experiment will consist in a change of reference to the charger from a positive power reference to a negative one. The results are presented in Figure 3.26, in a similar fashion to the previous experiment. In this case, the charger current changes its phase to change from demanding to injecting power to the grid. So does the battery current, which slowly moves from a positive value

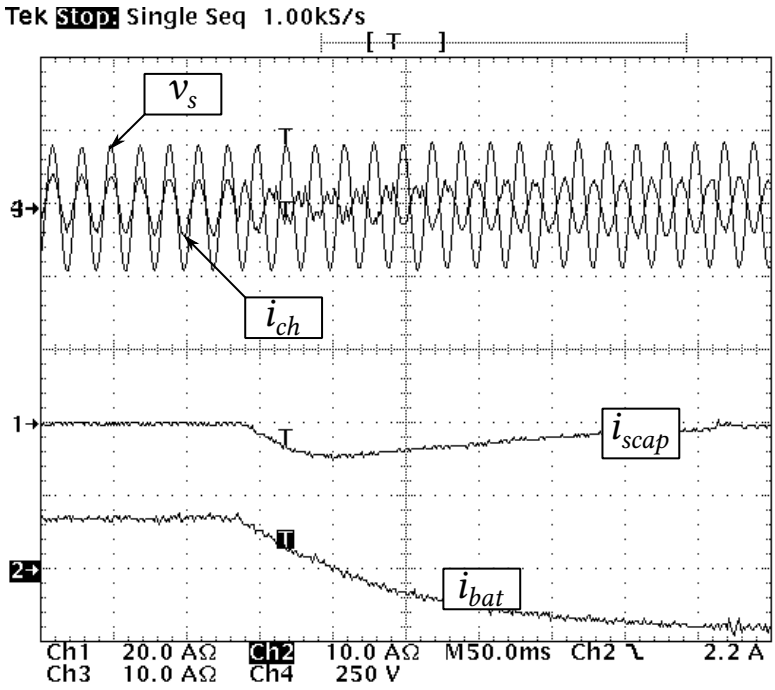

Figure 3.26: Experiment results testing reference change and hybrid storage. Charger behaviour when changing from a $P_{ref} = 500$ W to a $P_{ref} = -500$ W. Grid voltage (250 V/div), charger current (10 A/div), supercapacitor current (10 A/div) and battery current (10 A/div).

that meant charging, to a negative one. The supercapacitor helps this transition supplying the initial peak of current.

The last experiment of this section will explore the reference changes deeper, as it was done in the simulation presented in Section 3.2.3. To this aim, the DSC will be employed with a power reference pattern defined by

$$P_{ref} = \{0, 200, 1000, 800, 500, 400, -400, -1000, -800, 0\}\,\text{W}. \tag{3.23}$$

The results of the experiments are presented in Figure 3.27. As in previous experiments, the power reference is used for splitting the DC reference currents

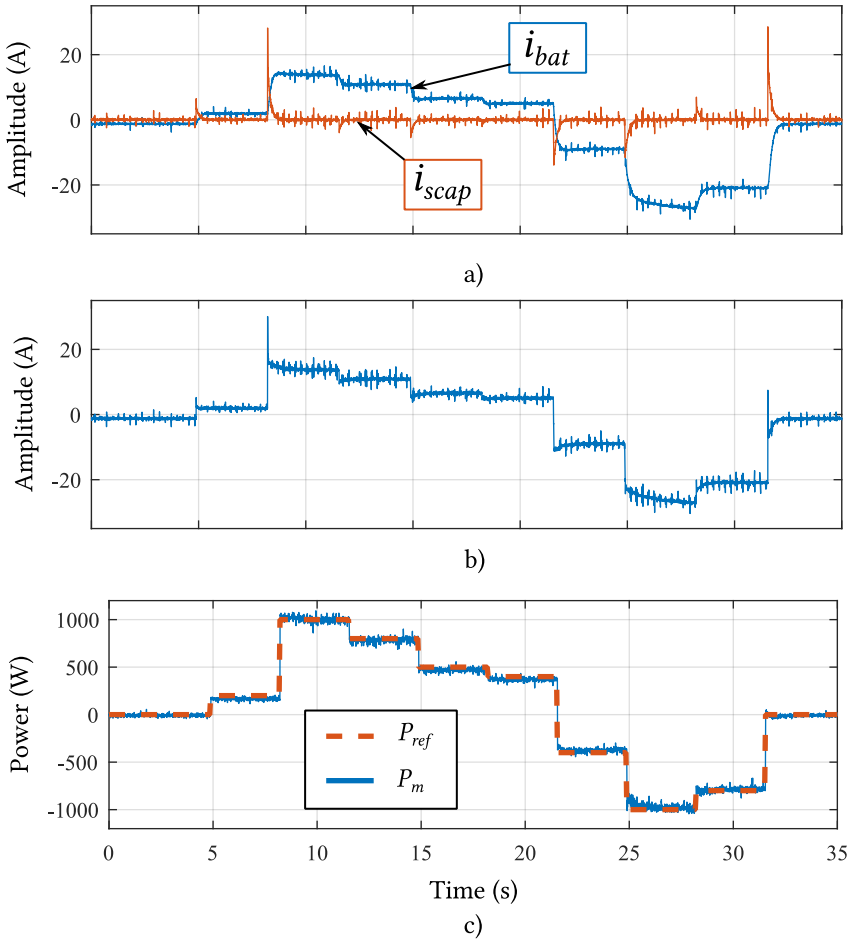

Figure 3.27: Experiment results testing P_{ref} pattern and hybrid storage. a) Battery and supercapacitor currents. b) Total current for storage system $i_{bat\_m} + i_{scap\_m}$. c) Power reference pattern and measured power in AC side.

as it can be observed in Figure 3.27 a). It can be seen how the supercapacitor current has high peaks when a change in the power reference is made. The highest peaks correspond to the higher power changes, e.g., from 200 to 1000 W. Figure 3.27 b) shows the sum of both currents, that has a stair waveform, since

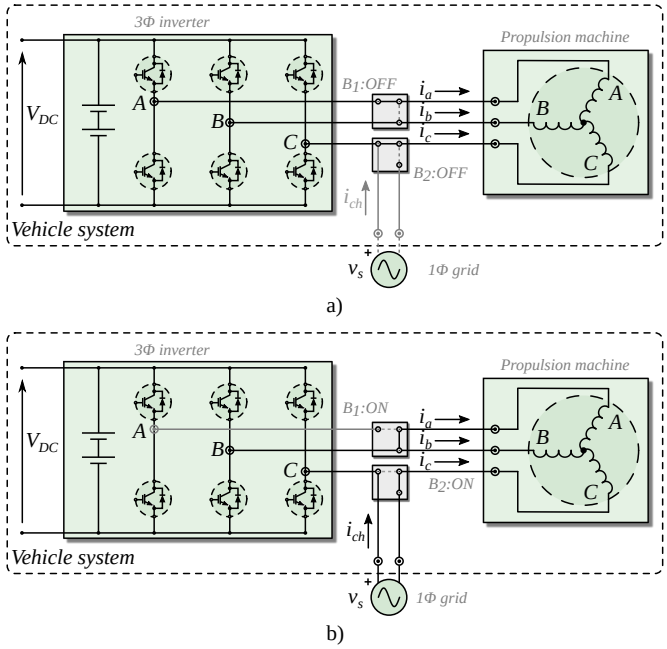

Figure 3.28: Connection of single-phase grid to a three-phase converter. a) Propulsion mode. b) Charging mode

according to Figure 3.9 it is just the power reference divided by the battery voltage. Finally, Figure 3.27 c) shows both the power reference pattern and the power measured in the grid side. It can be observed that the two waveforms match almost perfectly. Therefore, the good operation of the storage hybridation for the charger proposed is confirmed.

3.3 Integrated On-Board topology

Due to the similarity of the power electronics found in the charger proposed and the one found in a typical vehicle system, it is interesting to reuse as many components as possible. The most used machine for EV propulsion is the PMSM,

as the one used in the previous chapter, so it is desirable to use it during the charging process too. By looking at Figure 3.3, one can see that the windings of the propulsion machine could be used for the AC inductor L_{AC}. Moreover, even if only two branches of the converter are needed for a single-phase connection to the grid, the three-phase converter of the vehicle could serve the same purpose. This situation is depicted in Figure 3.28, where the single-phase connection of the grid to the converter is shown. By manipulating the internal connections of the phases, one can achieve a dual purpose converter, that allows to drive the machine and transfer energy from the grid to the storage system attached to the DC bus. Nevertheless, using the motor windings as inductors give raise to magnetic fields in the airgap. These fields will interactuate with the field established by the rotor magnets, given that the machine is a PMSM. This fact will cause the appearance of torque in the motor shaft, and the nature of this torque will depend on the grid characteristics and the connection made. This torque will be properly analized in the following section.

3.3.1 Torque analysis

During drive mode, the internal connection of the system is the one depicted in Figure 3.28 a), in which the motor phases are connected to the midpoints of the three branches. This is achieved by setting the commutators B1 and B2 to *OFF*. The currents i_a, i_b, i_c will be determined by the drive controller using the FOC described in Section 2.2.3.1. However, when a connection of the system with the grid is made as shown in Figure 3.28 b) by setting the commutators to *ON*, the typical connection for single phase integrated charging is made. Then the relationship between the phase currents and the current demanded form the grid can be established as

$$\begin{aligned} i_c &= -i_{ch} \\ i_a &= i_b = -\frac{i_c}{2}. \end{aligned} \tag{3.24}$$

The charger current i_{ch} has already been described as a mix of reference currents coming from the different strategies employed as in (3.4). However, for the sake of simplicity, for this section only the reference from the DSC control will be used and thus, the current will be in phase with the grid voltage. Therefore, the current (3.5) can be ideally described as

$$i_{ch} = \sqrt{2} I_{ch} \cos(2\pi f_g t), \tag{3.25}$$

where f_g is the grid frequency, 50 Hz in Europe, and t is the time variable. Taking these currents to field coordinates using the transformations introduced in Section 2.2.1, the direct and quadrature currents can be expressed as

$$\begin{aligned} i_d &= -i_{ch} \cos\left(\theta_e + \frac{2\pi}{3}\right) \\ i_q &= i_{ch} \sin\left(\theta_e + \frac{2\pi}{3}\right). \end{aligned} \tag{3.26}$$

The zero component is ignored as a three-wire balanced system with no harmonics is considered. Recalling the expression for the electromagnetic torque (2.7) introduced in the previous chapter and using (3.26), the torque generated by the motor when in charging mode can be expressed as

$$\begin{aligned} T_e = -\frac{3}{4} p \left(L_d - L_q\right) I_{ch}^2 \left(1 + \cos(4\pi f_g t)\right) \sin\left(2\theta_e + \frac{4\pi}{3}\right) + \\ \lambda \sqrt{2} I_{ch} \cos\left(2\pi f_g t\right) \sin\left(\theta_e + \frac{2\pi}{3}\right). \end{aligned} \tag{3.27}$$

The torque expressed by (3.27) depends on the rotor electric angle θ_e and is time dependant, pulsating according to the grid frequency. Figure 3.29 shows a spatial representation of this torque, for the PMSM parameters gathered in Table 2.3 and a charging current with a RMS value $I_{ch} = 16$ A. It can be observed how the motor will produce a pulsating torque whose peak value depends on the electrical rotor position. From (3.27) it can be deduced that the maximum and minimum values of the torque are given by

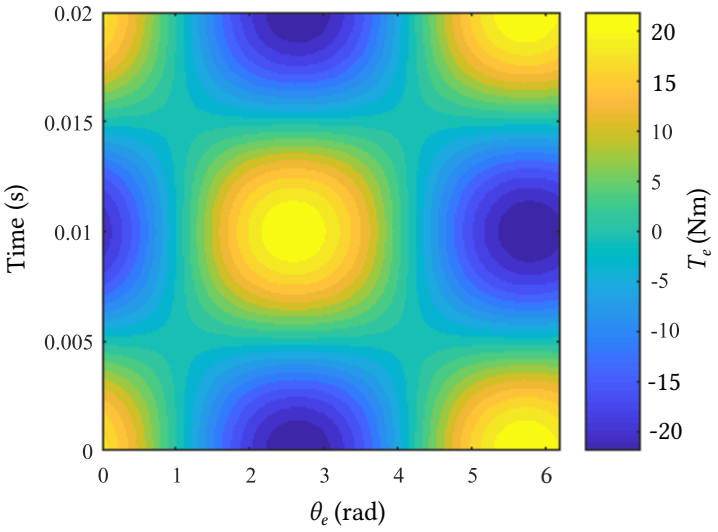

Figure 3.29: Electromagnetic torque developed by the motor when operating in charging mode. The torque is represented in the z dimension using the color scale.

$$\begin{aligned} T_{min} \Rightarrow \theta_e &= \left\{ \frac{\pi}{3}, \frac{4\pi}{3} \right\} \text{rad}, \\ T_{max} \Rightarrow \theta_e &= \left\{ \frac{5\pi}{6}, \frac{11\pi}{6} \right\} \text{rad}. \end{aligned} \tag{3.28}$$

In other words, when the rotor is aligned with the axis of the phase that has the connection to the grid, the torque developed will be 0. This values can be confirmed with Figure 3.29. Taking into account that the connection made follows Figure 3.28 b), the phase connected to the grid is phase c. Thus, in the axis defined by angles $\pi/3$ and $4\pi/3$, there is no torque.

Another conclussion driven by (3.28) is that the torque in the motor will have three components in the frequency analysis. Two of them are dependent on the difference of the inductances $L_d - L_q$, and are located at 0 (a DC component) and $2f_g$ Hz. The third one is proportional to the rotor field and is located at f_g Hz. This can be observed in Figure 3.30, where these three components are plotted

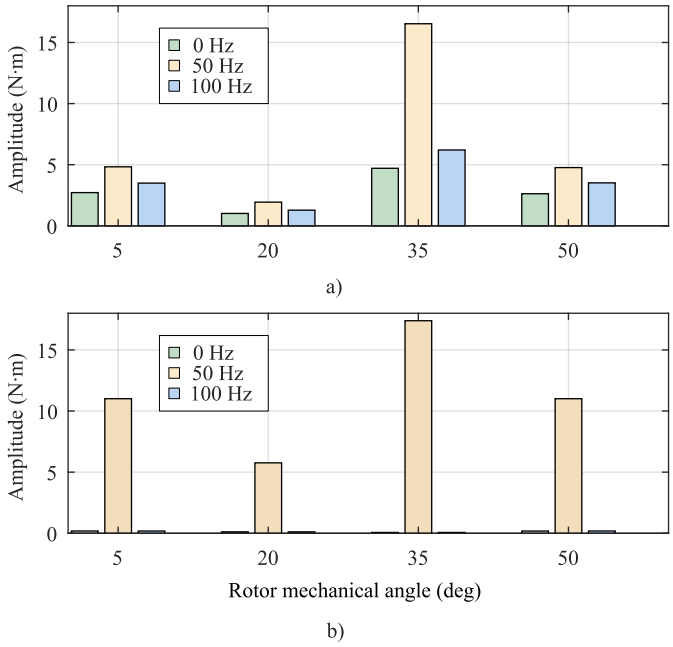

Figure 3.30: Torque components developed by the machine when the system is operating in charging mode. a) IMPMSM. b) SMPMSM

for several rotor positions. The simulation is made in the same conditions as the previous one, but for Figure 3.30 b), the L_q is modified so the salience factor is 5, i.e., $L_q/L_d = 5$. This is tipically the case with Interior Mounted PMSM (IMPMSM). It can be observed how the torque developed is affected by the type of machine considered, being the DC and $2f_g$ components almost negligible for the case of a SMPMSM.

If the grid is connected to any of the other two motor windings, similar results are to be expected, at rotor angles shifted by $2\pi/3$. In any case, this oscillations in the torque developed would represent a hazard to any device attached to the rotor shaft. The logical solution would be to align the rotor with the grid-connected phase to avoid torque generation while charging, but this could not always be

possible or need aditional components to let the motor spin without moving the vehicle. Therefore, a more general solution is required to avoid causing damage to other parts of the system while integrating the charger.

3.3.2 Control modelling

Looking again at Figure 3.28, one can see that by setting B1 to *OFF* and B2 to *ON*, the grid is still connected to phase C but (3.24) does not hold anymore. Instead, one could also control another current besides the charger current, and the third one would vary accordingly. For instance, given that i_c is already controlled as

$$i_c = -i_{ch} = -\sqrt{2} I_s \cos 2\pi f_g t, \tag{3.29}$$

and by controlling another one, e.g., i_b, the last one will be given by

$$i_a = -\left(i_b + i_c\right). \tag{3.30}$$

For cancelling the rotor oscillation due to the torque generaion while charging, it would necessary to cancel i_q, according to (2.7). By definition, the q-axis current is given by

$$i_q = \sqrt{\frac{2}{3}}\left[-i_a \sin(\theta_e) - i_b \sin\left(\theta_e - \frac{2\pi}{3}\right) - i_c \sin\left(\theta_e + \frac{2\pi}{3}\right)\right] \tag{3.31}$$

Taking into account that we can now control 2 currents, using (3.30) and forcing $i_q = 0$ in (3.31), one can write

$$i_b = i_c \left[\frac{\sin\left(\theta_e\right) - \sin\left(\theta_e + \frac{2\pi}{3}\right)}{\sin\left(\theta_e - \frac{2\pi}{3}\right) - \sin\left(\theta_e\right)}\right]. \tag{3.32}$$

In order to test the validity of the current control proposed, a simple simulation model is developed using the Simulink powerlib library. The simulation model is depicted in Figure 3.31. The inverter is simplified and modelled as simple current sources for the following examples.

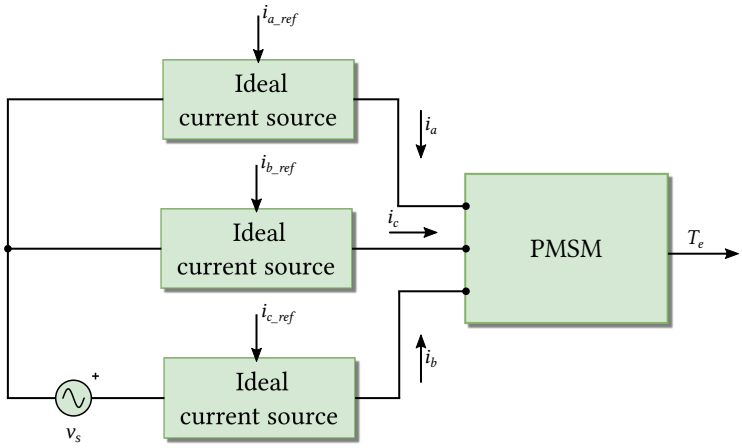

Figure 3.31: Simplified simulation model for analyzing the charging torque

Ideally, forcing the current in phase to follow (3.32) would suffice to cancel the torque generation. However, in that expression there are certain rotor angle values that cancel the denominator. This would mean that infinite current circulating for the remaining phases not connected to the grid would be necessary to cancel the torque produced by the third one. This can be observed in Figure 3.32 a), where the results of using the simulation model from Figure 3.31 for a complete electrical revolution are presented. The value of the grid voltage is $V_s = 230$ V (no harmonics considered), and the charging current is $I_c = 16$ A. The reference for the currents i_b, i_a are calculated following (3.32) and (3.30), respectively. It can be observed how for the angles where the maximum torque is generated, the RMS values for the non-grid currents rise up to impossible values.

In order to cancel the torque, no matter what the position of the rotor is, but taking into account the limitations of the machine windings, some restrictions have to be applied to (3.32). To maintain the condition $i_q = 0$, all three currents have to be scaled down simultaneously. To that aim, a scaling factor is introduced

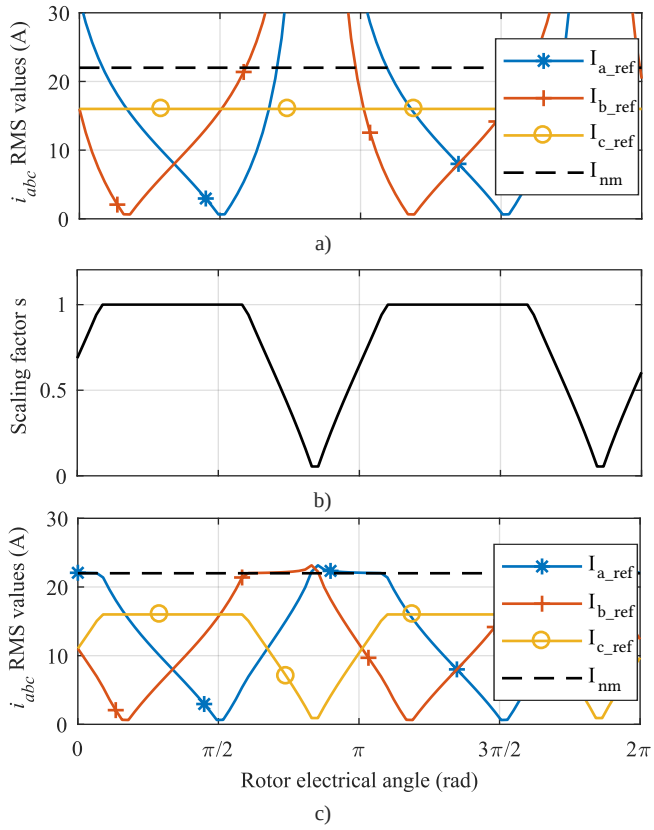

Figure 3.32: Scaling operation of the torque cancellation technique. (a) RMS values of the phase currents prior to scaling. (b) Scaling factor applied. (c) RMS values of the phase currents after scaling.

as

$$s = \begin{cases} 1 & 0 < I_{RMS\_max} < I_{nm} \\ \frac{I_{nm}}{I_{RMS\_max}} & I_{nm} \leq I_{RMS\_max}, \end{cases} \tag{3.33}$$

where $I_{RMS\_max} = \max(I_{a\_ref}, I_{b\_ref}, I_{c\_ref})$ and I_{nm} is the nominal current of the motor. This scaling factor is dependent of the electrical angle, since the reference currents for phase b anc a are, and is shown in Figure 3.32 b). Then,

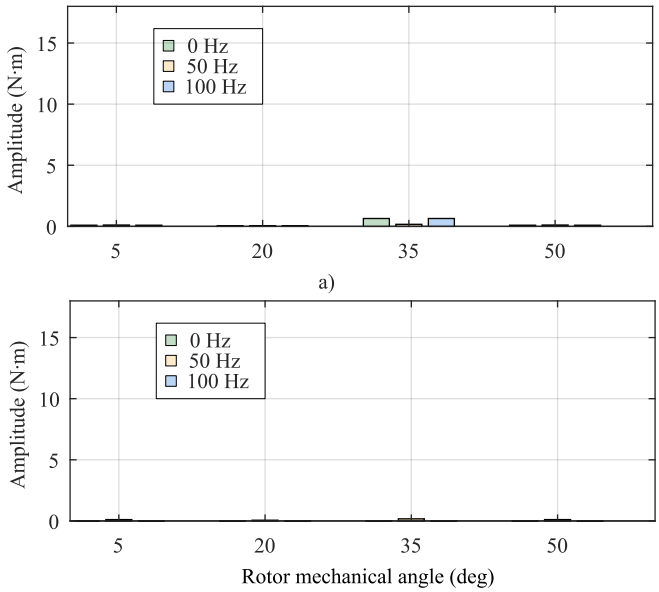

Figure 3.33: Torque components developed by the machine when the system is operating in charging mode and $i_q = 0$.

the scaled currents using the scaling factor are obtained simply by

$$i^*_{abc\_ref} = s \cdot i_{abc\_ref}. \tag{3.34}$$

This currents are depicted in Figure 3.32 c. When the angles for the maximum torque are being reached, the currents are scaled so the nominal current of the machine is not overcomed. For this simulation, $I_{nm} = 22$ A.

Using the scaling discussed, the same analysis to the torque components that was done in Figure 3.30 is repeated. The results are depicted in Figure 3.33, where it can be seen that the torque components for the angles considered is insignificant, even for the cases where the rotor was close to the highest torque generation points. Nevertheless, even if the torque is completely cancelled, from Figure 3.32 c) it can be seen that the charging current, which is the one flowing

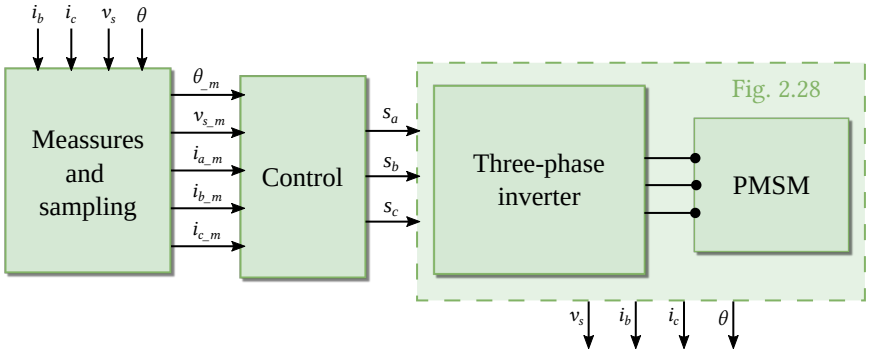

Figure 3.34: Simulation scheme employed for the integration of the machine in the charger

through phase C, is severely reduced due to the scaling. Since this current is used to charge the storage system, this effect will heavely impact on the charging power and thus, the charging speed.

3.3.3 Simulation results

In order to analyze the impact of the current scaling done in the previous section, a more complete simulation is done to study the viability of the machine's windings integration into the charger. To that aim, the two charging scenarios obtained form Figure 3.28 will be compared: the one where B1:ON and B2:ON and two phases of the motor are connected in parallel, using only two branches of the inverter; and the proposed where B1:OFF and B2:ON where the three branches are controlled for torque cancelling.

The simulation follows the scheme presented in Figure 3.34. The measures and sampling model uses the sample and hold already described in previous simulations, and the inverter and PMSM models use the Simulink powerlib library to recreate the connections showed in Figure 3.28. The control model takes the voltage measured and generates the charger current using the DSC control

strategy presented in Section 3.2.2.1. As it has been already discussed, this current is the same as the one flowing through phase C. Then, depending on the scenario considered, the other two reference currents are obtained differently:

- Parallel topology. The inverter is operated using a bipolar strategy and thus only one reference current is needed for generating the switching signals.
- Proposed three-phase topology. Using (3.30) and (3.32), the references for phases A and B are computed.

To generate the switching signals for the inverter, a bang-bang hysteresis controller is used. It obtains the switching signals as the result of the following boolean comparisons

$$\begin{aligned} s_c^+ &= (i_{c\_m} \leq i_{c\_ref}) \\ s_c^- &= \overline{s_c^+} \\ s_b^+ &= s_c^- \\ s_b^- &= s_c^+, \end{aligned} \tag{3.35}$$

for the case of the parallel topology. $s_a+, s_a- = 0$ since the third branch is not used. For the case of the proposed three phase topology, the are obtained as follows

$$\begin{aligned} s_c^+ &= (i_{c\_m} \leq i_{c\_ref}) \\ s_c^- &= \overline{s_c^+} \\ s_b^+ &= (i_{b\_m} \leq i_{b\_ref}) \\ s_b^- &= \overline{s_b^+} \\ s_a^+ &= (i_{a\_m} \leq i_{a\_ref}) \\ s_a^- &= \overline{s_a^+}. \end{aligned} \tag{3.36}$$

The simulation model described is used to simulate the currents and torque generated. The results are shown in Figure 3.35, for a charging current equal to $I_c = 16$ A, and the rotor electrical angle is 20 deg. The rest of the simulation

Table 3.12: Parameters of the simulation

Parameter	Description	Value
T_f	Simulation time step	10^{-6} s
T_s	Sampling time	5^{-5} s
V_{DC}	DC bus vltage	500 V
V_s	Grid voltage	230 V
V_D	Diode voltage drop	1.8 V
V_{EB}	Switch voltage drop	3.7 V
R_D	Diode resistance	32×10^{-3} Ω
R_{EB}	Switch resistance	76×10^{-3} Ω
E_{ON}	Switch ON energy	10.5×10^{-3} J
E_{OFF}	Switch OFF energy	7.5×10^{-3} J
E_D	Diode recuperation energy	3×10^{-3} J
V_{ref}	Reference voltage for losses calculation	1200 V
I_{ref}	Reference current for losses calculation	25 A

parameters are gathered in Table 3.12. Phases a and b are not controlled and the current flowing through phase c is shared between them following (3.24). It can be seen that, although greatly reduced compared with the parallel topology, the torque pulsations are not completely reduced as it was the case with the ideal current sources in Figure 3.33. This is due to the the limited performance of the hysteresis band to follow the references. Higher commutation frequencies could improve the results, but they are kept this way in order to better compare to the experimental results that will be presented in next section.

As it was stated before, the scaling of the currents in order to cancel the torque could potentially undercut the charging efficiency of the system. This is going to be analyzed taking into account that the efficiency of the charger is given by

$$\mu = 1 - \frac{P_J + P_{inv}}{P_u}, \tag{3.37}$$

where P_J are the joule losses of the three motor phases, P_{inv} are the losses of

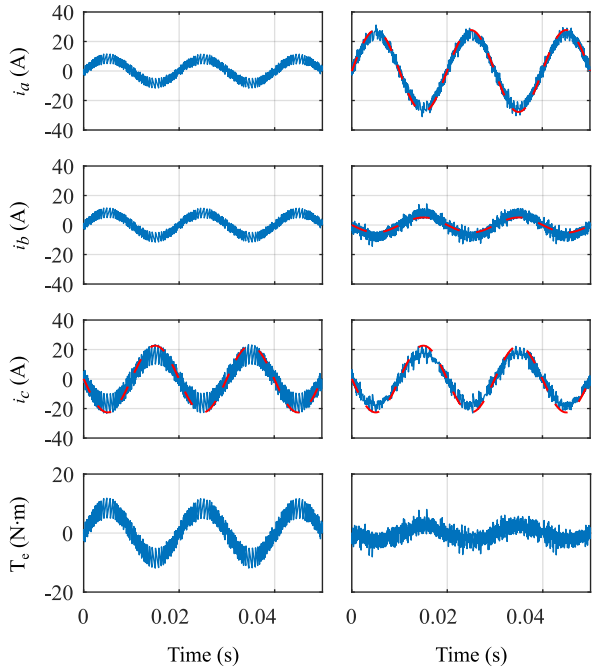

Figure 3.35: Simulation results comparing the parallel topology (left) versus the proposed one (right), for a rotor electrical angle $\theta_e = 20$ deg. The reference currents are represented by a dashed red line, while the currents flowing through the machine are depicted in solid blue, as the electromagnetic torque.

the inverter and P_u is the useful power demanded or injected to the grid. Since only the DSC strategy is used, the current in phase C (the one connected to the grid) is in phase with the grid voltage. Thus, $P_u = V_s I_c$. The joule losses in the machine windings are given by

$$P_J = I_a^2 R_s + I_b^2 R_s + I_c^2 R_s, \tag{3.38}$$

where R_s is the stator resistance per winding. Lastly, the inverter losses are calculated per branch, and are divided into conducting and switching losses as

$P_{inv} = P_{on} + P_{sw}$. The conducting losses for phase A are defined as

$$\begin{aligned} P_{on} &= P_{on\_EB} + P_{on\_D} \\ P_{on\_EB} &= V_{EB}\,|i_a| + R_{EB} i_a^2 \\ P_{on\_D} &= V_D\,|i_a| + R_D i_a^2. \end{aligned} \tag{3.39}$$

The losses are classified depending on the element they are produced on: the eletronic breaker (P_{on_EB}) or the reverse diode (P_{on_D}). V_{EB} and V_D are the voltage drops in these elements and R_{EB} and R_D their resistance. Lastly, the switching losses are defined as

$$\begin{aligned} P_{sw} &= P_{EB\_on} + P_{EB\_off} + P_D \\ P_{EB\_on} &= E_{on} \frac{|i_a|\,V_{DC}}{I_{ref} V_{ref}} f_s \\ P_{EB\_off} &= E_{off} \frac{|i_a|\,V_{DC}}{I_{ref} V_{ref}} f_s \\ P_D &= E_D \frac{|i_a|\,V_{DC}}{I_{ref} V_{ref}} f_s. \end{aligned} \tag{3.40}$$

Again, the switching losses are classified into losses when turning on the electronic breaker (P_{EB_on}), when turning it off (P_{EB_off}) and the power needed to polarize the reverse diode (P_D). E_{on} and E_{off} are the energy needed for turning on and off the switch, E_D is the energy for polarizing the diode. All these parameters are given by the manufacturer for certain operating conditions marked by I_{ref} and V_{ref}. They are extrapolated to the working point of the converter given by the phase current i_a, the DC bus voltage V_{DC} and the switching frequency f_s.

With the power definitions made, a simulation for computing all the terms mentioned is conducted, comparing the parallel topology with the proposed three-phase one. The same charging conditions used in previous simulations are kept,i.e., $I_c = 16$ A, and the simulation is repeated for a complete electrical revolution of the rotor, measuring the maximum torque developed, the useful power, the losses and efficiency of the system. Also, for the three-phase topology, scaling is done when needed. The results are depicted in Figure 3.36. From

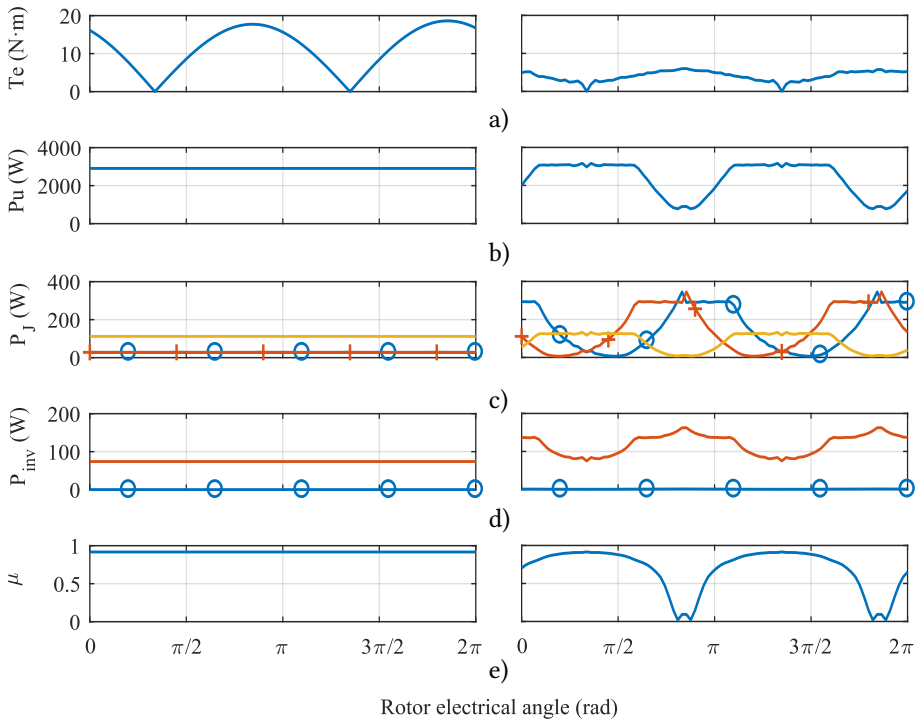

Figure 3.36: Simulation results comparing the paralallel topology (left) with the proposed one (right), for a complete rotor electrical revolution. a) Torque developed by the machine. b) Useful power. c) Machine losses for phase A (blue line with circle markers), phase B (orange line with cross markers) and phase C (solid yellow line). d) Inverter switching losses (blue line with circle markers) and conduction losses (orange solid line). e) Charging efficiency.

Figure 3.36 a), it can be clearly seen how the torque is greatly reduced in the proposed topology no matter the rotor position. However, the useful power is affected by the current scaling when the rotor get to the worse operation points given in (3.28), as it can be seen in Figure 3.36 b). The joule losses for phases a and b, shown in Figure 3.36 c), were almost negligible in the case of the parallel topology, but increase specially when the current needed in those phases grow due to high torque generated by the motor. The same can be said for the inverter

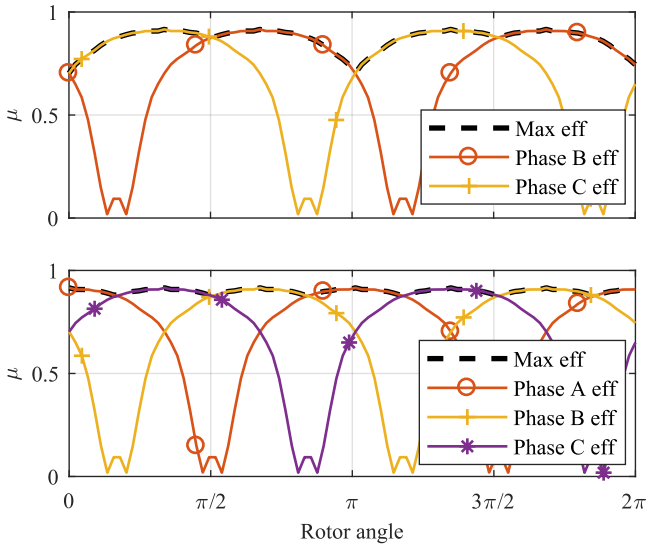

Figure 3.37: Simulation results showing the efficiency of each branch and the maximum combined efficiency achieved. The top plot shows the efficiency combined when using two branches and the bottom one, when using three branches.

losses shown in Figure 3.36 d), the conduction losses are increased due to the intensive use of the remaining phases not connected to the grid, while the switching losses are barely changed. The overall efficiency is depicted in Figure 3.36 e), and it can be seen that, as expected, the efficiency is severely reduced due to the scaling.

It can be observed from Figure 3.36 e) that, for the angles where the maximum torque is produced, the efficiency has margin for improvement. As it was stated previously, it is imperative that the system has to be able to charge no matter the rotor angle. However, if the voltage source is connected in any of the other two phases, the efficiency curve is shifted $2\pi/3$ electrical radians. In this way, the points of minimum efficiency can be avoided while retaining the advantage of reducing the torque generated by the machine. The efficiency could be further

improved by allowing the connection to the single phase grid in any of the three branches, which would allow an efficiency curve almost flat and equal to the parallel topology. This situation is illustrated in Figure 3.37, for a complete electrical revolution of the rotor. The efficiency ranges from $[0.70, 0.91]$ for the case that the grid is connected to the best out of two phases (c or b) , and from $[0.88, 0.91]$ for the case that the grid is connected to the most favorable phase voltage.

3.3.4 Experimental results

In order to validate the proposed integrated topology for the charger, a prototype has been built. The machine windings have been used for replacing the AC inductor. The whole prototype can be seen in Figure 3.38. It is formed of the following elements:

- dSPACE control platform. The MicrolabBox control platform from dSPACE was used to measure all the variables, as well as generating the switching signals for the converters used.

- Host PC. Running the software ControlDesk, is used to visualize variables and record them, for later processing and plotting.

- Oscilloscope. Used for capturing some snapshots of the main system waveforms.

- Three-phase inverter. The same inverter used for driving the motor is now used for the charging process.

- Magnetic dust brake. Its mission is esentially lock the rotor to avoid the spinning of the motor and allow torque measurement.

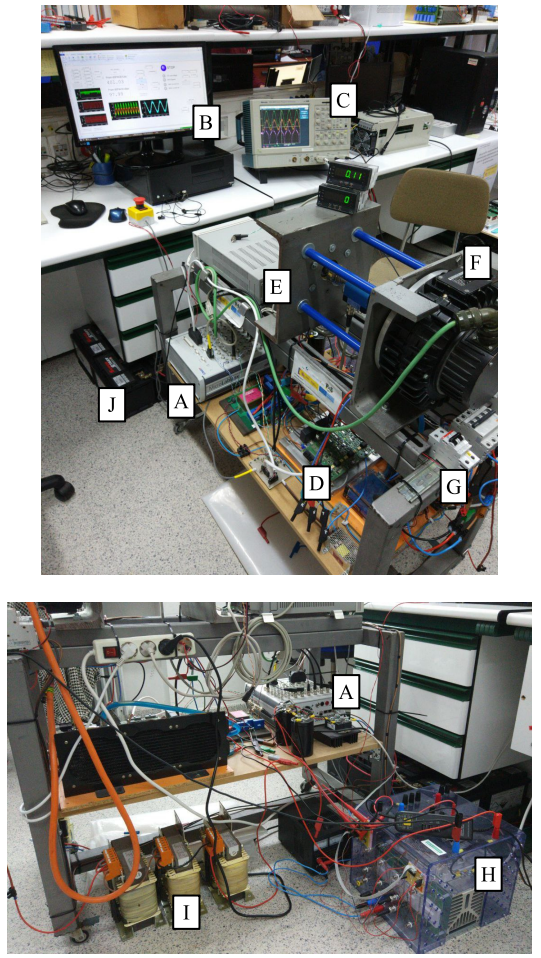

Figure 3.38: Experimental testbench for the conducted experiments. A: dSPACE control platform. B: ControlDesk software. C: Oscilloscope. D: three-phase inverter. E: Magnetic dust brake. F: PMSM. G: Single-phase grid conection. H: DC/DC converter. I: DC filter. J: Energy storage

- Single grid connection. The connection to the grid is made using banana connectors to allow easy reconfiguration between parallel and three phase

Table 3.13: Parameters of the experiments

Parameter	Description	Value
T_s	Sampling time	5^{-5} s
V_{DC}	DC bus vltage	500 V
V_s	Grid voltage	230 V
V_{bat}	Battery voltage	96 V
R_{bat}	Battery inductive filter resistance	0.38 Ω
L_{bat}	Battery inductive filter inductance	6×10^{-3} H
I_{ch}	RMS value for charger reference current	16 A

topologies.

- Measuring board. Voltage (LV50) and current (LA25) transducers are employed to transform the electrical signals so they have an amplitude measurable by the control platform.

- DC/DC converter. One branch of the extra converter is used to build the DC/DC converter used to regulate the DC bus voltage.

- Energy storage. Eight lead acid 12V batteries connected in series are used to build the storage system for the prototype.

Most of the equipment used has already been described in Section2.3. The inverter used for driving the motor is employed for AC/DC conversion from the grid, while an extra branch from the second converter is used for the DC/DC conversion. The DC/DC converter has an inductor L_{DC}, while the motor windings are used for the AC/DC converter. The main parameters for the experiments are gathered in Table 3.13.

The first test results, representing the paralellel topology, is depicted in Figure 3.39. Three different rotor positions are represented, and for each one the grid voltage v_s, current i_s and torque measured in the shaft of the machine. In the

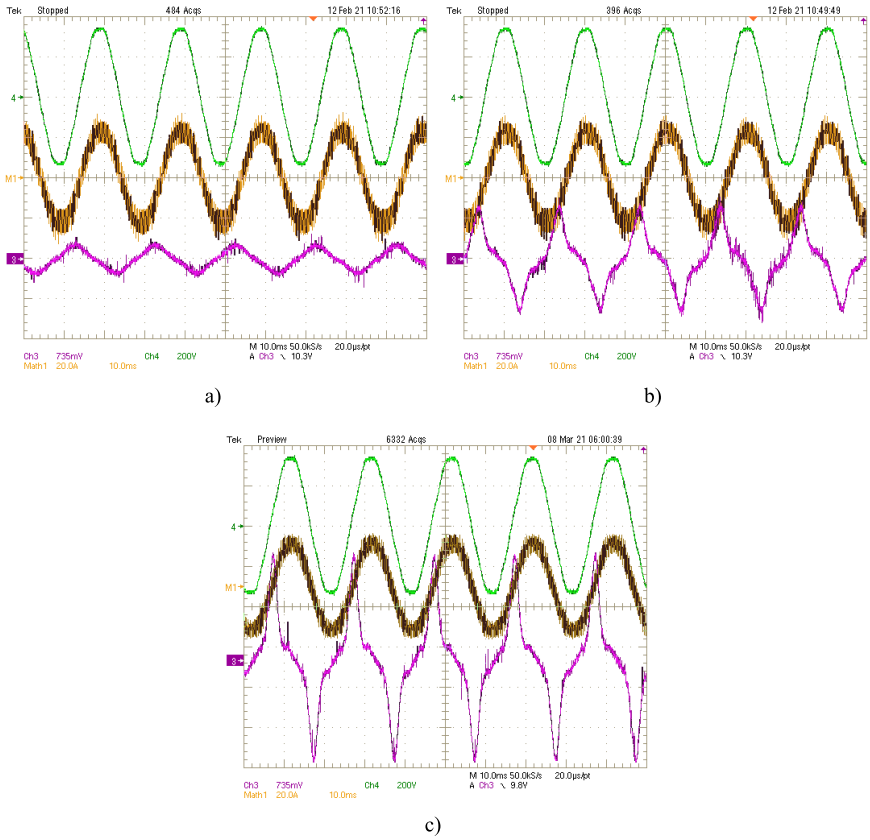

Figure 3.39: Experiments results for the paralell topology. Three different rotor positions: a) $\theta = 1.02$ rad, b) $\theta = 1.4$ rad, c) $\theta = 2.6$ rad. From top to bottom: grid voltage v_s (200 V/div), grid current i_s (20 A/div) and torque (10 Nm/div).

three experiments conducted, the grid current RMS value is fixed at 16 A since it is an usual value for domestic consumers. This current is kept in phase with the grid voltage in order to achieve unity power factor. It can be observed that, the closer one gets to angle values of maximum torque, torque peaks around 20 Nm can be observed. This would severely affect mechanical elements connected to the shaft of the machine.

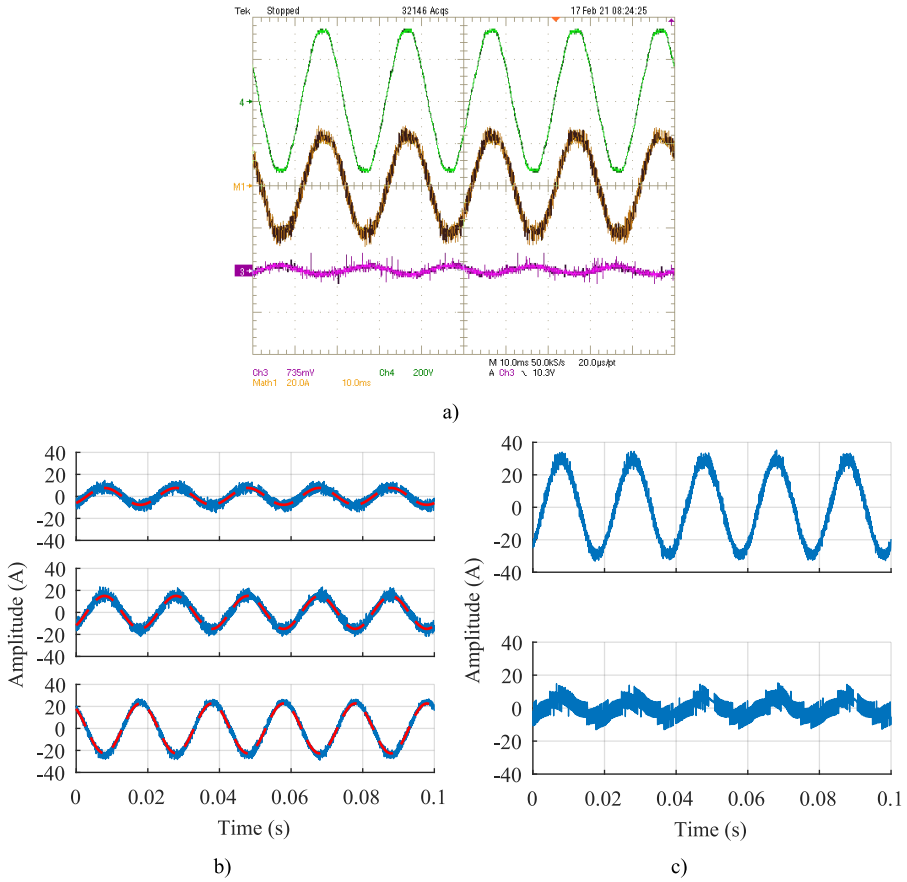

Figure 3.40: Experiment results using the three phase topology, with the torque cancellation strategy for $\theta_e = 1.02$ rad. a) grid voltage v_s (200 V/div), charger current i_{ch} (20 A/div) and torque (10 Nm/div), from top to bottom. b) Motor currents i_{abc} as measured by the control platform (reference current as a dashed red line, scaled refence in green with circle markers and measured current in solid blue). c) Motor currents in the $dq0$ reference frame (d current top, q current bottom).

Next, the same experiments are conducted using the strategy proposed, and its results presented in Figure 3.40, Figure 3.41 and Figure 3.42 where each figure corresponds to a different rotor position, the positions analyzed in Figure 3.39.

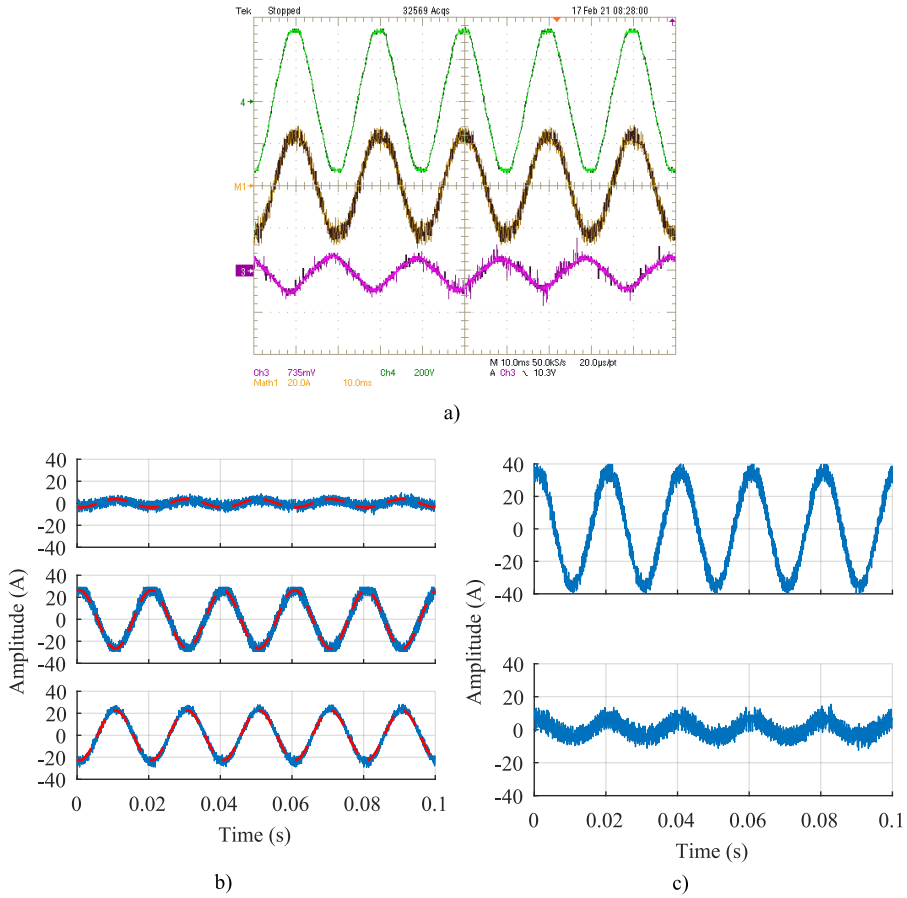

Figure 3.41: Experiment results using the three phase topology, with the torque cancellation strategy for $\theta_e = 1.4$ rad. a) grid voltage v_s (200 V/div), charger current i_{ch} (20 A/div) and torque (10 Nm/div), from top to bottom. b) Motor currents i_{abc} as measured by the control platform (reference current as a dashed red line, scaled refence in green with circle markers and measured current in solid blue). c) Motor currents in the $dq0$ reference frame (d current top, q current bottom).

The current level for I_{ch} is kept at 16 A, and the reference currents i_{a_ref}, i_{b_ref} and i_{c_ref} are calculated according to (3.30), (3.29) and (3.32) respectively. The

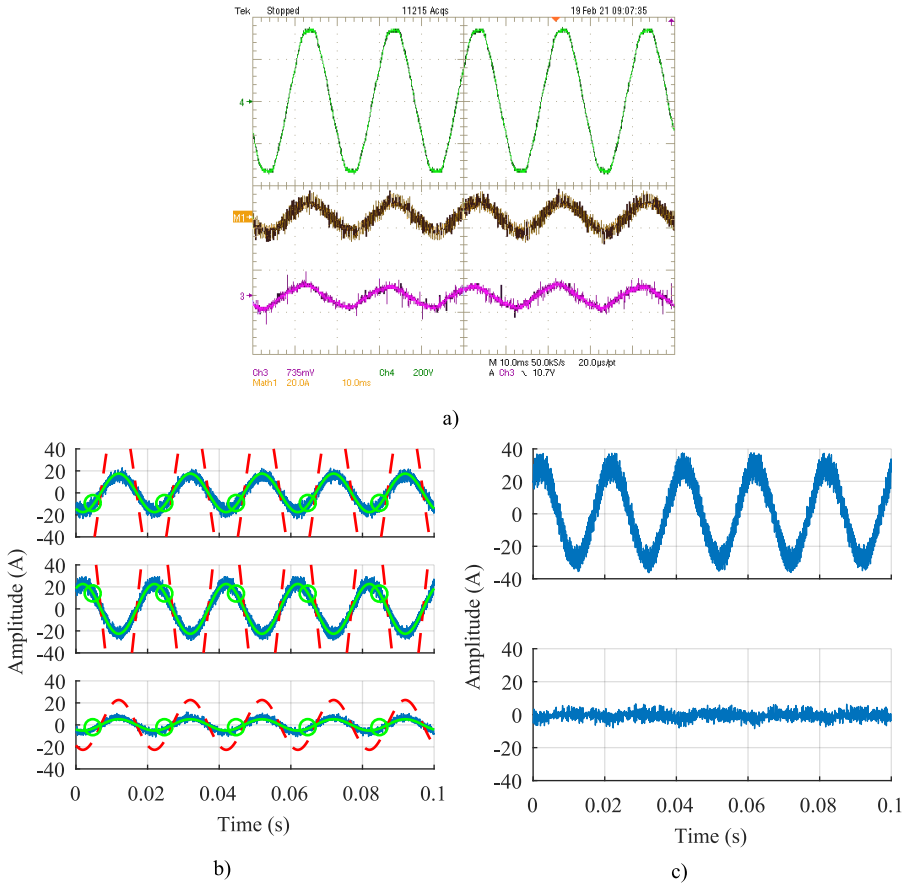

Figure 3.42: Experiment results using the three phase topology, with the torque cancellation strategy for $\theta_e = 2.6$ rad. a) grid voltage v_s (200 V/div), charger current i_{ch} (20 A/div) and torque (10 Nm/div), from top to bottom. b) Motor currents i_{abc} as measured by the control platform (reference current as a dashed red line, scaled refence in green with circle markers and measured current in solid blue). c) Motor currents in the $dq0$ reference frame (d current top, q current bottom).

subplots labeled with a) show the oscilloscope captures depicting the same information as Figure 3.39, where it can be seen that the currents are kept in phase

with the grid voltage as before. From Figure 3.42 a), it can be seen that the current magnitude for the grid current is much smaller than in the other two cases. This is because in this rotor position, the other two currents needed for torque cancellation are so high that require scaling, and so does the grid current. In any case, it can be seen how the torque peaks are severely reduced. However, there is still some torque developed as discussed for in the simulations results depicted in Figure 3.36, the main reason being the hysteresis current controller. In the subplots marked with b), one can see the reference currents in the *abc* reference frame, the scaled references when scaling is used, and the phase currents measured by the control platform. Again, for the third rotor position, the reference currents exceed the maximum currents allowed, and thus they are scaled down in order to guarantee that the nominal currents are not overcomed and still generate the minimum torque possible in the rotor shaft (Figure 3.42 b)). Lastly, the measured currents in the *dq* reference frame are depicted in the right column. Here it can be seen that there is still some current in the q axis, again due to the current controller perfomance. It is worth noting that the strategy proposed can be implemented with any other current controller, so there is no lack of generality.

3.4 Conclussions

The control and management of an ESS has been developed in this chapter. Three control strategies, regarding the power flow and harmonic control, have been developed and tested in simulation and expriments. Next, the integration of the charger developed into the drive system of an EV is studied, analyzing the torque generated during the charge stage. A new control strategy and topology is developed to miminize the torque pulsation generated when the motor windings

are used as inductors for the converter. The following can be concluded from this work

1. The ESMS is able to control the energy flow demanded form the ESS even with distorted grid voltage. However, provide the exact power references is a difficult task because of numerous experimental factors, specially in the signal acquisition process and the exact knowledge of system parameters. Nevertheless, the prototype built is able to fulfill the power requiremets with small percentage error.

2. Besides controlling active and reactive power, the ESMS is able to minimize the effects caused by the harmonic current demanded by a non-lineal load. The bandwith of the controller plays a fundamental role in the charger's ability to cancel the harmonic content. The deadbeat controller has found to be too dependent on system parameters and its hability to follow high frequency reference currents, limited. Nevertheless, the charger is able to supress most of the harmonic content of the grid current, to the extent of its available current limits.

3. The ESS storage system is sucessfully hybridated using both supercapacitor and battery storage. The active power reference is splitted, taking advantage of the high power density of the supercapacitor for taking the steep power references. This fact allows to smooth the requirements, improving its lifetime.

4. The integration of the motor drive is difficult, specially if both ends of the windings are not accessible. Moreover, the torque generated has a DC component that will try to move the rotor in certain positions. The torque control strategy developed allows to use more components of the drive sys-

tem for a better torque suppression. The efficiency can be maintained if the grid connection is switched to the more convenient motor phase.

4

Active Damping

4.1 Introduction

Vibrations are a consequence of the functioning of a machine, and it does not always mean an abnormal mode of operation. In the case of electric drives, where there is an electrical rotating machine, the source of the vibration can be electrical or mechanical. The so called Noise, Vibration and Harshness (NVH) studies aim to identify those sources in order to understand them and propose solutions [89–92].

The gradual change towards the EV supposes a new challenge for NVH techniques, since the vibration sources in a traditional vehicle, equipped with an Internal Combustion Engine (ICE), are mainly mechanical. In the case of EVs, power electronics and the vehicle control are in part responsible for the noise in the current and voltages, which in turn accounts for the vibration. Moreover, the electric motor can also be a source of vibrations due to its torque response [93].

The electrification of the power train (i.e. the propulsion and transmission systems) is yet another problem that the NVH analysis techniques have to deal with. In ICE equipped vehicles, there are several elements that act as mechanical

dampers suppressing the vibrations in the power train, such as the clutch, flying wheel and flexible joints. However, in most EVs these elements are removed because of the change in the propulsion system, weight and cost reasons. The increase in speed range of the electric drives, together with the mass reduction of the system favors the displacement of the system resonances to lower motor rotation speeds [94].

Despite the problems that the change towards the EV brings in terms of new sources of vibrations, the presence of power electronics and the electrical motor brings a new possibility of tackling this issue. Compared to the traditional solutions for passive vibration attenuation, the aforementioned new components can be used to provide an active solution that can be used to adapt to any situation, the so called active damping [95].

In the vehicle field there is a great interest in correcting the vibrations since they heavily affect the driving experience. In [96] the authors develop a complete vehicle model, taking into account the suspension actuators to develop a robust control against parameter uncertainties. Other researchers include data from the road ahead of the vehicle to better adapt and anticipate a good response [97].

However, the active damping is not only applicable to the EV field, but rather to any field with vibrations associated with rotative electrical machines. This includes the industrial and even domestic fields. [98] is a clear example, which describes the detection and attenuation of vibrations caused by high speed rotation under unbalanced loads in a washer. On the industrial field, [99] studies the effect of vibrations and their active damping on a moving strip system under external time-varying disturbances.

4.1.1 Challenges encountered

The cancellation of the speed oscillations causing vibrations in an EV has been topic of research for the past years. The goal of supressing the vibrations coming

from the electrical motor has motivated the research in advanced speed controllers. The authors in [100] analyzed the effect of the PI controller tuning, adding feedback from the system to it. More advanced controllers are also investigated for this topic, such as the artificial intelligence based controls [101], linear quadratic regulators [102] and H∞ control [103]. However, even if the vibrations originated in the propulsion system are addressed, the resonance issues caused by the interaction with the power train are still present.

On the mechanical part, the damper coefficient, stiffness and mass of the system are critical to tackle the resonance issues. Active suspension [104] and other suspension mechanisms based on extra elements and actuators [96, 97] have been investigated. Nevertheless, mass, volume and cost are constraints that must be taken into consideration in EV applicatins [94].

Fortunately, the use of an electric motor in the EV can be employed as an actuator that is already present in the system for vibration suppression. Aided with the rest of sensors used for the FOC described in previous chapters and the information provided by a NVH analysis of the vibrations on the system, an active damping of the vibrations observed in a structure can be carried out without the need of extra equipment.

4.1.2 Goals of the reserch

This chapter has two goals in mind. First, an experimental NVH study will be carried out to analyze the vibrations present in the testbench already used in Section 2.3. The experimental data will then be processed in the frequency domain using Fourier analysis. This will allow to model the vibrations observed, aiming to reproduce in simulation the conditions of the experiment.

The second objective is to use the results from the system modelling to develop an active damping control able to attenuate the vibrations encountered. First, the role of the speed controller will be analyzed with respect to vibration cancellation.

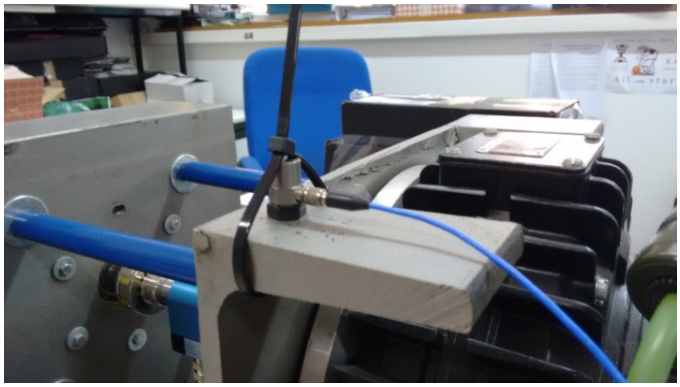

a)

b)

c)

Figure 4.1: Accelerometer setup used of the vibration acquisition. a) Location of the accelerometer. b) accelerometer used. c) Signal processing device.

Then, the active attenuation technique will be described and the automation of such algorithm will be discussed. Simulation results will confirm the usefulness of the control developed.

4.2 Vibrations in structure with rotative elements

In order to determine the vibrations expected in a system attached to an electric motor, a NVH experimental study consisting on some experiments will be

carried out. The experiments will use the testbench described in Section 2.3, using the FOC to drive the motor. For determining the vibrations in the structure, an accelerometer will be attached to the testbench, as shown in Figure 4.1. It also includes a signal conditioner for processing the signal meassured, prior to representation. The signal is then recorded using the oscilloscope for later processing.

One example of the data collected by the oscilloscope can be seen in Figure 4.2. The signals shows the vibration data, represented by Γ, as a function of time. The signal conditioner removes the DC offset of the waveform, so only the periodic content remains, as it can be seen in Figure 4.2 b), where the frequency spectrum of the signal acquired is depicted. Since the sampling frequency used in this example is 2.5 kHz (2.5 kS/s), the Fourier analysis only shows the components up to 1250 Hz.

Given that one is interested in studying the relationship between the rotor speed and the vibrations observed, the focus has to be set in the low frequency region of the frequency spectrum. From Figure 4.2 b) it can be seen how there are important peaks located at the lower frequency content. If the experiment is repeated, lowering the sampling rate to 500 S/s, and varying the rotor speed, the results are the ones shown in Figure 4.3. The speed reference for both cases depicted in Figure 4.3 are 300 and 500 rpm, respectively. The relationship between the frequency and rotation speed of the synchronous machine is

$$n = \frac{60 f_\omega}{p}, \tag{4.1}$$

where n is the rotor speed in rpm and f_ω is the electric rotation frequency in hertzs. From the speed references given, and knowing that the machine has 4 pole pairs (Table 2.3), the corresponding electric rotation frequencies for Figure 4.3 would be 20 and 33.33 Hz, respectively. From this figure it is clear that the vi-

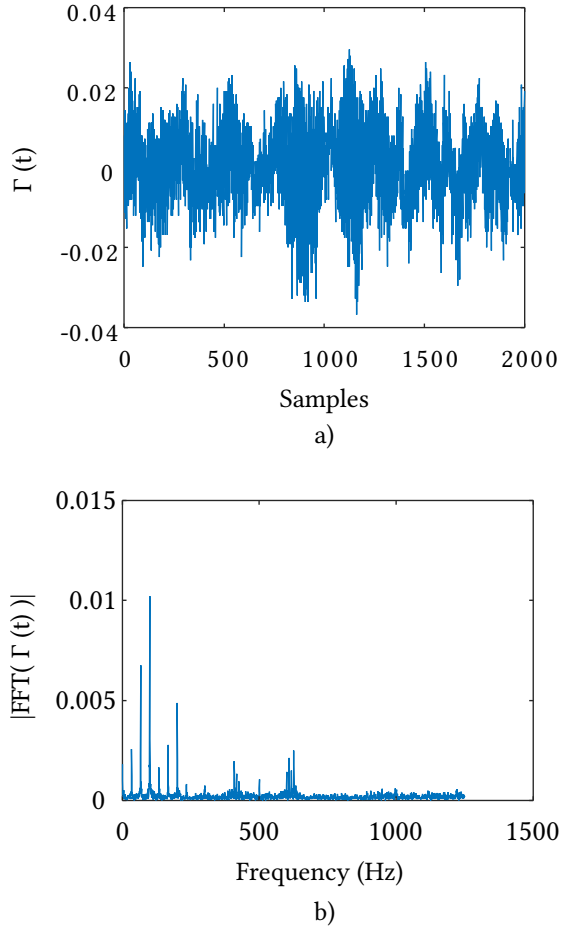

Figure 4.2: Data collected from the accelerometer. Sampling rate 2 kS/s. a) Vibration data from acelerometer. b) Frequency spectrum of the vibration signal.

brations recorded by the accelerometer are distributed along the main harmonics of the electric rotation frequency.

Finally, in the last experiment, more rotor speeds are tested and also a load is applied to the motor. The reason is to determine whether the load affects the location and amplitude of the vibration harmonics or not. The harmonic frequency

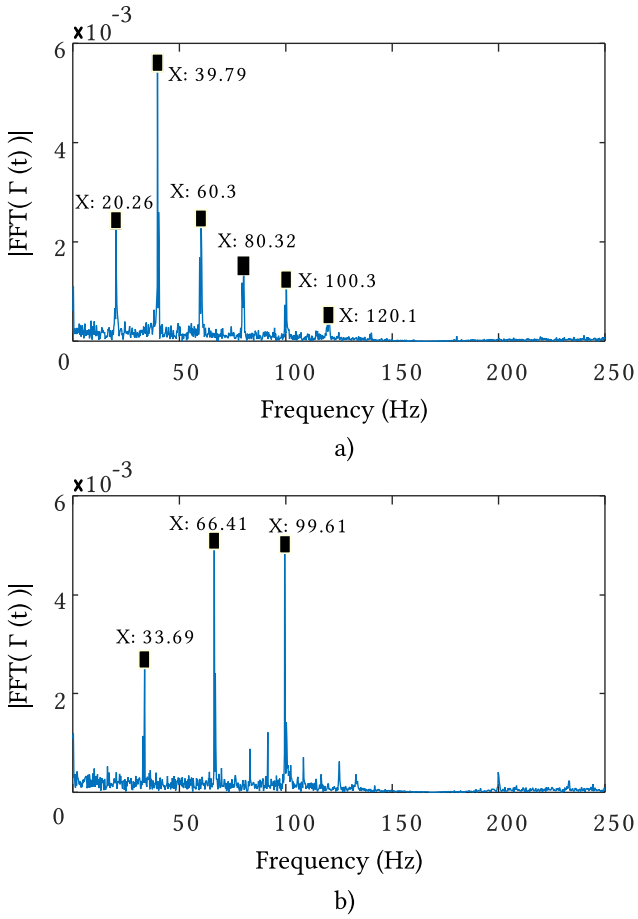

Figure 4.3: Harmonic distribution according to speed. a) Rotor speed: 300 rpm. b) Rotor speed: 500 rpm

locations are gathered in Table 4.1 and depicted in Figure 4.4. As predicted, the harmonic components are located at multiples of the electric rotation frequency f_ω, and applying load to the machine barely changes this fact. On the other hand, the amplitude of the harmonic content seems to be modified by the load condition, as can be observed in Figure 4.4. In any case, it can be concluded that

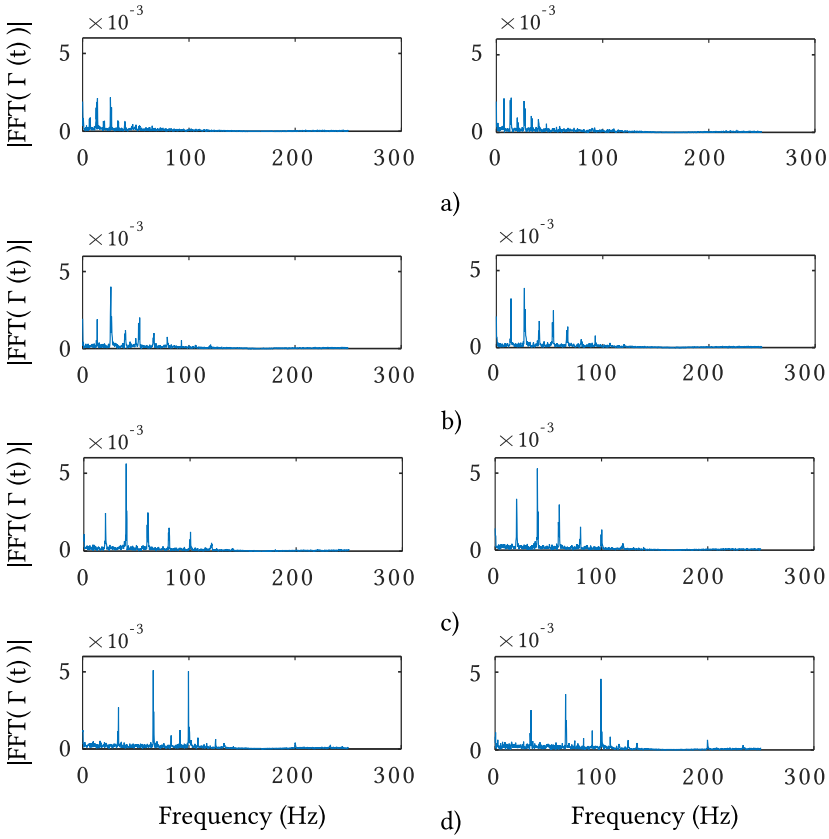

Figure 4.4: Harmonic distribution according to speed. Column in the left results with no load, right ones have 4.3 Nm torque applied a) Rotor speed: 100 rpm. b) Rotor speed: 200 rpm. c) Rotor speed: 300 rpm. d) Rotor speed: 500 rpm

the vibrations observed can be described as a function of the electric rotation frequency as

$$\Gamma(f_\omega) = \sum_{h=1}^{n} \Gamma_h \sin\left(2\pi f_\omega h + \phi_{h\Gamma}\right), \tag{4.2}$$

where $\phi_{h\Gamma}$ would be the phase of the harmonic component h of the vibration. This will be used for the simulation of a vibration model in order to develop an attenuation procedure, as will be discussed in the following section.

Motor Speed	Load Condition	Main harmonic content frequency				
		1st	2nd	3rd	4th	5th
100 rpm	No load	6.348	13.92	20.51	26.12	32.96
	Loaded	7.08	13.92	19.53	26.12	32.96
200 rpm	No load	13.67	26.37	40.28	53.71	67.14
	Loaded	13.67	26.37	40.28	53.71	67.14
300 rpm	No load	20.26	39.79	60.3	80.32	100.3
	Loaded	20.26	39.79	60.3	80.32	100.3
500 rpm	No load	33.69	66.41	99.61	-	-
	Loaded	33.69	66.41	99.61	-	-

Table 4.1: Location of the main harmonics depicted in the results from Figure 4.4

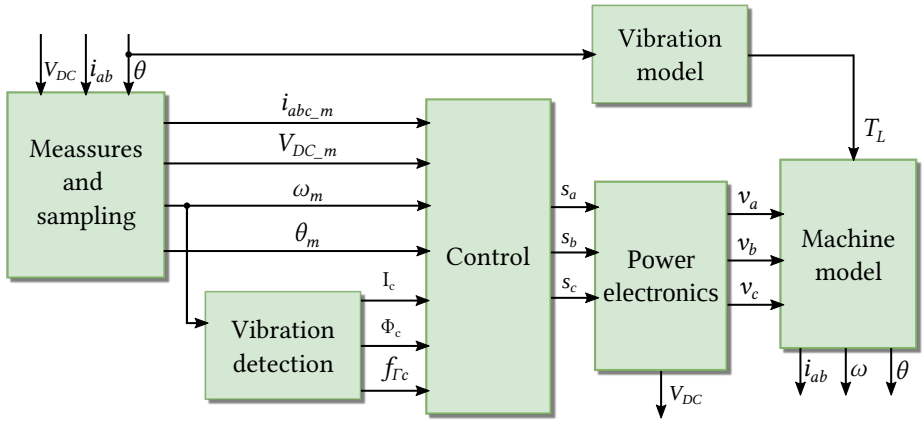

Figure 4.5: Simulation scheme for vibration control

4.3 Vibration attenuation

As it has been deduced from the previous section, a structure coupled to a motor will have vibrations that will depend on the rotation speed. In order to mitigate these vibrations, two different methods will be investigated. The first one is using the already present PI speed controller in the system, by modifying the controller constant and studying the effect on the system. Since it does not adapt to the

Component	Amplitude (Nm)
T_{L_0}	4
T_{L_4}	0.4
T_{L_8}	1.6
T_{L_12}	0.2

Table 4.2: Load torque components used for the simulation model

characteristics of the system's vibrations, it is also referred as passive attenuation. The second one will make use of the information available about the vibration to introduce corrections in the current controller, thus it is called active attenuation.

For developing an attenuation method for the vibrations observed, first a simulation model will be put together. The model is based on the one already described in Section 2.2, and is depicted in Figure 4.5. Based on the observations made in the previous section, the vibrations introduced in the model will be a function of the rotor speed. They will be simulated as perturbations in the load torque, so they appear in the rotor speed and angle later on. Therefore, taking as a reference (4.2), the load torque for the vibration model can be expressed as

$$T_L(\theta) = \sum_{h=0}^{n} T_{L\_h} \sin(h\theta), \tag{4.3}$$

where the index 0 would refer to the DC component of the load torque. Recalling (2.8), it is clear that the same amplitude in different load torque components will translate into different amplitudes for the same harmonics in the speed. This is due to the low pass filtering effect that the rotor inertia exert on the system.

The load torque modelling introduced produces speed oscillations that would translate later on into vibrations. The load torque composition described by Table 4.2 produces the oscillations in the rotor speed shown by Figure 4.6.

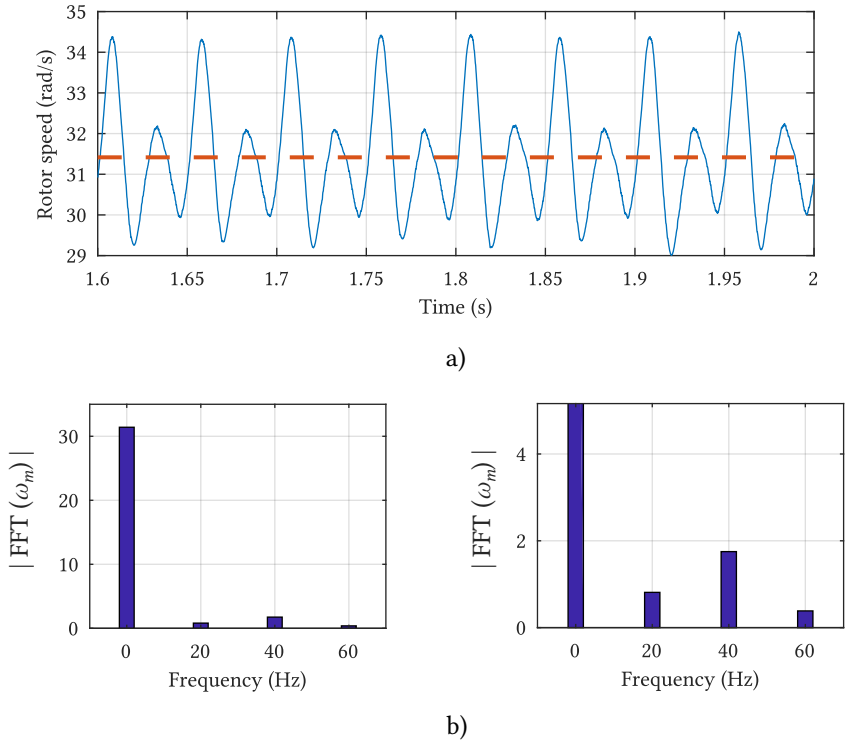

Figure 4.6: Speed vibrations introduced using the vibration model. Speed reference of 300 rpm or 31.41 rad/s (mechanical speed) a) Speed waveform. b) Speed Fourier analysis (whole plot on the left, zoomed part of the vibration components on the right)

4.3.1 Passive attenuation

As it was previously stated, one option to cancel the oscillations observed in the rotor speed that are causing the vibrations would be to use the existing speed controller of the motor. Since the mission of this controller is to set the rotor speed to the reference given, it can be used to correct the oscillations observed. The speed controller used is the PI described in Section 2.2.3.1, now depicted as a block diagram in Figure 4.7. To the controller already described, a derivative

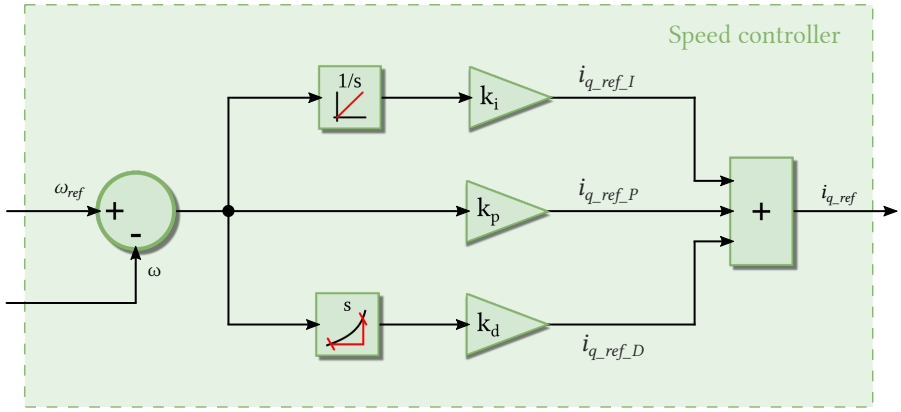

Figure 4.7: Block diagram of the speed controller based on PID

part has been added for this study, so the controller is now a Proportional Integral Derivative (PID) controller.

Each part of the controller is in charge of adding to the current reference i_{q_ref} its own share, based on the error committed. Thus, the current reference can be expressed as

$$i_{q\_ref} = i_{q\_ref\_P} + i_{q\_ref\_I} + i_{q\_ref\_D}, \tag{4.4}$$

where the subindex P,I and D indicates the controller part which generates it. Figure 4.8, presents an example of this fact, when the rotor is spinning at 300 rpm, the controller constants are $k_p = 0.3, k_i = 1.5, k_d = 0.005$ and the torque load components are $T_{L\_0} = 4, T_{L\_8} = 1.6$ Nm. The speed oscillation is then located at 40 Hz (8 times the mechanical frequency of rotation) and is present in the error feeded to the controller, $\omega_{ref} - \omega_m$.

Due to nature of each controller's part, the reference they supply has different charasteristics. The proportional part is just a scaled version of the error in the speed, so it is in phase with it. However, this is not the case for the other two, due to the integration and derivative done to the error prior to the multiplication by the corresponding gains. When the steady state is reached, the integral operation

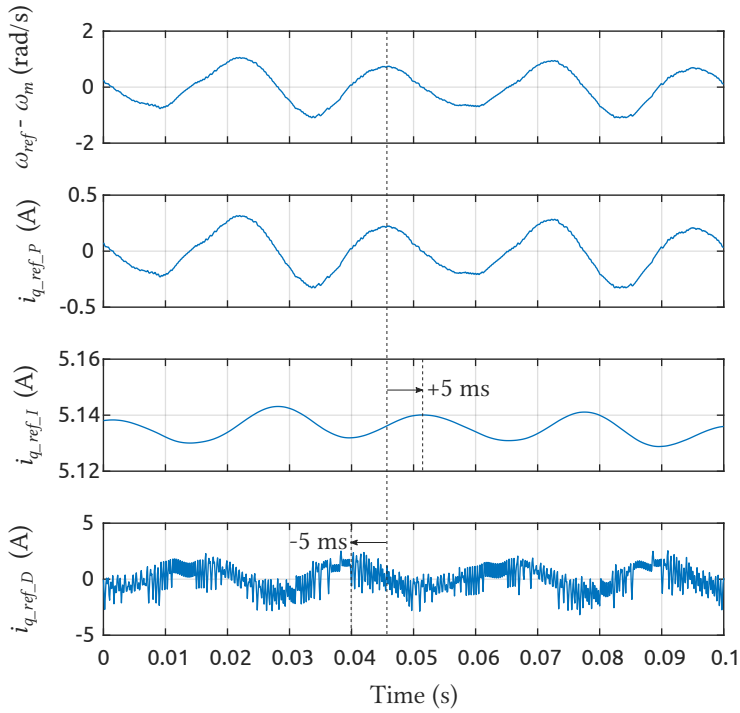

Figure 4.8: Reference share of each part of the PID controller. From top to bottom: error fed to the controller, proportional reference, integral reference and derivative reference.

shifts the phase of the error by 90 degrees lagging behind. This can be observed in Figure 4.8, where a vertical line as been added at one maximum of the speed oscillation. Recalling that the oscillation has a frequency of 40 Hz, it is clear that the period is 0.025 s. It can be observed in the figure how the integral share of the controller is lagging 90 degrees (corresponding to 0.005 s), while the derivative contribution is leading the error by the same amount. The final reference is the sum of the three waveforms, having a phase that will depend on the amplitudes of each part, i.e., the gains of the controller.

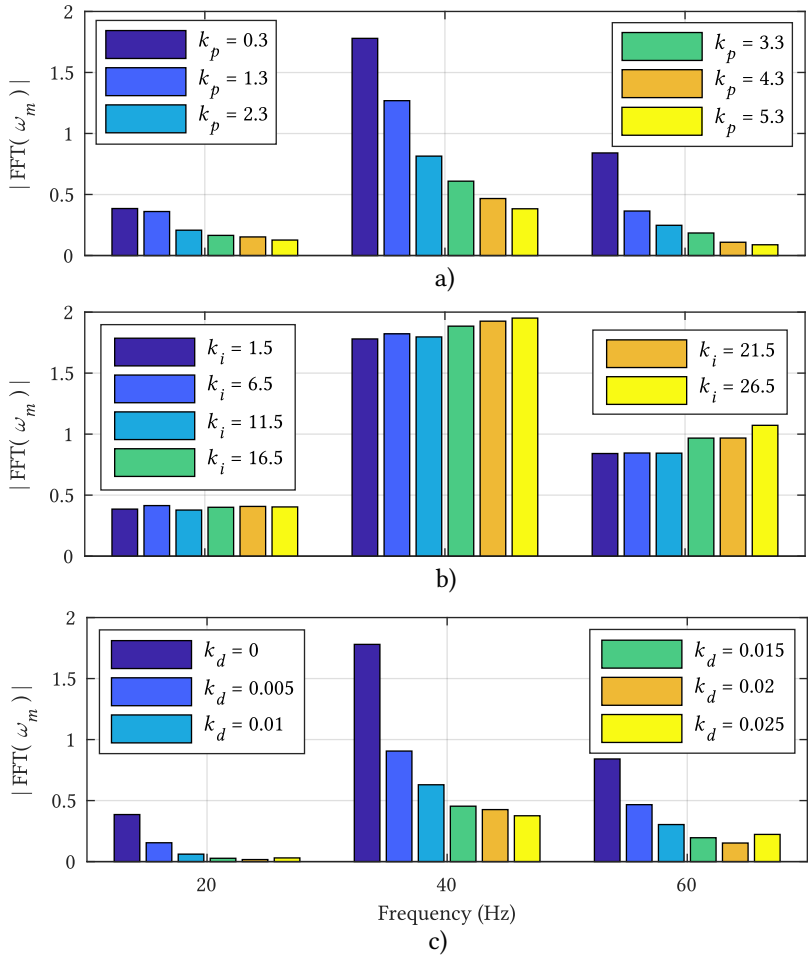

Figure 4.9: Simulation results of passive attenuation by PID tuning. a) Harmonic amplitudes when tuning the proportional controller. b) Harmonic amplitudes when tuning the integral controller. c) Harmonic amplitudes when tuning the derivative controller.

In order to test the capability of the PID controller to eliminate the speed oscillations and the vibrations that would arise from them, a more complete simulation is conducted. The load components are the ones from Table 4.2, while

the rotor speed is fixed at 300 rpm. The values for the each gain of the speed controller are selected from the following ranges $k_p = [0.3, 1.3, 2.3, 3.3, 4.3, 5.3]$, $k_i = [1.5, 6.5, 11.5, 16.5, 21.5, 26.5]$, $k_d = [0, 0.005, 0.01, 0, 015, 0.02, 0.025]$. The results are shown in Figure 4.9, and the changes done to each gain are done one at a time. The initial values for each gain are the first values of each set, so when the proportional gain is being swetp in Figure 4.9 a), $k_i = 1.5$ and $k_d = 0$ for all k_p values. The figure represents the amplitude of the speed harmonic components at 20, 40 and 60 Hz. It can be observed how the main contributors to the oscillation cancelation are the proportional and the derivative part. The integral part is in charge of the steady state error elimination, and the speed oscillations are too fast for the integrated error to make any difference.

From these results, it is clear that a combination of the proportional and derivative control could almost eliminate the oscillations introduced in the speed. However, the PID tuning is normally adjusted to obtain a desired behaviour of the machine (rise time, overshoot, settling time) and tuning the controller to also remove the oscillations could compromise this aspect of the control. Moreover, the derivative part of the controller can introduce noise to the current reference, since the derivation of the signal can suffer from a faulty meassurement in the rotor speed (see the last plot from Figure 4.8). Therefore, it would be interesting to develop a different control scheme that introduces the needed correction aside to cancel the oscillations leaving aside the speed controller.

4.3.2 Active attenuation

Understanding the vibrations observed and taking advantage of its charasteristics can be used to develop an alternative control to cancel de speed oscillations. As it was checked in the previous section, adding to the constant q-axis current reference (the one needed to overcome the constant load T_{L_0} and maintain the

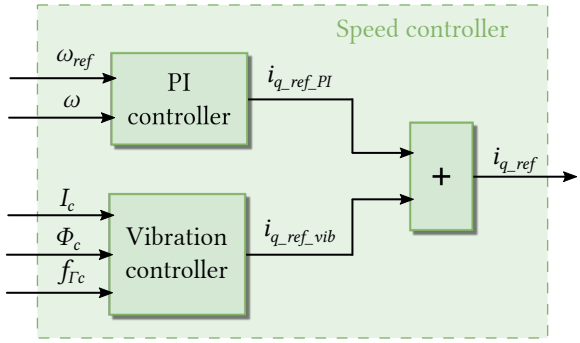

Figure 4.10: Block diagram of the speed controller including an active cancellation of oscillations.

speed reference) an additional waveform with the same frequency as the oscillation observed, but different phase and/or amplitude, could potentially eliminate said oscillation. Such control is the one depicted in Figure 4.10, from which can be easily deduced that

$$i_{q\_ref} = i_{q\_ref\_PI} + i_{q\_ref\_vib}, \tag{4.5}$$

where $i_{q\_ref\_PI}$ is the PI contribution for the q-axis current reference, and $i_{q\_ref\_vib}$ is the oscillation cancelling reference. The latter can be further developed as

$$i_{q\_ref\_vib} = I_c \sin\left(2\pi f_{\Gamma c} + \phi_c\right), \tag{4.6}$$

where I_c is the correction amplitude, $f_{\Gamma c}$ is the frequency of the correction and ϕ_c its phase. Setting the amplitude and phase of the correction to a proper value would then cancel the vibration observed at the frequency $f_{\Gamma c}$ without the need of tuning the PI controller, also without the need of adding a derivative part.

To test the effectiveness of the control proposed, several simulations are conducted. A torque load whose composition is shown in Table 4.2 is applied, and the oscillations are corrected individually. The results of the simulations are shown in Figure 4.11, Figure 4.12 and Figure 4.13, for each oscillation at 20, 40

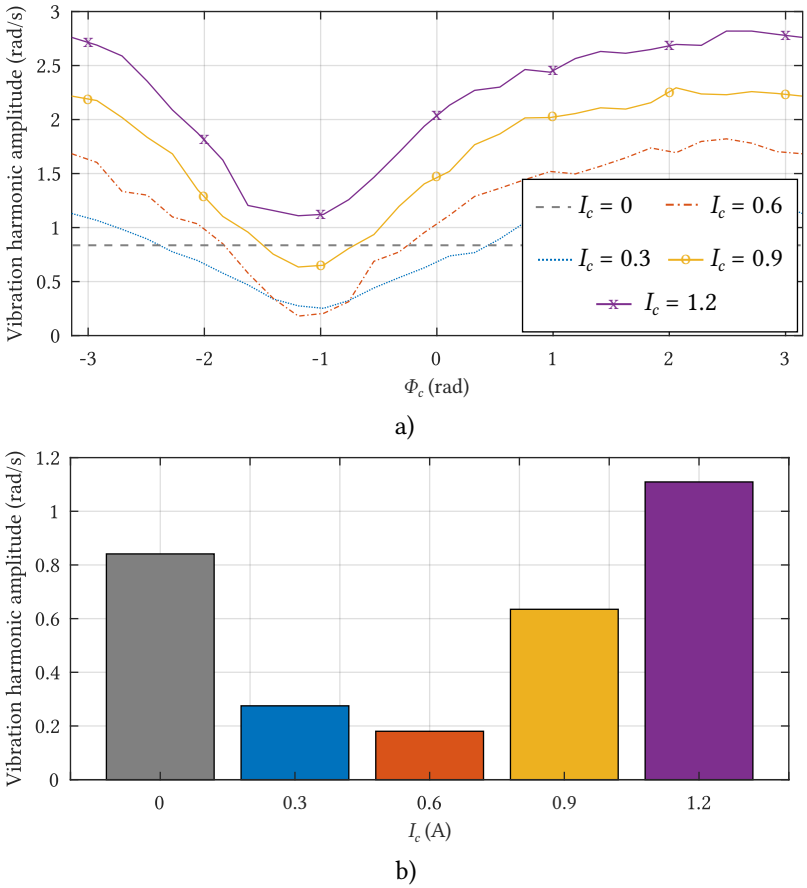

Figure 4.11: Active attenuation simulation results for the 20 Hz component. a) Amplitudes of the vibration harmonic for different amplitudes of the correction current, while sweeping the phase of the correction wave. b) Amplitudes of the vibration harmonic for different amplitudes of the correction current, for a correction phase $\phi_c = -1.1916$ rad.

and 60 Hz respectively. For each one, the correction phase is swept from $-\pi$ to π, and different amplitude levels are tried out for each phase value. In each case, there is a phase value that achieves the maximum correction for the oscillation observed. For that phase value, the bar plot compares the amplitude of the oscil-

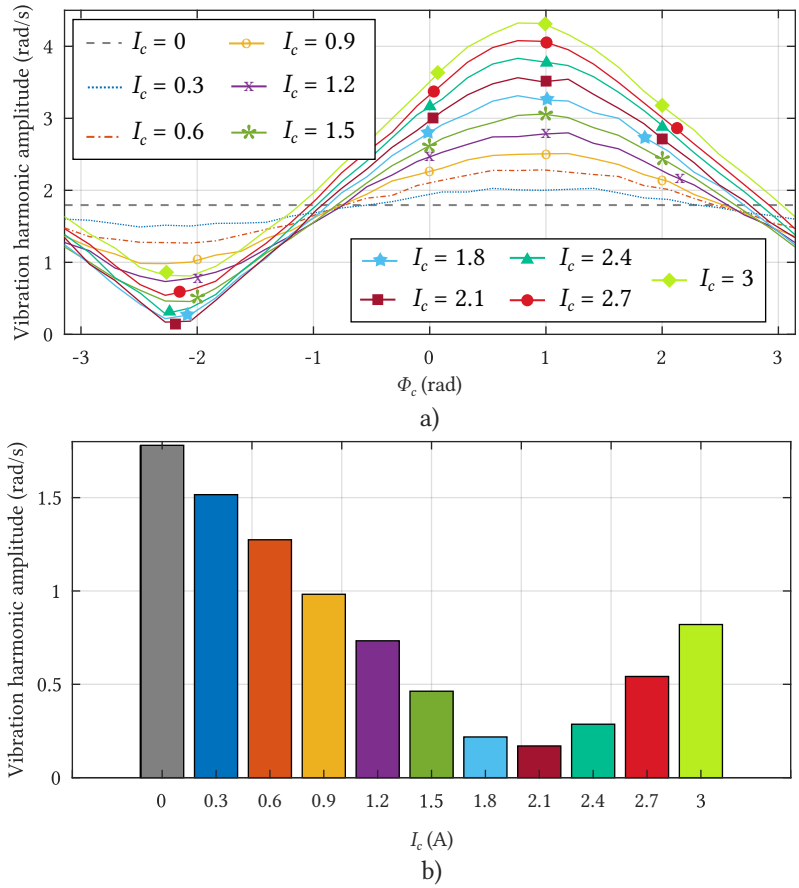

Figure 4.12: Active attenuation simulation results for the 40 Hz component. a) Amplitudes of the vibration harmonic for different amplitudes of the correction current, while sweeping the phase of the correction wave. b) Amplitudes of the vibration harmonic for different amplitudes of the correction current, for a correction phase $\phi_c = -2.2749$ rad.

lation for each value of correction amplitude, including the one when there is no correction at all. It can be observed how an error in the phase of the correction introduced could lead to an increase in the speed oscillation. Moreover, when the correct phase is used, increasing the correction amplitude will not always result

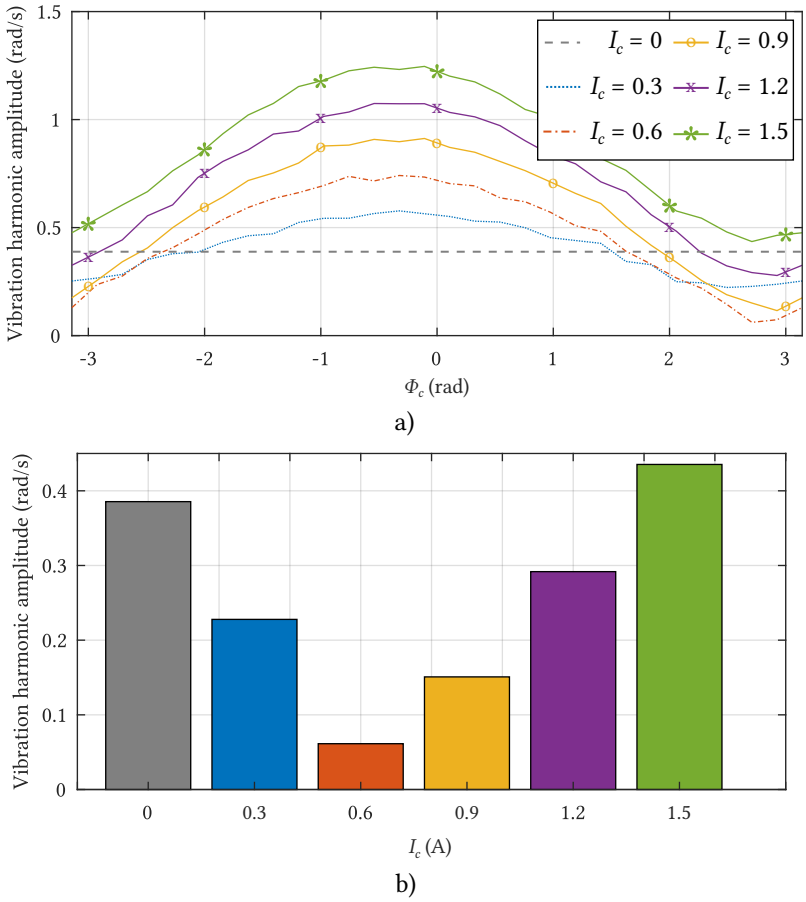

Figure 4.13: Active attenuation simulation results for the 40 Hz component. a) Amplitudes of the vibration harmonic for different amplitudes of the correction current, while sweeping the phase of the correction wave. b) Amplitudes of the vibration harmonic for different amplitudes of the correction current, for a correction phase $\phi_c = 2.7083$ rad.

in an smaller oscillation amplitude. Nevertheless, the correct selection of both parameters can effectively reduce the oscillations observed.

Comparing to the results obtained in the passive attenuation method from Figure 4.8, similar attenuations are obtained, but without the need of aggressivily

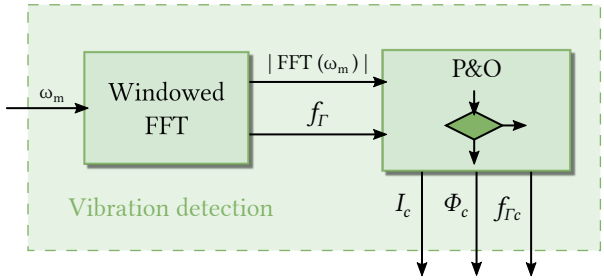

Figure 4.14: Vibration detection system with a windowed FFT and P&O algorithms.

tuning the speed controller or adding the derivative control. Moreover, the control developed can be used to build an iterative process based on Perturbation and Observation (P&O) , to automatically eliminate the oscillations detected in the speed. To that aim, the vibration detection model of the Figure 4.5 has to be able to detect the oscillation in the machine speed and produce the adequate references for the vibration controller from Figure 4.10. This model can be observed in Figure 4.14. It uses a windowed Fast Fourier Transform (FFT) to locate the main harmonics in the rotor speed and their amplitude. They consists of two arrays with the amplitudes $|\text{FFT}(\omega_m)|$ and the frequencies f_Γ. These values are then feeded to a P&O logic control, that will modify first the phase of the correction needed and then the amplitude. Figure 4.15 depicts the flow diagram of the P&O logic for the determination of the phase angle of the correction needed, ϕ_c. A similar approach is used for the correction of the amplitude used later on. The amplitude and phase will initially be set to some initial values as

$$\begin{aligned} I_{c_0} &= 1 \\ \phi_{c_0} &= 0, \end{aligned} \tag{4.7}$$

where the subindex 0 in I_c and ϕ_c indicates that is the initial value. The values

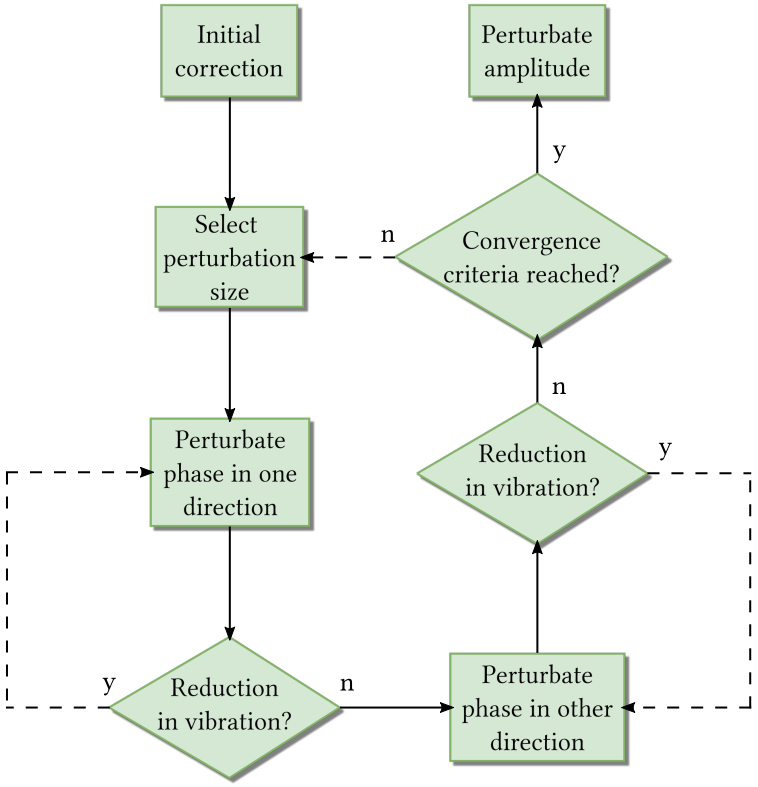

Figure 4.15: Perturbation and observation flow diagram for the determination of the correction phase.

for the next iterations of the P&O algorithm will be calculated as

$$\begin{aligned} I_{c_n} &= I_{c_{n-1}} + k\delta_A \\ \phi_{c_n} &= \phi_{c_{n-1}} + k\delta_{ph}, \end{aligned} \tag{4.8}$$

where δ_A and δ_{ph} are the perturbations introduced in the amplitude and phase, respectively . The subindex n refers to the iteration number of the algorithm and the constant k can be expressed as

$$k = \begin{cases} 1 & \Gamma(f_{\Gamma c})_{|n} < \Gamma(f_{\Gamma c})_{|n-1} \\ -1 & \text{otherwise,} \end{cases} \tag{4.9}$$

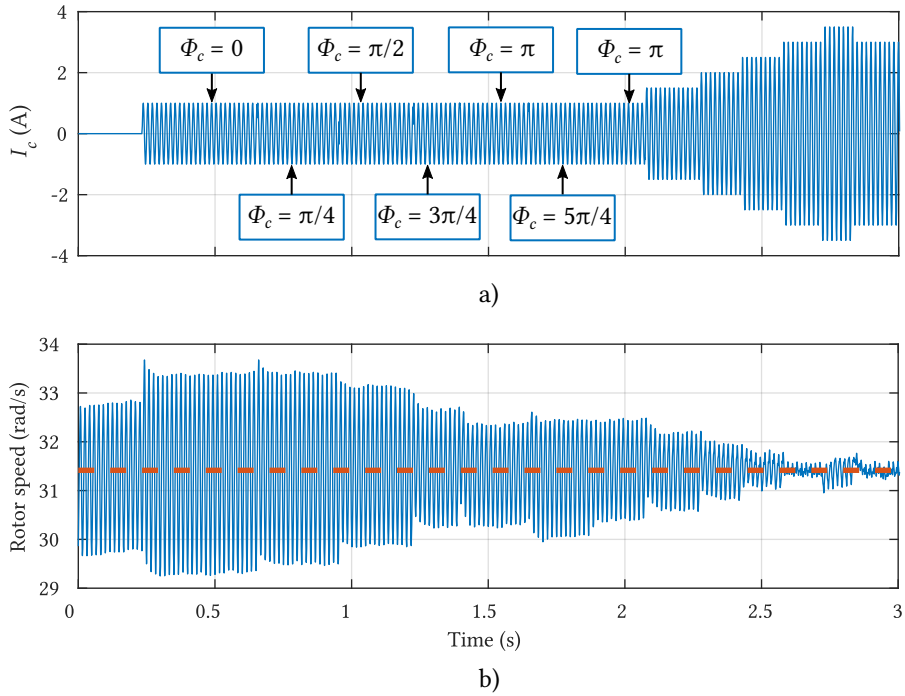

Figure 4.16: Simulation results of the active attenuation of oscillations based in P&O algorithm. a) Correction current used to cancel the oscillation observed. b) Rotor speed measured.

where $\Gamma(f_{\Gamma c})_{|n}$ is the amplitude of the oscillation observed at the n_{th} iteration.

By using (4.8) and (4.9), the system will introduce perturbations in order to look for the minimum possible value. First it will try to find the proper phase value, and the amplitude. As it is depicted in Figure 4.15, when the algorithm starts to change the direction in every iteration, a convergence criteria can be set to check if the oscillation has been removed. If it is not, the values δ_A and δ_{ph} can be reduced to try again.

Figure 4.16 depicts an example of the application of the P&O algorithm applied to the active attenuation technique described. The reference speed is set to

300 rpm, and the load applied is formbed by $T_0 = 4$ Nm and $T_{12} = 6$ Nm. This produces a speed oscillation at 60 Hz which without correction, has an amplitude of 2 rad/s. First, a correction $i_{q\_ref\_vib}$ is introduced at the same frequency, $f_{\Gamma c} = 60$ Hz, using the values from (4.7). Next, perturbations in the phase for the correction ϕ_c will be used to find the proper value, as it can be observed in Figure 4.16 a). The size for these perturbations will be $\delta_{ph} = \pi/4$. Since the oscillation amplitude is reduced with the first increment of the phase from 0 to $\pi/4$ as can be seen in Figure 4.16 b), the next perturbations will be made in the same direction. When the pase changes from π to $5\pi/4$, the oscillation amplitude becomes larger, so the direction for the perturbation will also change. Reverting the phase increment direction sets $\phi_c = \pi$ once again. At this point, the algorithm would continue alternating around this minimum. The size of δ_{ph} could be decreased to obtain better results, but for simplicity's sake, it will not be done for this example. Then, the same procedure is carried out, finishing when the amplitude for the correction achieves a minimum in the speed oscillation at $I_c = 3$ A. Similarly as it was explained for the phase, the perturbation in amplitude δ_A could be tweaked to achieve a better attenuation, but from Figure 4.16 b), it is clear that the attenuation is almost complete.

4.4 Conclusions

The analysis and supression of vibrations in a structure coupled to a rotative machine has been discussed in this chapter. An experimental NVH analysis has been carried out, studying the vibrations observed in the frequency domain. A relation between the rotor speed and the vibrations is observed, which is used for modelling the system in simulation. Afterwards, the effect of the speed controller on the oscillations is evaluated, adding to the controller used previously a derivative control. It is then compared to an active attenuation controller that

makes use of the information given by the NVH study to correct the oscillations. The following can be concluded from this work:

1. The NVH study reveals that the vibrations produced in the system are dependant of the motor speed, and not so much on the motor loading.

2. When considering the PID speed controller, the proportional and derivative parts are the most effective in supressing vibrations. However, the agressive tuning of this parameters could deteriorate the behaviour of the system under certain circumstances.

3. Understanding how the PID generated each part of its references leads to the conclussion that adding a sinusoidal reference to the one coming from the regular PI controller, with the same frequency as the oscillation observed but different phase and amplitude, can be used to supress the vibration.

4. The search of the adequate values for the phase and amplitude of the correction can be regarded as an iterative process, suitable for an implementation using a P&O method looking for the minimum oscillation possible.

5. The frequencies of the oscillations observed are provided by a windowed FFT of the rotor speed. In order to be able to detect the vibrations located at multiples of the rotor speed, the sampling frequency for this model has to be considerably lowered.

6. The current controller bandwidth has to be wide enough to correctly follow the references set by the vibration controller. Depending on the rotor speed and the harmonic considered, this could prove troublesome.

5

Conclusions and future work

5.1 Conclusiones

Al comienzo de este trabajo se ha hablado de la importancia que tiene actualmente el Vehículo Eléctrico (VE), y la que ha de ganar en los próximos años. La Unión Europea (EU) ha pasado a la acción en los objetivos marcados por los distintos acuerdos internacionales en lo relativo a cambio climático, siendo uno de los aspectos clave una movilidad libre de emisiones. Por lo tanto, la investigación en el campo del VE nunca ha sido tan relevante y prometedora, ya que juega un papel decisivo en los cambios que acontecen a la sociedad en los próximos años.

Este trabajo ha presentado resultados en tres líneas de investigación relativas al VE. En primer lugar se ha estudiado las deficiencias del control del motor eléctrico sin sensor del VE, proponiéndose un nuevo algoritmo capaz de controlarlo. Existen en la literatura multitud de técnicas diferentes de control sin sensor del motor, cada una intentando superar las dificultades de este tipo de control de una forma distinta. Sin embargo, un denominador común es que generalmente requieren una gran tensión de inyección para funcionar de forma correcta, y sólo en determinados tipos de máquinas que presenten una gran saliencia, lo

que limita su aplicación. El algoritmo desarrollado es capaz de operar incluso cuando se usa una tensión de inyección muy pequeña, y se trata de una máquina con baja saliencia. Resultados de simulación y experimentales avalan el buen funcionamiento del algoritmo propuesto, en variedad de pruebas y condiciones de operación. Este tipo de control es de alto interés en el VE ya que supone un ahorro de componentes y un aumento de la fiabilidad del sistema, lo que se traduce en una reducción de costes y mantenimiento.

A continuación, se ha analizado el papel del VE en las comunidades inteligentes. Por su naturaleza, el sistema del almacenamiento de energía y el cargador pueden prestar servicios al consumidor y a la red eléctrica, mientras el VE está estacionado y enchufado. Es beneficioso para los usuarios ya que se puede usar la energía almacenada en el VE para evitar consumir de la red en periodos en los que el precio de la energía esté más alto, y cargar el VE cuando sea más bajo. Por otro lado, es beneficioso para la red ya que puede proporcionar servicios de compensación de energía reactiva y compensación de corriente armónica, contribuyendo a la mejora del servicio eléctrico. En este trabajo se ha desarrollado una topología de cargador monofásico bidireccional que integra las funciones descritas. Los ensayos realizados muestran la efectividad del cargador diseñado cuando se carga o descarga el VE, se corrigen las componentes armónicas de la corriente demandada por el hogar y se proporciona la energía reactiva necesaria. Además, se han ensayado un sistema de almacenamiento híbrido compuesto por un supercondensador junto a la batería, usando un sistema de reparto de energía beneficioso para la vida útil de esta última. Por último, se ha analizado la posibilidad de integrar el cargador con la electrónica de potencia ya presente en el VE para lograr un Cargador a Bordo Integrado (CBI). El objetivo es disminuir la cantidad de componentes necesarios, redundando en la reducción de costes. Sin embargo, integrar los bobinados de la máquina en el diseño del cargador provoca la aparición de momentos de par indeseados en el vehículo. Para paliar este

problema, se ha propuesto una estrategia de control de las corrientes usadas en el cargador que asegure que no se genera par en la máquina cuando se usa para cargar el VE. Aunque dicha estrategia anula el par generado, también disminuye la eficiencia de carga según la posición del rotor. No obstante, se ha demostrado mediante simulación que es posible evitar la disminución de la eficiencia mediante una estrategia que decide la conexión más eficaz en función de la posición del rotor, adaptando el resto de corrientes adecuadamente. La efectividad de la cancelación del par ha sido demostrada mediante simulación y experimentos.

Finalmente, en el último capítulo se ha realizado un estudio experimental de Ruidos y Vibraciones (NVH de sus siglas en inglés). Dicho estudio ha permitido analizar las vibraciones presentes en una estructura acoplada a un motor eléctrico, como podría ser el de un VE. El espectro en frecuencia de las vibraciones observadas revela que hay una relación entre la velocidad de giro y las características de dichas vibraciones, lo cual ha sido usado para la elaboración de un modelo de simulación. Dicho modelo ha permitido el desarrollo de un sistema de amortiguación activo de vibraciones, el cual se adapta a las vibraciones observadas y es independiente del controlador de velocidad usado. Dicho algoritmo puede ser usado de forma iterativa mediante la combinación con el algoritmo de perturbación y observación para la eliminación de distintas vibraciones observadas en la estructura de manera sistemática. Ensayos mediante simulación demuestran el buen funcionamiento del mismo.

5.2 Conclusions

At the beginning of this work it was discussed the importance that the Electric Vehicle (EV) has nowadays, and even more in the years to come. The European Union (EU) has taken the lead in the objectives marked in the different international agreements related to climate change, being one of the key aspects

the emission-free mobility. Therefore, research in the EV field has never been so relevant and promising, given that it plays a fundamental role in the changes that will affect society in the following years.

This work has presented results in three research lines related to the EV. First, the sensorless control of the motor in the EV has been analyzed, proposing a new algorithm able to control it successfully. There are plenty of different techniques for doing so in the literature, each one trying to overcome the difficulties that this kind of control exhibits. However, most of them share the need of a very high injection voltage for the control to work, and only in the machines that present a high salience ratio. The algorithm developed in this work can control the machine using a very low injection voltage and using a low salience machine. Simulation and experimental results show the good operation of the proposed control under several conditions. This kind of control is of great interest since it means a reduction of costs and an increase of the reliability of the system.

Next, the role of the EV in the smart communities is analyzed. Due to its own nature, the storage system and EV charger can prove usefull for both the individual user and the electric grid, while the EV is connected to it. The benefits for the user include using the energy stored in the system to avoid consuming from the grid when the energy price is higher, and charge the EV when is lower. On the other hand, it can provide grid services like reactive energy and harmonic current compensation. In this work, a bidirectional single phase topology for the charger providing the grid functions described has been developed. The simulations and experiments conducted prove the usefulness of the charger when the battery is charged or discharged, and the reactive and harmonic currents are compensated. Moreover, a hybrid storage system made up of batteries and a supercapacitor has been tested, using a current sharing strategy that can extend the battery life. Furthermore, the possibility of integrating the charger in the EV using the power electronics already available in the EV driving system to

achieve an Integrated On-board Charger (IOC). However, integrating the machine windings in the charger electronics can produce undesired charging torque. In order to tackle this issue, a new charging current control is used for eliminating the torque produced. Although the torque is removed, it also can decrease the charging efficiency depending on the rotor position while charging. Nevertheless, it has been proved by simulation that the reduction in charging efficiency can be avoided switching the connection to the grid from one phase to another by means of a control strategy that decides the best one, adapting the charging currents accordingly. The effectiveness of the torque removal has been tested in simulations and experiments.

Finally, in the last chapter an experimental Noise Vibration and Harshness (NVH) study has been carried out. The results obtained allowed the analysis of the vibrations encountered in an structure couple to a electric motor, as it could be an EV. The frequency spectrum of the vibrations observed reveals that there is a relationship between the rotational frequency and the vibrations characteristics. This fact has been used to develop a simulation model to come up with an active damping system. It has the advantage of being independent of the speed controller used and it adapts to the vibrations observed. This algorithm can be combined with a Perturbation and Observation (P&O) algorithm to remove vibrations in an iterative way. Simulation tests prove the good operation of the control developed.

5.3 Future work

Although this work has presented results in three different research lines, there is still much work ahead. As it was mentioned in Chapter 1, the EV is going to receive a lot of attention in the years to come, and so is research about it. This

dissertation is intended as a starting point, and so the following can be advanced as future work:

- Although the sensorless technique developed presents some advantages compared to the ones found in the literature, the trend nowadays is to raise the injection frequency using square wave injection. It allows avoiding problems related with noise caused by the high frequency noise if it is raised above human hearing, and some authors report better results compared to sinusoidal injection. A thorough study comparing both techniques could provide useful information, comparing where each one excels.

- Extend the control algorithms developed to the case of a three phase charger of the EV. Add more grid functions to it such as the correction of unbalanced systems.

- Analyze the operation of the Smart Community Energy Management System (SCEMS) as an aggregator of resources for a better integration with the Smart Grid. The current references generated by the SCEMS can fulfill more objectives like the optimization of the community batteries lifetime or the global power factor correction.

- Deepen the NVH analysis made by means of the implementation of a variable loading device able to introduce more vibration conditions into the system. This will allow to test the active vibration control proposed in an experimental setup.

- Extend the algorithms developed to other kind of machines, such as the Synchronous Reluctance Machine (SRM) or the Permanent Magnet Assisted SRM (PMASRM). Both machines exhibit great potential in the EV field sharing some advantages with the PMSM but lacking the need for

rare earth magnets (since the magnets used in the PMASRM are normally ferrite).

5.4 Publications

The following publications are the result of the predoctoral stage of the candidate. This work is mostly based on them, although there are some conference publications not strictly related.

Journal article	M.-I. Milanes-Montero, F. Barrero-Gonzalez, J. Pando-Acedo, E. Gonzalez-Romera, E. Romero-Cadaval, and A. Moreno-Munoz, "Active, Reactive and Harmonic Control for Distributed Energy Micro-Storage Systems in Smart Communities Homes," Energies, vol. 10, no. 4, Art. no. 4, Apr. 2017, doi: 10.3390/en10040448.	Q2 (2.676) Energy & Fuels
Journal article	M. I. Milanés-Montero, F. Barrero-González, J. Pando-Acedo, E. González-Romera, E. Romero-Cadaval, and A. Moreno-Munoz, "Smart Community Electric Energy Micro-Storage Systems With Active Functions," IEEE Transactions on Industry Applications, vol. 54, no. 3, pp. 1975–1982, May 2018, doi: 10.1109/TIA.2018.2799547.	Q1 (2.743) Engineering, Multidisciplinary
Journal article	J. Pando-Acedo, E. Romero-Cadaval, M. I. Milanes-Montero, and F. Barrero-Gonzalez, "Improvements on a Sensorless Scheme for a Surface-Mounted Permanent Magnet Synchronous Motor Using Very Low Voltage Injection," Energies, vol. 13, no. 11, Art. no. 11, Jan. 2020, doi: 10.3390/en13112732.	Q3 (2.702) Energy & Fuels

Journal article	J. Pando-Acedo, M. I. Milanés Montero, E. Romero Cadaval, F. Briz, and F. Barrero-González, "Improved Three-Phase Integrated Charger Converter Connected to Single-Phase Grid with Torque Cancellation," Pending Publication.
Conference paper	J. Pando-Acedo, M. I. Milanés-Montero, E. Romero-Cadaval, M. A. Guerrero-Martínez, F. Barrero-González, and E. González-Romera, "Active power flow strategies for bidirectional Energy Storage Units in smart communities," in 2017 11th IEEE International Conference on Compatibility, Power Electronics and Power Engineering (CPE-POWERENG), Apr. 2017, pp. 614–619. doi: 10.1109/CPE.2017.7915243.
Conference paper	A. Rassolkin, H. Heidari, A. Kallaste, T. Vaimann, J. P. Acedo, and E. Romero-Cadaval, "Efficiency Map Comparison of Induction and Synchronous Reluctance Motors," in 2019 26th International Workshop on Electric Drives: Improvement in Efficiency of Electric Drives (IWED), Jan. 2019, pp. 1–4. doi: 10.1109/IWED.2019.8664334.
Conference paper	J. Pando-Acedo et al., "Hybrid FEA-Simulink Modelling of Permanent Magnet Assisted Synchronous Reluctance Motor with Unbalanced Magnet Flux," in 2019 IEEE 12th International Symposium on Diagnostics for Electrical Machines, Power Electronics and Drives (SDEMPED), Aug. 2019, pp. 174–180. doi: 10.1109/DEMPED.2019.8864925.

Conference paper	J. Pando-Acedo, E. Romero-Cadaval, C. Gragera-Peña, and M. I. Milanés-Montero, "Noise, Vibration and Harshness on a Permanent Magnet Synchronous Motor for a Remote Laboratory," in Technological Innovation for Smart Systems, Cham, 2017, pp. 382–389. doi: 10.1007/978-3-319-56077-9_37.
Conference paper	J. Pando-Acedo, E. Romero-Cadaval, and M. I. Milanés-Montero, "Estudio Comparativo de Técnicas Sensorless en un Motor Síncrono de Imanes Permanentes," presented at the XXV Seminario Anual de Automática, Electrónica Industrial e Instrumentación, Barcelona, España, Jul. 2018.
Conference paper	J. Pando-Acedo, "Implementation Issues and Considerations for a FOC of an IM using Speedgoat," presented at the Doctoral School of Energy and Geotechnology, Toila, Estonia, Jan. 2019.
Conference paper	J. Pando-Acedo, E. Romero Cadaval, and M. I. Milanés-Montero, "Topología de Tensión de Bus Variable para la Regulación de Velocidad en Motores," presented at the XXVII Seminario Anual de Automática, Electrónica Industrial e Instrumentación, Ciudad Real, España, Sep. 2020.

References

[1] "Global Warming of 1.5 ºC." Special Report, Intergovernmental Panel on Climate Change (IPCC) 2018.

[2] "Commission Communication - The European Green Deal." COM(2019) 640 final of 11 December 2019.

[3] "Proyecto de Ley de Cambio Climático y Transición Energética." Ministerio para la Transición Ecológica y el Reto Demográfico.

[4] "Plan Nacional Integrado de Energía y Clima (PNIEC) 2021-2030." Ministerio para la Transición Ecológica y el Reto Demográfico.

[5] Z. Wang, J. Chen, M. Cheng, and K. T. Chau, "Field-Oriented Control and Direct Torque Control for Paralleled VSIs Fed PMSM Drives With Variable Switching Frequencies," *IEEE Transactions on Power Electronics*, vol. 31, pp. 2417–2428, Mar. 2016. Conference Name: IEEE Transactions on Power Electronics.

[6] J. Lara, J. Xu, and A. Chandra, "Effects of Rotor Position Error in the Performance of Field-Oriented-Controlled PMSM Drives for Electric Vehicle Traction Applications," *IEEE Transactions on Industrial Electronics*, vol. 63, pp. 4738–4751, Aug. 2016. Conference Name: IEEE Transactions on Industrial Electronics.

[7] U. Gupta, D. K. Yadav, and D. Panchauli, "Field Oriented Control of PMSM during Regenerative Braking," in *2019 Global Conference for Advancement in Technology (GCAT)*, pp. 1–5, Oct. 2019.

[8] H. Gashtil, V. Pickert, D. Atkinson, D. Giaouris, and M. Dahidah, "Comparative Evaluation of Field Oriented Control and Direct Torque Control Methodologies in Field Weakening Regions for Interior Permanent Magnet Machines," in *2019 IEEE 13th International Conference on Compatibility, Power Electronics and Power Engineering (CPE-POWERENG)*, pp. 1–6, Apr. 2019. ISSN: 2166-9546.

[9] K. Lee, T. Gu, and Y. Bang, "Analysis of Accuracy and Measuring Range of Dual Absolute Encoder System," *IEEE Sensors Journal*, vol. 20, pp. 2997–3004, Mar. 2020. Conference Name: IEEE Sensors Journal.

[10] F. Tootoonchian, "Proposal of a New Affordable 2-Pole Resolver and Comparing Its Performance With Conventional Wound-Rotor and VR Resolvers," *IEEE Sensors Journal*, vol. 18, pp. 5284–5290, July 2018. Conference Name: IEEE Sensors Journal.

[11] A. Anuchin, V. Astakhova, D. Shpak, A. Zharkov, and F. Briz, "Optimized method for speed estimation using incremental encoder," in *2017 International Symposium on Power Electronics (Ee)*, (Novi Sad), pp. 1–5, IEEE, Oct. 2017.

[12] J. Holtz, "Sensorless Control of Induction Machines—With or Without Signal Injection?," *IEEE Transactions on Industrial Electronics*, vol. 53, pp. 7–30, Feb. 2006.

[13] R. Bojoi, M. Pastorelli, J. Bottomley, P. Giangrande, and C. Gerada, "Sensorless control of PM motor drives — A technology status review," in *2013 IEEE Workshop on Electrical Machines Design, Control and Diagnosis (WEMDCD)*, pp. 168–182, Mar. 2013.

[14] Z. Guoqiang and W. Gaolin, "Saliency-based position sensorless control methods for PMSM drives - A review," *Chinese Journal of Electrical Engineering*, vol. 3, pp. 14–23, Sept. 2017.

[15] G. Wang, M. Valla, and J. Solsona, "Position Sensorless Permanent Magnet Synchronous Machine Drives—A Review," *IEEE Transactions on Industrial Electronics*, vol. 67, pp. 5830–5842, July 2020. Conference Name: IEEE Transactions on Industrial Electronics.

[16] R. Antonello, L. Ortombina, F. Tinazzi, and M. Zigliotto, "Enhanced Low-Speed Operations for Sensorless Anisotropic PM Synchronous Motor Drives by a Modified Back-EMF Observer," *IEEE Transactions on Industrial Electronics*, vol. 65, pp. 3069–3076, Apr. 2018.

[17] G. Lindemann, B. Weber, and A. Mertens, "Reducing the Low-Speed Limit for Back-EMF Based Self-Sensing Speed Control by Using an FPGA-Operated Dead-Time Compensation," in *2018 IEEE 9th International Symposium on Sensorless Control for Electrical Drives (SLED)*, (Helsinki), pp. 60–65, IEEE, Sept. 2018.

[18] F. Demmelmayr, M. Troyer, and M. Schroedl, "Comparison of a linear and a non-linear state observer for sensorless control of PM machines," in *2013 IEEE International Symposium on Sensorless Control for Electrical Drives and Predictive Control of Electrical Drives and Power Electronics (SLED/PRECEDE)*, (München, Germany), pp. 1–5, IEEE, Oct. 2013.

[19] D. Bao, X. Pan, Y. Wang, X. Wang, and K. Li, "Adaptive Synchronous-Frequency Tracking-Mode Observer for the Sensorless Control of a Surface PMSM," *IEEE Transactions on Industry Applications*, vol. 54, pp. 6460–6471, Nov. 2018.

[20] D. Lee and K. Akatsu, "The study on transient performance improvement of position sensorless control algorithm for IPMSM," in *2017 IEEE International Symposium on Sensorless Control for Electrical Drives (SLED)*, (Catania, Italy), pp. 67–72, IEEE, Sept. 2017.

[21] A. Khlaief, M. Bendjedia, M. Boussak, and M. Gossa, "A Nonlinear Observer for High-Performance Sensorless Speed Control of IPMSM Drive," *IEEE Transactions on Power Electronics*, vol. 27, pp. 3028–3040, June 2012.

[22] M. Linke, R. Kennel, and J. Holtz, "Sensorless position control of permanent magnet synchronous machines without limitation at zero speed," in *IEEE 2002 28th Annual Conference of the Industrial Electronics Society. IECON 02*, vol. 1, (Sevilla, Spain), pp. 674–679, IEEE, 2002.

[23] P. L. Xu and Z. Q. Zhu, "Novel Square-Wave Signal Injection Method Using Zero-Sequence Voltage for Sensorless Control of PMSM Drives," *IEEE Transactions on Industrial Electronics*, vol. 63, pp. 7444–7454, Dec. 2016.

[24] W. Limei, G. Qingding, and R. D. Lorenz, "Sensorless Control of Permanent Magnet Synchronous Motor," (Beijing, China, China), p. 5, IEEE, 2000.

[25] W. Hammel and R. Kennel, "Integration of alternating carrier injection in position sensorless control without any filtering," in *2009 IEEE Energy Conversion Congress and Exposition*, (San Jose, CA), pp. 3830–3836, IEEE, Sept. 2009.

[26] J. Holtz, "Developments in Sensorless AC Drive Technology," in *2005 International Conference on Power Electronics and Drives Systems*, vol. 1, (Kuala Lumpur, Malaysia), pp. 9–16, IEEE, 2005.

[27] X. Jin, R. Ni, W. Chen, F. Blaabjerg, and D. Xu, "High-Frequency Voltage-Injection Methods and Observer Design for Initial Position Detection of Perma-

nent Magnet Synchronous Machines," *IEEE Transactions on Power Electronics*, vol. 33, pp. 7971–7979, Sept. 2018.

[28] J. Holtz, "Acquisition of Position Error and Magnet Polarity for Sensorless Control of PM Synchronous Machines," *IEEE Transactions on Industry Applications*, vol. 44, no. 4, pp. 1172–1180, 2008.

[29] E. Trancho, E. Ibarra, A. Arias, I. Kortabarria, and P. Prieto, "A practical approach to HFI based sensorless control of PM-assisted synchronous reluctance machines applied to EVs and HEVs," in *IECON 2017 - 43rd Annual Conference of the IEEE Industrial Electronics Society*, (Beijing), pp. 1735–1740, IEEE, Oct. 2017.

[30] C.-E. Hwang, Y. Lee, and S.-K. Sul, "Analysis on Position Estimation Error in Position-Sensorless Operation of IPMSM Using Pulsating Square Wave Signal Injection," *IEEE Transactions on Industry Applications*, vol. 55, pp. 458–470, Jan. 2019.

[31] S.-I. Kim, J.-H. Im, E.-Y. Song, and R.-Y. Kim, "A New Rotor Position Estimation Method of IPMSM Using All-Pass Filter on High-Frequency Rotating Voltage Signal Injection," *IEEE Transactions on Industrial Electronics*, vol. 63, pp. 6499–6509, Oct. 2016.

[32] Q. Tang, A. Shen, X. Luo, and J. Xu, "PMSM Sensorless Control by Injecting HF Pulsating Carrier Signal Into ABC Frame," *IEEE Transactions on Power Electronics*, vol. 32, pp. 3767–3776, May 2017.

[33] M. W. Degner, "Position Estimation in Induction Machines Utilizing Rotor Bar Slot Harmonics and Carrier-Frequency Signal Injection," *IEEE TRANSACTIONS ON INDUSTRY APPLICATIONS*, vol. 36, no. 3, p. 7, 2000.

[34] M. Corley and R. Lorenz, "Rotor position and velocity estimation for a salient-pole permanent magnet synchronous machine at standstill and high speeds," *IEEE Transactions on Industry Applications*, vol. 34, pp. 784–789, Aug. 1998.

[35] Z. Q. Zhu and L. M. Gong, "Investigation of Effectiveness of Sensorless Operation in Carrier-Signal-Injection-Based Sensorless-Control Methods," *IEEE Transactions on Industrial Electronics*, vol. 58, pp. 3431–3439, Aug. 2011.

[36] D. Raca, P. García, D. Reigosa, F. Briz, and R. D. Lorenz, "Carrier Signal Selection for Sensorless Control of PM Synchronous Machines at Zero and Very Low Speeds," *IEEE Transactions on Industry Applications*, vol. 46, no. 1, p. 8, 2010.

[37] F. Briz, M. Degner, P. Garcia, and R. Lorenz, "Comparison of Saliency-Based Sensorless Control Techniques for AC Machines," *IEEE Transactions on Industry Applications*, vol. 40, pp. 1107–1115, July 2004.

[38] F. Briz, M. Degner, P. Garcia, and J. Guerrero, "Rotor Position Estimation of AC Machines Using the Zero-Sequence Carrier-Signal Voltage," *IEEE Transactions on Industry Applications*, vol. 41, pp. 1637–1646, Nov. 2005.

[39] G. Wang, J. Kuang, N. Zhao, G. Zhang, and D. Xu, "Rotor Position Estimation of PMSM in Low-Speed Region and Standstill Using Zero-Voltage Vector Injection," *IEEE Transactions on Power Electronics*, vol. 33, pp. 7948–7958, Sept. 2018.

[40] Young-Doo Yoon, Seung-Ki Sul, S. Morimoto, and K. Ide, "High-Bandwidth Sensorless Algorithm for AC Machines Based on Square-Wave-Type Voltage Injection," *IEEE Transactions on Industry Applications*, vol. 47, pp. 1361–1370, May 2011.

[41] R. Ni, D. Xu, F. Blaabjerg, K. Lu, G. Wang, and G. Zhang, "Square-Wave Voltage Injection Algorithm for PMSM Position Sensorless Control With High Robustness to Voltage Errors," *IEEE Transactions on Power Electronics*, vol. 32, pp. 5425–5437, July 2017.

[42] M. A. Ghazi Moghadam and F. Tahami, "Sensorless control of PMSMs with tolerance for delays and stator resistance uncertainties," *IEEE Transactions on Power Electronics*, vol. 28, pp. 1391–1399, Mar. 2013.

[43] G. Xie, K. Lu, S. K. Dwivedi, J. R. Rosholm, and F. Blaabjerg, "Minimum-Voltage Vector Injection Method for Sensorless Control of PMSM for Low-Speed Operations," *IEEE Transactions on Power Electronics*, vol. 31, pp. 1785–1794, Feb. 2016.

[44] P. Xu and Z. Zhu, "Carrier signal injection-based sensorless control for permanent magnet synchronous machine drives with tolerance of signal processing delays," *IET Electric Power Applications*, vol. 11, pp. 1140–1149, July 2017.

[45] T. C. Lin and Z. Q. Zhu, "Sensorless Operation Capability of Surface-Mounted Permanent-Magnet Machine Based on High-Frequency Signal Injection Methods," *IEEE Transactions on Industry Applications*, vol. 51, pp. 2161–2171, May 2015.

[46] Zhixun Ma and R. Kennel, "System-on-Chip sensorless control of PMSM combining signal injection and flux observer," in *Proceedings of The 7th International*

Power Electronics and Motion Control Conference, (Harbin, China), pp. 1201–1205, IEEE, June 2012.

[47] X. Luo, Q. Tang, A. Shen, and Q. Zhang, "PMSM Sensorless Control by Injecting HF Pulsating Carrier Signal Into Estimated Fixed-Frequency Rotating Reference Frame," *IEEE Transactions on Industrial Electronics*, vol. 63, pp. 2294–2303, Apr. 2016.

[48] D. Kim, Y.-C. Kwon, S.-K. Sul, J.-H. Kim, and R.-S. Yu, "Suppression of Injection Voltage Disturbance for High-Frequency Square-Wave Injection Sensorless Drive With Regulation of Induced High-Frequency Current Ripple," *IEEE Transactions on Industry Applications*, vol. 52, pp. 302–312, Jan. 2016.

[49] H. W. De Kock, M. J. Kamper, and R. M. Kennel, "Anisotropy Comparison of Reluctance and PM Synchronous Machines for Position Sensorless Control Using HF Carrier Injection," *IEEE Transactions on Power Electronics*, vol. 24, pp. 1905–1913, Aug. 2009.

[50] P. Garcia, F. Briz, M. Degner, and D. Diaz-Reigosa, "Accuracy and Bandwidth Limits of Carrier Signal Injection-Based Sensorless Control Methods," in *Conference Record of the 2006 IEEE Industry Applications Conference Forty-First IAS Annual Meeting*, vol. 2, (Tampa, FL), pp. 897–904, IEEE, Oct. 2006. ISSN: 0197-2618.

[51] R. Davies, M. Sumner, and E. Christopher, "Energy storage control for a small community microgrid," in *7th IET International Conference on Power Electronics, Machines and Drives (PEMD 2014)*, pp. 1–6, Apr. 2014.

[52] L. Sharifi, F. Freitag, and L. Veiga, "Combing Smart Grid with community clouds: Next generation integrated service platform," in *2014 IEEE International Conference on Smart Grid Communications (SmartGridComm)*, pp. 434–439, Nov. 2014.

[53] J. Li, Z. Wu, S. Zhou, H. Fu, and X.-P. Zhang, "Aggregator service for PV and battery energy storage systems of residential building," *CSEE Journal of Power and Energy Systems*, vol. 1, pp. 3–11, Dec. 2015. Conference Name: CSEE Journal of Power and Energy Systems.

[54] C. J. Mozina, "Impact of smart grid and green power generation on distribution systems," in *2012 IEEE PES Innovative Smart Grid Technologies (ISGT)*, pp. 1–13, Jan. 2012.

[55] H. Kanchev, D. Lu, F. Colas, V. Lazarov, and B. Francois, "Energy Management and Operational Planning of a Microgrid With a PV-Based Active Generator for Smart Grid Applications," *IEEE Transactions on Industrial Electronics*, vol. 58, pp. 4583–4592, Oct. 2011. Conference Name: IEEE Transactions on Industrial Electronics.

[56] E. González-Romera, F. Barrero-González, E. Romero-Cadaval, and M. I. Milanés-Montero, "Overview of plug-in electric vehicles as providers of ancillary services," in *2015 9th International Conference on Compatibility and Power Electronics (CPE)*, pp. 516–521, June 2015. ISSN: 2166-9546.

[57] S. A. Saleh, P. Pijnenburg, and E. Castillo-Guerra, "Load Aggregation From Generation-Follows-Load to Load-Follows-Generation: Residential Loads," *IEEE Transactions on Industry Applications*, vol. 53, pp. 833–842, Mar. 2017. Conference Name: IEEE Transactions on Industry Applications.

[58] S. Aman, Y. Simmhan, and V. K. Prasanna, "Energy management systems: state of the art and emerging trends," *IEEE Communications Magazine*, vol. 51, pp. 114–119, Jan. 2013. Conference Name: IEEE Communications Magazine.

[59] R. C. Dugan, J. A. Taylor, and D. Montenegro, "Energy Storage Modeling for Distribution Planning," *IEEE Transactions on Industry Applications*, vol. 53, pp. 954–962, Mar. 2017. Conference Name: IEEE Transactions on Industry Applications.

[60] M. Farhadi and O. Mohammed, "Energy Storage Technologies for High-Power Applications," *IEEE Transactions on Industry Applications*, vol. 52, pp. 1953–1961, May 2016. Conference Name: IEEE Transactions on Industry Applications.

[61] A. A. Hussein, N. Kutkut, Z. J. Shen, and I. Batarseh, "Distributed Battery Micro-Storage Systems Design and Operation in a Deregulated Electricity Market," *IEEE Transactions on Sustainable Energy*, vol. 3, pp. 545–556, July 2012. Conference Name: IEEE Transactions on Sustainable Energy.

[62] J. Gallardo-Lozano, M. I. Milanés-Montero, M. A. Guerrero-Martínez, and E. Romero-Cadaval, "Three-phase bidirectional battery charger for smart electric vehicles," in *2011 7th International Conference-Workshop Compatibility and Power Electronics (CPE)*, pp. 371–376, June 2011. ISSN: 2166-9546.

[63] J. Gomez and M. Morcos, "Impact of EV battery chargers on the power quality of distribution systems," *IEEE Transactions on Power Delivery*, vol. 18, pp. 975–981, July 2003. Conference Name: IEEE Transactions on Power Delivery.

[64] X. Liang, "Emerging Power Quality Challenges Due to Integration of Renewable Energy Sources," *IEEE Transactions on Industry Applications*, vol. 53, pp. 855–866, Mar. 2017. Conference Name: IEEE Transactions on Industry Applications.

[65] O. C. Onar and A. Khaligh, "Grid interactions and stability analysis of distribution power network with high penetration of plug-in hybrid electric vehicles," in *2010 Twenty-Fifth Annual IEEE Applied Power Electronics Conference and Exposition (APEC)*, pp. 1755–1762, Feb. 2010. ISSN: 1048-2334.

[66] C. Roncero-Clemente, O. Husev, E. Romero-Cadaval, J. Martins, D. Vinnikov, and M. Milanés-Montero, "Three-phase three-level neutral-point-clamped qZ source inverter with active filtering capabilities," in *2015 9th International Conference on Compatibility and Power Electronics (CPE)*, pp. 216–220, June 2015. ISSN: 2166-9546.

[67] V. Miñambres-Marcos, E. Romero-Cadaval, M. Á. Guerrero-Martínez, and M. I. Milanés-Montero, "Three-phase single stage photovoltaic inverter with active filtering capabilities," in *IECON 2012 - 38th Annual Conference on IEEE Industrial Electronics Society*, pp. 5253–5258, Oct. 2012. ISSN: 1553-572X.

[68] V. Monteiro, J. G. Pinto, and J. L. Afonso, "Operation Modes for the Electric Vehicle in Smart Grids and Smart Homes: Present and Proposed Modes," *IEEE Transactions on Vehicular Technology*, vol. 65, pp. 1007–1020, Mar. 2016. Conference Name: IEEE Transactions on Vehicular Technology.

[69] A. Khaligh and M. D'Antonio, "Global Trends in High-Power On-Board Chargers for Electric Vehicles," *IEEE Transactions on Vehicular Technology*, vol. 68, pp. 3306–3324, Apr. 2019. Conference Name: IEEE Transactions on Vehicular Technology.

[70] M. Yilmaz and P. T. Krein, "Review of Battery Charger Topologies, Charging Power Levels, and Infrastructure for Plug-In Electric and Hybrid Vehicles," *IEEE Transactions on Power Electronics*, vol. 28, pp. 2151–2169, May 2013. Conference Name: IEEE Transactions on Power Electronics.

[71] S. Rivera, S. Kouro, S. Vazquez, S. M. Goetz, R. Lizana, and E. Romero-Cadaval, "Electric Vehicle Charging Infrastructure – From Grid to Battery," *IEEE Industrial Electronics Magazine*, pp. 0–0, 2021. Conference Name: IEEE Industrial Electronics Magazine.

[72] I. Subotic and E. Levi, "A review of single-phase on-board integrated battery charging topologies for electric vehicles," in *2015 IEEE Workshop on Electrical Machines Design, Control and Diagnosis (WEMDCD)*, pp. 136–145, Mar. 2015.

[73] D. Kim, M. Kim, and B. Lee, "An Integrated Battery Charger With High Power Density and Efficiency for Electric Vehicles," *IEEE Transactions on Power Electronics*, vol. 32, pp. 4553–4565, June 2017. Conference Name: IEEE Transactions on Power Electronics.

[74] C. Shi and A. Khaligh, "A Two-Stage Three-Phase Integrated Charger for Electric Vehicles With Dual Cascaded Control Strategy," *IEEE Journal of Emerging and Selected Topics in Power Electronics*, vol. 6, pp. 898–909, June 2018. Conference Name: IEEE Journal of Emerging and Selected Topics in Power Electronics.

[75] J. Ye, C. Shi, and A. Khaligh, "Single-Phase Charging Operation of a Three-Phase Integrated Onboard Charger for Electric Vehicles," in *2018 IEEE Transportation Electrification Conference and Expo (ITEC)*, pp. 681–686, June 2018.

[76] V. F. Pires, A. Cordeiro, D. Foito, and J. F. Silva, "A Three-Phase On-Board Integrated Battery Charger for EVs with Six-Phase Machine and Nine Switch Converter," in *2019 IEEE 13th International Conference on Compatibility, Power Electronics and Power Engineering (CPE-POWERENG)*, pp. 1–6, Apr. 2019. ISSN: 2166-9546.

[77] Y. Xiao, C. Liu, and F. Yu, "An Effective Charging-Torque Elimination Method for Six-Phase Integrated On-Board EV Chargers," *IEEE Transactions on Power Electronics*, vol. 35, pp. 2776–2786, Mar. 2020. Conference Name: IEEE Transactions on Power Electronics.

[78] C. Shi, Y. Tang, and A. Khaligh, "A Single-Phase Integrated Onboard Battery Charger Using Propulsion System for Plug-in Electric Vehicles," *IEEE Transactions on Vehicular Technology*, vol. 66, pp. 10899–10910, Dec. 2017. Conference Name: IEEE Transactions on Vehicular Technology.

[79] J. Gao, D. Jiang, W. Sun, and Y. Zhang, "Zero Torque Three Phase Integrated On-board Charger by Multi-Elements Motor Torque Cancellation," in *2019 IEEE Energy Conversion Congress and Exposition (ECCE)*, pp. 563–568, Sept. 2019. ISSN: 2329-3748.

[80] S. Q. Ali, D. Mascarella, G. Joos, and L. Tan, "Torque Cancelation of Integrated Battery Charger Based on Six-Phase Permanent Magnet Synchronous Motor

Drives for Electric Vehicles," *IEEE Transactions on Transportation Electrification*, vol. 4, pp. 344–354, June 2018. Conference Name: IEEE Transactions on Transportation Electrification.

[81] S. Q. Ali, D. Mascarella, G. Joos, and L. Tan, "Torque elimination for integrated battery charger based on two permanent magnet synchronous motor drives for electric vehicles," *IET Electric Power Applications*, vol. 11, no. 9, pp. 1627–1635, 2017. _eprint: https://ietresearch.onlinelibrary.wiley.com/doi/pdf/10.1049/iet-epa.2017.0302.

[82] S. Sharma, M. V. Aware, and A. Bhowate, "Integrated Battery Charger for EV by Using Three-Phase Induction Motor Stator Windings as Filter," *IEEE Transactions on Transportation Electrification*, vol. 6, pp. 83–94, Mar. 2020. Conference Name: IEEE Transactions on Transportation Electrification.

[83] S. He, Z. Xu, M. Chen, H. Yang, and W. Li, "General Derivation Law With Torque-Free Achieving of Integral On-Board Charger on Compact Powertrains," *IEEE Transactions on Industrial Electronics*, vol. 68, pp. 1791–1802, Feb. 2021. Conference Name: IEEE Transactions on Industrial Electronics.

[84] H. Fakham, D. Lu, and B. Francois, "Power Control Design of a Battery Charger in a Hybrid Active PV Generator for Load-Following Applications," *IEEE Transactions on Industrial Electronics*, vol. 58, pp. 85–94, Jan. 2011. Conference Name: IEEE Transactions on Industrial Electronics.

[85] M. C. Kisacikoglu, B. Ozpineci, and L. M. Tolbert, "EV/PHEV Bidirectional Charger Assessment for V2G Reactive Power Operation," *IEEE Transactions on Power Electronics*, vol. 28, pp. 5717–5727, Dec. 2013. Conference Name: IEEE Transactions on Power Electronics.

[86] D. B. Wickramasinghe Abeywardana, B. Hredzak, and V. G. Agelidis, "A Fixed-Frequency Sliding Mode Controller for a Boost-Inverter-Based Battery-Supercapacitor Hybrid Energy Storage System," *IEEE Transactions on Power Electronics*, vol. 32, pp. 668–680, Jan. 2017. Conference Name: IEEE Transactions on Power Electronics.

[87] J. Gao, W. Sun, D. Jiang, Y. Zhang, and R. Qu, "Improved Operation and Control of Single-Phase Integrated On-Board Charger System," *IEEE Transactions on Power Electronics*, vol. 36, pp. 4752–4765, Apr. 2021. Conference Name: IEEE Transactions on Power Electronics.

[88] M. I. Milanes-Montero, E. Romero-Cadaval, A. R. de Marcos, V. M. Minambres-Marcos, and F. Barrero-Gonzalez, "Novel method for synchronization to disturbed three-phase and single-phase systems," in *2007 IEEE International Symposium on Industrial Electronics*, pp. 860–865, June 2007. ISSN: 2163-5145.

[89] R. Holehouse, A. Shahaj, M. Michon, and B. James, "Integrated approach to NVH analysis in electric vehicle drivetrains," *The Journal of Engineering*, vol. 2019, no. 17, pp. 3842–3847, 2019. _eprint: https://ietresearch.onlinelibrary.wiley.com/doi/pdf/10.1049/joe.2018.8247.

[90] Z. Yang, M. Krishnamurthy, and I. P. Brown, "Electromagnetic and vibrational characteristic of IPM over full torque-speed range," in *2013 International Electric Machines Drives Conference*, pp. 295–302, May 2013.

[91] J. Poxon, P. Jennings, and M. Allman-Ward, "Development of a Hybrid Electric Vehicle (HEV) Model for Interactive Customer Assessment of Sound Quality," in *IET HEVC 2008 - Hybrid and Eco-Friendly Vehicle Conference*, pp. 1–4, Dec. 2008. ISSN: 0537-9989.

[92] M. Sarrazin, S. Gillijns, J. Anthonis, K. Janssens, H. van der Auweraer, and K. Verhaeghe, "NVH analysis of a 3 phase 12/8 SR motor drive for HEV applications," in *2013 World Electric Vehicle Symposium and Exhibition (EVS27)*, pp. 1–10, Nov. 2013.

[93] T. Karikomi, K. Itou, T. Okubo, and S. Fujimoto, "Development of the Shaking Vibration Control for Electric Vehicles," in *2006 SICE-ICASE International Joint Conference*, pp. 2434–2439, Oct. 2006.

[94] Q. Wang, K. Rajashekara, Y. Jia, and J. Sun, "A Real-Time Vibration Suppression Strategy in Electric Vehicles," *IEEE Transactions on Vehicular Technology*, vol. 66, pp. 7722–7729, Sept. 2017. Conference Name: IEEE Transactions on Vehicular Technology.

[95] G. Götting and M. Kretschmer, "Development and series application of a vehicle drivetrain observer used in hybrid and electric vehicles," in *2013 World Electric Vehicle Symposium and Exhibition (EVS27)*, pp. 1–9, Nov. 2013.

[96] W. Sun, H. Gao, and B. Yao, "Adaptive Robust Vibration Control of Full-Car Active Suspensions With Electrohydraulic Actuators," *IEEE Transactions on Control Systems Technology*, vol. 21, pp. 2417–2422, Nov. 2013. Conference Name: IEEE Transactions on Control Systems Technology.

[97] C. Gohrle, A. Schindler, A. Wagner, and O. Sawodny, "Design and Vehicle Implementation of Preview Active Suspension Controllers," *IEEE Transactions on Control Systems Technology*, vol. 22, pp. 1135–1142, May 2014. Conference Name: IEEE Transactions on Control Systems Technology.

[98] E. Marioni, "Washer or Similar Domestic Appliance Activated by a Synchronous Electric Motor with a Detaching Device Detection Device," Mar. 2011.

[99] W. He, X. He, and C. Sun, "Vibration Control of an Industrial Moving Strip in the Presence of Input Deadzone," *IEEE Transactions on Industrial Electronics*, vol. 64, pp. 4680–4689, June 2017. Conference Name: IEEE Transactions on Industrial Electronics.

[100] K. Szabat and T. Orlowska-Kowalska, "Vibration Suppression in a Two-Mass Drive System Using PI Speed Controller and Additional Feedbacks—Comparative Study," *IEEE Transactions on Industrial Electronics*, vol. 54, pp. 1193–1206, Apr. 2007. Conference Name: IEEE Transactions on Industrial Electronics.

[101] T. Orlowska-Kowalska and K. Szabat, "Control of the Drive System With Stiff and Elastic Couplings Using Adaptive Neuro-Fuzzy Approach," *IEEE Transactions on Industrial Electronics*, vol. 54, pp. 228–240, Feb. 2007. Conference Name: IEEE Transactions on Industrial Electronics.

[102] H. Fu, C. Feng, and S. Xue, "Vibration suppression control of an integrated powertrain of electric and hybrid vehicles using LQR controller and reduced-order observer," in *2014 IEEE Conference and Expo Transportation Electrification Asia-Pacific (ITEC Asia-Pacific)*, pp. 1–6, Aug. 2014.

[103] K. Peter, I. Scholing, and B. Orlik, "Robust output-feedback H/sub /spl infin// control with a nonlinear observer for a two-mass system," *IEEE Transactions on Industry Applications*, vol. 39, pp. 637–644, May 2003. Conference Name: IEEE Transactions on Industry Applications.

[104] H. M. Isa, W. N. L. Mahadi, R. Ramli, and M. Abidin, "A review on electromagnetic suspension systems for passenger vehicle," in *International Conference on Electrical, Control and Computer Engineering 2011 (InECCE)*, pp. 399–403, June 2011.